

AD-A241 684



2

GL-TR-90-0285
ENVIRONMENTAL RESEARCH PAPERS, NO. 1067

Refinement and Testing of the Moist Convection
Parameterization in the GL Global Spectral Model

DONALD C. NORQUIST
CHIEN-HSIUNG YANG

DTIC
ELECTE
OCT 16 1991
S D D



22 October 1990



Approved for public release; distribution unlimited.



91-13240



ATMOSPHERIC SCIENCES DIVISION PROJECT 2310
GEOPHYSICS LABORATORY
HANSCOM AFB, MA 01731-5000

"This technical report has been reviewed and is approved for publication"

FOR THE COMMANDER



DONALD A. CHISHOLM, Chief
Atmospheric Prediction Branch



ROBERT A. McCLATCHEY, Director
Atmospheric Sciences Division

This document has been reviewed by the ESD Public Affairs Office (PA) and is releasable to the National Technical Information Service (NTIS).

Qualified requestors may obtain additional copies from the Defense Technical Information Center. All others should apply to the National Technical Information Service.

If your address has changed, or if you wish to be removed from the mailing list, or if the addressee is no longer employed by your organization, please notify GL/DAA, Hanscom AFB, MA 01731. This will assist us in maintaining a current mailing list.

REPORT DOCUMENTATION PAGE

Form Approved
OMB No. 0704-0188

Public reporting burden for this collection of information is estimated to average 7 hours per response, including the time for reviewing instructions, searching existing data sources, gathering and maintaining the data needed, and completing and reviewing the collection of information. Send comments regarding this burden estimate or any other aspect of this collection of information, including suggestions for reducing the burden, to Washington Headquarters Office, Directorate for Information Operations and Reports, U.S. Office of Management and Budget, Paperwork Reduction Project (0704-0188), Washington, DC 20503.

1. AGENCY USE ONLY (Leave blank)		2. REPORT DATE 22 October 1990	3. REPORT TYPE AND DATES COVERED Interim Report 6 Jun 86 - 31 Mar 90	
4. TITLE AND SUBTITLE Refinement and Testing of the Moist Convection Parameterization in the GL Global Spectral Model			5. FUNDING NUMBERS PE: 61102F PR: 2310 TA: G7 WU: 09	
6. AUTHOR(S) Norquist, Donald C. Yang, Chien-hsiung				
7. PERFORMING ORGANIZATION NAME(S) AND ADDRESS(ES) Geophysics Laboratory (AFSC/LYP) Hanscom Air Force Base Massachusetts 01731			9. PERFORMING ORGANIZATION REPORT NUMBER ERP, No. 1067 GL-TR-90-0285	
9. SPONSORING / MONITORING AGENCY NAME(S) AND ADDRESS(ES)			10. SPONSORING / MONITORING AGENCY REPORT NUMBER	
11. SUPPLEMENTARY NOTES				
12a. DISTRIBUTION AVAILABILITY STATEMENT Approved for public release; distribution unlimited			12b. DISTRIBUTION CODE	
13. ABSTRACT (Maximum 200 words) An evaluation of the original version of the advanced physics moist convection parameterization revealed excessive heating and precipitation being produced by the scheme within the global spectral model. This report describes a series of corrections and modifications made to the parameterization software to improve its performance. Forecast experiments were conducted to determine the effectiveness of each modification. We found that turning off the entrainment formulation, using a newly developed scheme for computing the lifting condensation level and moist adiabat, employing a center-difference scheme for computing moisture convergence, and allowing evaporation of falling precipitation in the cloudy portion of the grid box yielded the most realistic convective heating and precipitation. This version of the convective scheme was used in a series of 10-day global spectral model forecasts over January and June 1979 to further scrutinize its performance. Global and zonal average distributions of precipitation agreed well with climatological estimates for the same months. We found that although the modified version of the scheme resulted in substantially reduced convective precipitation, it still produced more than was observed in areas of high climatological rainfall. We				
14. SUBJECT TERMS Moist convection Atmospheric models Cumulus parameterization Numerical weather prediction			15. NUMBER OF PAGES 134	
			16. PRICE CODE	
17. SECURITY CLASSIFICATION OF REPORT Unclassified	18. SECURITY CLASSIFICATION OF THIS PAGE Unclassified	19. SECURITY CLASSIFICATION OF ABSTRACT Unclassified	20. LIMITATION OF ABSTRACT SAR	

Continued from #13

conclude that in the tropics, the modified convective scheme produces too much precipitation in areas characterized by heavy precipitation, and not enough precipitation in the more arid regions. In the extratropics, wintertime convection downstream from continents (typically involved in cyclogenesis) was simulated by the model. Summertime convection over the United States was characterized by too little precipitation in the typically convectively active areas, and too much in the more convectively stable regions of the country.

Illustrations

1. Globally-Averaged Total and Convective Precipitation Rates (10^{-5} kg m⁻² s⁻¹) and Percent Convective Points for Three Versions of the GSM (GWC84, GWC84IL, GLALL) Initialized 1200 UTC 17 June 1979. 6
2. Geopotential Height Bias (m) of Four Versions of the GSM (GWC84, GWC84IL, GLNOC, GLALL) Initialized 1200 UTC 17 June 1979 When Evaluated Against the Global Radiosonde Network. 9
3. Relative Humidity Bias (percent) of Four Versions of the GSM (GWC84, GWC84IL, GLNOC, GLALL) Initialized 1200 UTC 17 June 1979 When Evaluated Against the Global Radiosonde Network. 10
4. Forecast Day 5 Zonally-Averaged Temperature Bias (K) of GSM Experiment 0 (Original MODKUU) Initialized 1200 UTC 11 June 1979 When Evaluated Against FGGE III-B Analysis. 11
5. Forecast Day 5 Zonally-Averaged Relative Humidity Bias (percent) of GSM Experiment 0 (Original MODKUU) Initialized 1200 UTC 11 June 1979 When Evaluated Against FGGE III-B Analysis. 12
6. Globally-Averaged Total Precipitation Rates (mm day⁻¹) for Four Versions of the GSM (Exp. 0,G,1,3) Initialized 1200 UTC 11 June 1979. 17
7. Forecast Day 5 Zonally-Averaged Temperature Bias (K) of GSM Experiment G (Corrected MODKUU) Initialized 1200 UTC 11 June 1979 When Evaluated Against FGGE III-B Analysis. 18
8. Forecast Day 5 Zonally Averaged Relative Humidity Bias (Percent) of GSM Experiment G (Corrected MODKUU) Initialized 1200 UTC 11 June 1979 When Evaluated Against FGGE III-B Analysis. 19

9. Convective Precipitation Rates (mm day ⁻¹) Over Four Grid Points in Western Africa from GSM Experiment 0 (Original MODKUO) Initialized 1200 UTC 17 June 1979.	21
10. Convective Heating Fraction (percent) Over Four Grid Points in Western Africa from GSM Experiment 0 (Original MODKUO) Initialized 1200 UTC 17 June 1979.	22
11. Forecast Day 5 Zonally-Averaged Temperature Bias (K) of GSM Experiment 1 (Corrected MODKUO Without Entrainment) Initialized 1200 UTC 11 June 1979 When Evaluated Against FGGE III-B Analysis.	23
12. Forecast Day 5 Zonally-Averaged Relative Humidity Bias (percent) of GSM Experiment 1 (Corrected MODKUO Without Entrainment) Initialized 1200 UTC 11 June 1979 When Evaluated Against FGGE III-B Analysis.	24
13. Forecast Day 5 Zonally-Averaged Temperature Bias (K) of GSM Experiment 3 (GL Baseline) Initialized 1200 UTC 11 June 1979 When Evaluated Against FGGE III-B Analysis.	26
14. Forecast Day 5 Zonally-Averaged Relative Humidity Bias (percent) of GSM Experiment 3 (GL Baseline) Initialized 1200 UTC 11 June 1979 When Evaluated Against FGGE III-B Analysis.	27
15. Globally-Averaged Total Precipitation Rates (mm day ⁻¹) for Five Versions of the GSM (Exp. 3,4,5,8,9) Initialized 1200 UTC 11 June 1979.	32
16. Forecast Day 5 Zonally-Averaged Temperature Bias (K) of GSM Experiment 4 (GL Evap) Initialized 1200 UTC 11 June 1979 When Evaluated Against FGGE III-B Analysis.	33
17. Forecast Day 5 Zonally-Averaged Relative Humidity Bias (percent) of GSM Experiment 4 (GL Evap) Initialized 1200 UTC 11 June 1979 When Evaluated Against FGGE III-B Analysis.	34
18. Forecast Day 5 Zonally-Averaged Temperature Bias (K) of GSM Experiment 5 (NMC Evap) Initialized 1200 UTC 11 June 1979 When Evaluated Against FGGE III-B Analysis.	35
19. Forecast Day 5 Zonally-Averaged Relative Humidity Bias (percent) of GSM Experiment 5 (NMC Evap) Initialized 1200 UTC 11 June 1979 When Evaluated Against FGGE-III-B Analysis.	36
20. Forecast Day 5 Zonally-Averaged Temperature Bias (K) of GSM Experiment 8 (NMC Evap & Lpfrg) Initialized 1200 UTC 11 June 1979 When Evaluated Against FGGE III-B Analysis.	39
21. Forecast Day 5 Zonally-Averaged Relative Humidity Bias (percent) of GSM Experiment 8 (NMC Evap & Lpfrg) Initialized 1200 UTC 11 June 1979 When Evaluated Against FGGE III-B Analysis.	40

22. Forecast Day 5 Zonally-Averaged Temperature Bias (K) of GSM Experiment 9 (GL Evap & Lpfrg) Initialized 1200 UTC 11 June 1979 When Evaluated Against FGGE III-B Analysis.	41
23. Forecast Day 5 Zonally-Averaged Relative Humidity Bias (percent) of GSM Experiment 9 (GL Evap & Lpfrg) Initialized 1200 UTC 11 June 1979 When Evaluated Against FGGE III-B Analysis.	42
24. Zonally-Averaged Total Precipitation (mm) Accumulated Over Days 2-4 (X 10) for Five Versions of the GSM Initialized 1200 UTC 11 June 1979 as Compared with Jaeger ¹⁹ June Climatology Precipitation.	46
25. Map of 3-Day Total Precipitation Accumulation (mm) for 1200 UTC 12-15 June 1979 of GSM Experiment 3 (GL Baseline) Initialized 1200 UTC 11 June 1979.	47
26. Map of 3-Day Total Precipitation Accumulation (mm) for 1200 UTC 12-15 June 1979 of GSM Experiment 9 (GL Evap & Lpfrg) Initialized 1200 UTC 11 June 1979.	48
27. GSM Grid Box 3-Day Precipitation (mm) for 1200 UTC 12-15 June 1979 Over the Tropical Ocean Area: (a) Observed, (b) GSM Exp. 3	50
27. GSM Grid Box 3-Day Precipitation (mm) for 1200 UTC 12-15 June 1979 Over the Tropical Ocean Area: (c) GSM Exp. 9, (d) Number of Observations in Grid Box Average.	51
28. GSM Grid Box 3-Day Precipitation (mm) for 1200 UTC 12-15 June 1979 Over the Tropical Land Area: (a) Observed, (b) GSM Exp. 3	52
28. GSM Grid Box 3-Day Precipitation (mm) for 1200 UTC 12-15 June 1979 Over the Tropical Land Area: (c) GSM Exp. 9, (d) Number of Observations in Grid Box Average.	53
29. GSM Grid Box 3-Day Precipitation (mm) for 1200 UTC 12-15 June 1979 Over the Extratropical Land Area: (a) Observed, (b) GSM Exp. 3	54
29. GSM Grid Box 3-Day Precipitation (mm) for 1200 UTC 12-15 June 1979 Over the Extratropical Land Area: (c) GSM Exp. 9, (d) Number of Observations in Grid Box Average.	55
30. Vertical Profile of Convective Heating Rates (K day ⁻¹) for 11-14 June 1979 Averaged Over All Convectively Active Points in +15° Latitude Band for GSM Experiment 9 as Compared with Southwestern Pacific Observed Profile from Reed and Recker ²¹ .	57
31. CAPE (10 ⁻⁵ m ² s ⁻²) Over the Tropical Ocean Area for (a) 24h and (b) 48h Forecast Times From the 1200 UTC 11 June 1979 Experiment 9 Forecast.	60
32. Moisture Convergence (g kg ⁻¹ day ⁻¹) Over the Tropical Ocean Area for (a) 30h and (b) 42h Forecast Times From the 1200 UTC 11 June 1979 Experiment 9 Forecast.	61

33. Precipitation Rate (mm day^{-1}) Over the Tropical Ocean Area for (a) 30h and (b) 42h Forecast Times From the 1200 UTC 11 June 1979 Experiment 9 Forecast.	62
34. Convective Cloud Cover (percent) Over the Tropical Area for (a) 30h and (b) 42h Forecast Times From the 1200 UTC 11 June 1979 Experiment Forecast.	63
35. Cloud Top Temperature (C) Over the Tropical Ocean Area for the 42h Forecast Time From the 1200 UTC 11 June 1979 Experiment 9 Forecast.	65
36. Cloud Top Pressure (kPa) Over the Tropical Ocean Area for the 42h Forecast Time From the 1200 UTC 11 June 1979 Experiment 9 Forecast.	65
37. Areal-Averaged Convective Quantities Over the Tropical Ocean Area in Their Departure From the Time Mean Computed Over the First Four Days of the 1200 UTC 11 June 1979 Experiment 9 Forecast.	66
38. Areal-Averaged Isobaric Temperature (K) Over the Tropical Ocean Area in its Departure From the Time Mean Computed Over the First Four Days of the 1200 UTC 11 June 1979 Experiment 9 Forecast.	67
39. Forecast Days 1-10 Northern Hemisphere-Averaged Temperature Bias (K) of (a) GWC84, Initialized 1200 UTC on Each of the Indicated January 1979 Dates (Width of Each Individual Graph Box is 5 K, Marks on Curves Indicate Position of Mandatory Pressure Levels to 50 kPa).	71
39. Forecast Days 1-10 Northern Hemisphere-Averaged Temperature Bias (K) of (b) GL-87, Initialized 1200 UTC on Each of the Indicated January 1979 Dates (Width of Each Individual Graph Box is 5 K, Marks on Curves Indicate Position of Mandatory Pressure Levels to 50 kPa).	72
39. Forecast Days 1-10 Northern Hemisphere-Averaged Temperature Bias (K) of (c) GL89 Initialized 1200 UTC on Each of the Indicated January 1979 Dates (Width of Each Individual Graph Box is 5 K, Marks on Curves Indicate Position of Mandatory Pressure Levels to 50 kPa).	73
40a. Globally-Averaged Total Precipitation Rates (mm day^{-1}) Averaged Over January Forecasts of GWC84, GL-87, and GL-89.	76
40b. Globally-Averaged Total Precipitation Rates (mm day^{-1}) Averaged Over June Forecasts of GWC84, GL-87, and GL-89.	77
41a. Total Precipitation Rates (mm day^{-1}), Globally-Averaged Total Convective for GL-89 Initialized 1200 UTC 05 January 1979.	78
41b. Total Precipitation Rates (mm day^{-1}), Latitude-Band ($+15^\circ$) Averaged Convective for GL-89 Initialized 1200 UTC 05 January 1979.	79
42a. Globally-Averaged Convective Precipitation Rates (mm day^{-1}) Averaged Over January Forecasts of GWC84, GL-87, and GL-89.	80

42b. Globally-Averaged Convective Precipitation Rates (mm day^{-1}) Averaged Over June Forecasts of GWC84, GL-87, and GL-89.	81
43a. Globally-Averaged Surface Evaporation Rates (mm day^{-1}) Averaged Over January Forecasts of GWC84, GL-87, and GL-89.	82
43b. Globally-Averaged Surface Evaporation Rates (mm day^{-1}) Averaged Over June Forecasts of GWC84, GL-87, and GL-89.	83
44. Vertically-Integrated Global Root-Mean-Square Specific Humidity (g kg^{-1}) for the 17 January 1979 and 15 June 1979 GL-87 and GL-89 Forecasts.	85
45a. Zonally-Averaged Accumulated Convective and Large-Scale Precipitation (mm) Summed Over Days 2-6 of All January Forecasts of GL-89.	86
45b. Zonally-Averaged Accumulated Convective and Large-Scale Precipitation (mm) Summed Over Days 2-6 of All June Forecasts of GL-89.	87
46a. Zonally-Averaged Accumulated Convective and Large-Scale Precipitation (mm) Summed Over Days 2-6 of All January Forecasts of GL-89.	89
46b. Zonally-Averaged Accumulated Convective and Large-Scale Precipitation (mm) Summed Over Days 2-6 of All June Forecasts of GL-89.	90
47. Maps of Accumulated Convective Precipitation (mm) Summed Over Days 2-6 of All (a) January and (b) June Forecasts of GL-89 (Contour Interval is 150 mm).	91
48a. Maps of Outgoing Longwave Radiation (W m^{-2}) At the Top of the Atmosphere for January of 1979 Taken from Bess and Smith ²⁶ .	93
48b. Maps of Outgoing Longwave Radiation (W m^{-2}) At the Top of the Atmosphere for June of 1979 Taken from Bess and Smith ²⁶ .	94
49. Maps of Accumulated Total Precipitation (mm) Summed Over Days 2-6 of All (a) January and (b) June Forecasts of GL-89 (Contour Interval is 150 mm).	95
50. Map of Climatological Precipitation (mm) for January Taken from Jaeger ¹⁹ .	96
51a. Latitude-Band Average Accumulated Convective and Large-Scale Precipitation (mm) Summed Over Days 2-6 of All January (0° - 15° S) Forecasts of GL-89 in Their Departure from the Zonal Mean.	97
51b. Latitude-Band Average Accumulated Convective and Large-Scale Precipitation (mm) Summed Over Days 2-6 of All June (0° - 15° N) Forecasts of GL-89 in Their Departure from the Zonal Mean.	98
52. GSM Grid Box Accumulated Precipitation (mm) for June 1979 over the Tropical Ocean Area: (a) Observed, (b) GL-89.	100
53. GSM Grid Box Accumulated Precipitation (mm) for June 1979 over the Tropical Land Area: (a) Observed, (b) GL-89 total	101

53. GSM Grid Box Accumulated Precipitation (mm) for June 1979 over the Tropical Land Area: (c) GL-89 Convective.	102
54. Latitude-Band (25° - 40°N) Average Accumulated Convective and Large-Scale Precipitation (mm) for January Forecasts of GL-89 in Their Departure from the Zonal Mean.	105
55. Latitude-Band (35° - 50°N) Average Accumulated Convective and Large-Scale Precipitation (mm) for June Forecasts of GL-89 in their Departure from the Zonal Mean.	106
56a. GSM Grid Box Accumulated Precipitation (mm) for June 1979 over the U.S.: Observed.	107
56b. GSM Grid Box Accumulated Precipitation (mm) for June 1979 over the U.S.: GL-89.	108
57. Map of Average Number of Thunderstorm Days for June Taken from Guttman ²⁹ .	110
58. GSM Grid Box Differences in Accumulated Precipitation (mm) for June 1979 Between GL-89 and Observations (Areas Outlined are Regions Referred to in Text).	111

Table

- | | |
|---|-----|
| 1. Statistics for Comparison of GL-89 and Observed Accumulated June 1979
Precipitation in GSM Grid Boxes Over the U.S. | 112 |
|---|-----|

Refinement and Testing of the Moist Convection Parameterization in the GL Global Spectral Model

1. INTRODUCTION

In an attempt to address the requirements of improved Air Force capability in global cloud and precipitation forecasting, the Atmospheric Prediction Branch at the Geophysics Laboratory (GL) has undertaken the implementation, refinement, and experimental testing of advanced physical parameterization schemes for its Global Spectral Model (GSM). The adiabatic portion of the model was originally acquired from the National Meteorological Center (NMC) in 1981 through Sela.¹ This portion of the model was completely rewritten and the hydrodynamics reformulated as

(Received for Publication 18 October 1990)

¹Sela, J. (1980) Spectral modeling at the National Meteorological Center, *Mon. Wea. Rev.*, **108**: 1279-1292.

reported by Brenner et al.^{2,3} A normal mode initialization scheme developed by Ballish⁴ was also acquired from NMC at that time and installed for use at GL.

The physical parameterizations of the NMC GSM (especially those dealing with atmospheric moisture) were rather limited and rudimentary. We undertook, therefore, the pursuit of more physically realistic schemes to achieve stated model performance goals. Three university groups under GL sponsorship undertook the development of new schemes of incorporating diabatic physical processes into the model. Mahrt et al,^{5,6} at Oregon State University developed a planetary boundary layer (PBL) parameterization that applied over both land and ocean surfaces. Liou and his associates^{7,8} at the University of Utah designed a scheme that calculated both infrared and solar radiation transfers in both clear and cloudy atmospheres.

²Brenner, S., Yang, C.-H., and Yee, S.Y.K. (1982) *The AFGL Spectral Model of the Moist Global Atmosphere: Documentation of the Baseline Version*, AFGL-TR-82-0393, Air Force Geophysics Laboratory, Hanscom AFB, MA. [NTIS ADA 129283]

³Brenner, S., Yang, C.-H., and Mitchell, K. (1984) *The AFGL Global Spectral Model: Expanded Resolution Baseline Version*, AFGL-TR-84-0308, Air Force Geophysics Laboratory, Hanscom AFB, MA. [NTIS ADA 160370]

⁴Ballish, B.A. (1980) *Initialization Theory and Application to the NMC Spectral Model*, Ph.D. Thesis. Dept. of Meteorology, Univ. of Maryland.

⁵Mahrt, L., Pan, H.-L., Paumier, J., and Troen, I. (1984) *A Boundary Layer Parameterization for a General Circulation Model*, AFGL-TR-84-0063, Air Force Geophysics Laboratory, Hanscom AFB, MA. [NTIS ADA 144224]

⁶Mahrt, L., Pan, H.-L., Ruscher, P., and Chu, C.-T. (1987) *Boundary Layer Parameterization for a Global Spectral Model*, AFGL-TR-87-0246, Air Force Geophysics Laboratory, Hanscom AFB, MA [NTIS ADA 199440]

⁷Liou, K.-N., Ou, S.-C., Kinne, S., and Koenig, G. (1984) *Radiation Parameterization Programs for Use in General Circulation Models*, AFGL-TR-84-0217, Air Force Geophysics Laboratory, Hanscom AFB, MA. [NTIS ADA 148015]

⁸Ou, S.-C., and Liou, K.-N. (1988) *Development of Radiation and Cloud Parameterization Programs for AFGL Global Models*, AFGL-TR-88-0018, Air Force Geophysics Laboratory, Hanscom AFB, MA. [NTIS ADA 202020]

Soong⁹ and Kao¹⁰ undertook an effort at the University of Illinois to investigate methods of cumulus parameterization. It is the continuing development and evaluation of parameterization schemes dealing with convection in the atmosphere that constitutes the focus of this report.

The University of Illinois investigation focused on two well-known convective parameterization schemes: the Arakawa-Schubert¹¹ procedure as discussed by Kao and Ogura¹⁰ and the Kuo^{12,13} procedure as detailed by Soong et al.⁹ The objectives of their research were: (1) to critically evaluate the Kuo and Arakawa-Schubert schemes for numerical weather prediction, and (2) to improve these cumulus parameterization schemes for the purpose of improving precipitation forecasts on the global scale. In their work on the Arakawa-Schubert scheme, they developed and tested a modified computational algorithm for computing the cloud spectrum using the quasi-equilibrium approximation. The major modifications developed and tested in the Kuo scheme were the prediction of cloud-top height and the incorporation of the effect of entrainment on cloud temperature and mixing ratio profiles. Two sets of comparative evaluations were conducted with the modified schemes: 1) semi-prognostic experiments within one-dimensional models in which forecasted heating and moistening profiles were compared with those computed from budget studies using GATE data, and 2) in the GL GSM of that time,² in which forecasted

⁹Soong, S.-T., Ogura, Y., and Kau, W.-S. (1985) *A Study of Cumulus Parameterization in a Global Circulation Model*, AFGL-TR-85-0160, Air Force Geophysics Laboratory, Hanscom AFB, MA. [NTIS ADA 170137]

¹⁰Kao, C.-Y. J., and Ogura, Y. (1985) *A Cumulus Parameterization Study with Special Attention to the Arakawa-Schubert Scheme*, AFGL-TR-85-0159, Air Force Geophysics Laboratory, Hanscom AFB, MA. [NTIS ADA 166801]

¹¹Arakawa, A. and Schubert, W.H. (1974) *Interaction of a cumulus cloud ensemble with the large-scale environment, Part 1*, *J. Atmos. Sci.*, **31**:674-701.

¹²Kuo, H.-L. (1965) *On formation and intensification of tropical cyclones through latent heat release by cumulus convection*, *J. Atmos. Sci.*, **22**:40-63.

¹³Kuo, H.-L. (1974) *Further studies of parameterization of the influence of cumulus convection on large-scale flow*, *J. Atmos. Sci.*, **31**:1232-1240.

precipitation amounts were compared with observations over the United States in April 1979 and with amounts produced by the model version received from NMC.¹ Both modified schemes produced what the investigators felt were reasonable distributions of convective precipitation in these evaluations.

While the two schemes produced comparable precipitation results, the Kuo scheme is more computationally efficient to run in an NWP model. Thus, we implemented the modified Kuo scheme (designated MODKUU) in the first version of the GL advanced physics GSM, which we refer to as GL-87 or GLALL. It also consisted of a PBL formulation⁵ and radiation scheme⁷ that constituted the initial model upgrade with new physical parameterization components. The performance of this model in two four-day model integrations has been fully documented by Yang et al.¹⁴ In addition to testing the advanced physics model, various combinations of the new physics packages were tested in an attempt to isolate the effect of each package on the model behavior. The most obvious consequences of MODKUU found in these experiments were: (1) a significant increase in convective activity globally over the basic NMC scheme, and in conjunction with the new PBL scheme, a maintenance of the increased amount at a relatively steady level through the four-day period, (2) a warming and drying of the middle troposphere, particularly in the tropics where convective activity is greatest, and (3) total rainfall far in excess of global climatology. The apparent overactivity of the MODKUU scheme became the focus of an intensive study. This report documents that study.

Clearly the behavior of the parameterization package was not physically realistic in a global context. The new convective scheme could not perform in physical balance with the other two newly-delivered physical parameterization schemes in its present state. At this stage, it was unclear how much of the overactivity of the scheme was due to feedbacks from the other two new physics packages and how much was due to MODKUU itself. For example, it was known that the enhanced vertical

¹⁴Yang, C.-H., Mitchell, K., Norquist, D., and Yee, S.Y.K. (1989) *Diagnostics for and Evaluation of New Physical Parameterization Schemes for Global NWP Models*, GL-TR-89-0158, Geophysics Laboratory (AFSC), Hanscom AFB, MA. [NTIS ADA 228033]

moisture fluxes in the new PBL scheme were capable of maintaining a source of moisture and precipitation rates in excess of those supported by the original PBL package. While global rainfall rates produced by a model with MODKURO and the old PBL scheme produced excessive precipitation in the first 24 hours of the forecast, insufficient moisture fluxes resulted in a rapid decay in the global precipitation rate as the forecast continued. In any case, it was clear that an adjustment of the scheme was necessary for it to play a dependable and reputable role in the total GL advanced physics package in the GSM.

Section 2 summarizes the diagnosis by Yang and others¹⁴ of the original MODKURO behavior. Sections 3 and 4 describe a series of experiments designed to test potential improvements to the scheme. Section 5 reports on the extensive testing of the resultant GL-modified MODKURO in a series of medium range forecast experiments. Section 6 includes a summary of progress of the cumulus parameterization scheme in the GL GSM and suggestions for future work.

2. REVIEW OF INITIAL MODKURO PERFORMANCE

Soong et al⁹ made several modifications to the Kuo 1974¹³ formulation that were incorporated into the testing by Yang et al¹⁴ in the GL GSM. These include the Krishnamurti et al¹⁵ computation of the so-called partitioning parameter b , a cloud-top estimation procedure, and the inclusion of entrainment in the cloud heating profile. Three versions of the GSM were evaluated using a 30 wave (rhomboidal) spectral truncation and a 12 vertical layer framework: the GSM received from NMC (called GWC84), replacing its convection scheme with MODKURO (called GWC84IL) and adding a new PBL formulation and radiation scheme to MODKURO (called GLALL). Two four-day global model runs were evaluated using FGGE III-A analyses

¹⁵Krishnamurti, T.N., Kanamitsu, M., Godbole, R., Chang C.-B., Carr F., and Chow, J.H. (1976) Study of a monsoon depression (II), dynamical structure, *J. Meteor. Soc. Japan*, **54**:208-225.

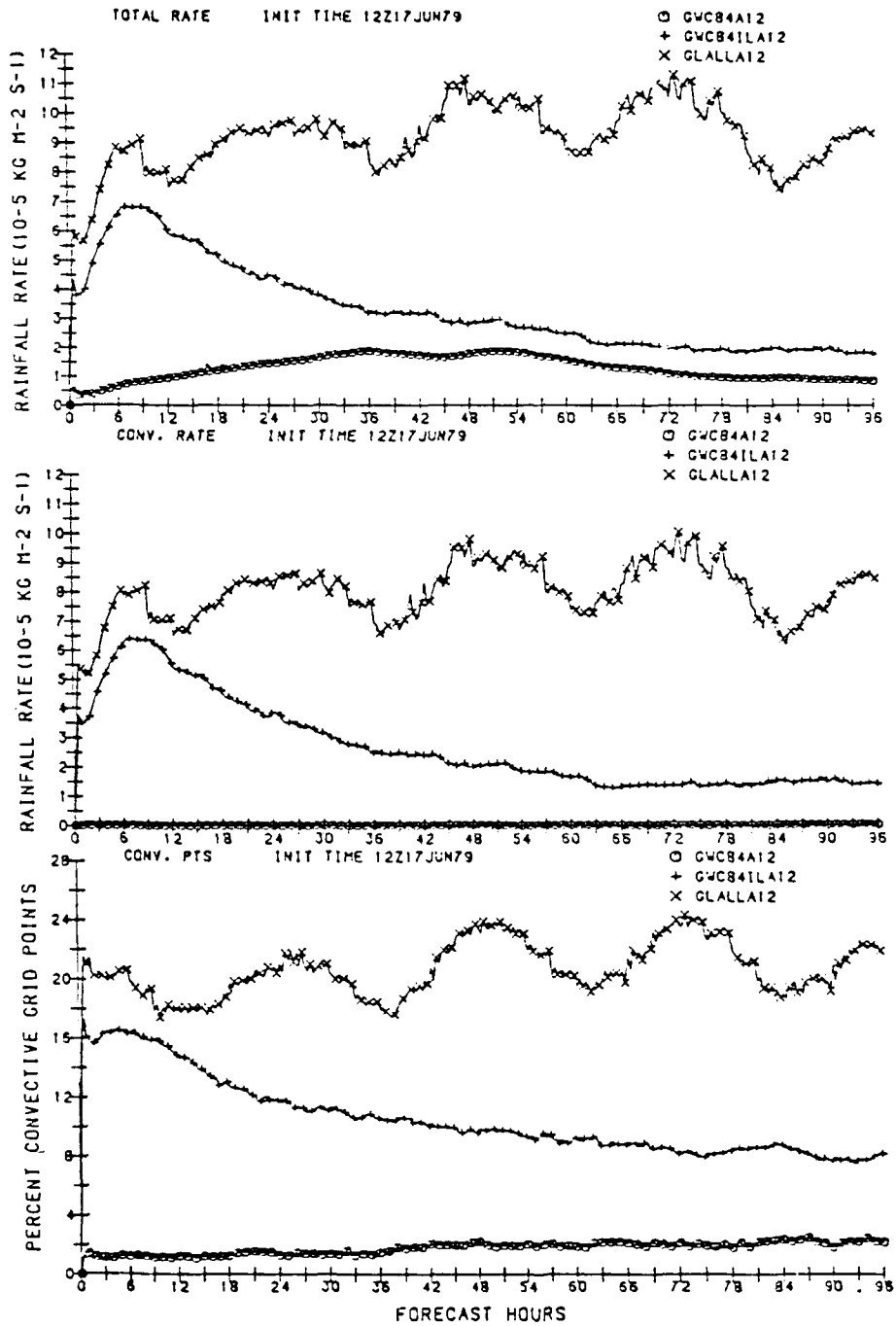


Figure 1. Globally-Averaged Total and Convective Precipitation Rates ($10^{-5} \text{ kg m}^{-2} \text{ s}^{-1}$) and Percent Convective Points for Three Versions of the GSM (GWC84, GWC84IL, GLALL) Initialized 1200 UTC 17 June 1979.

from 17 February and 17 June 1979 as initial conditions. A summary of the key points revealed in these experiments is presented below.

As can be seen in Figure 1, MODKUU produced enhanced precipitation rates in both the GWC84IL and GLALL versions of the GSM. The inclusion of MODKUU in GWC84IL increases convective precipitation to a rate greater than the stratiform precipitation rate (compare top panel to middle panel). As a point of reference, the global climatological average rainfall rate for June is $3.45 \times 10^{-5} \text{ kg m}^{-2} \text{ s}^{-1}$ (3 mm/day). In GLALL, MODKUU maintains precipitation rates that are 2.5 times the climatological value. As in GWC84IL, the convective component dominates the stratiform component of globally-averaged precipitation. The overactive MODKUU precipitation production is in sharp contrast to the GWC84 convective parameterization, which yields hardly any convective precipitation.

A comparison of the temporal variation of precipitation rate between GWCIL84 and GLALL in Figure 1 reveals the effect of the new PBL formulation. Both curves show an initial growth of precipitation rate for about 9 hours. Beyond that point, however, the rate in GWC84IL declines gradually while the rate in GLALL is maintained. The initial rapid increase results from the model's "spin-up" to a realistic level of divergence, overcoming the insufficient divergence in the initial flow field caused by the nonlinear normal mode initialization. Excessive precipitation rates deplete the atmospheric water vapor of the models, as evidenced in Figure 3 by a steady reduction in globally-averaged specific humidity. In GWC84IL, the precipitation rate decreases steadily to about 60 hours. At that point, an approximate hydrological balance is achieved between the precipitation and the atmospheric moisture supply (primarily, moisture transports from the ocean surface) and the rainfall rate is stabilized at approximately $2 \times 10^{-5} \text{ kg m}^{-2} \text{ s}^{-1}$. Since this is less than the climatological rate, it suggests that supply processes in the original PBL parameterization are unable to support realistic precipitation rates. In contrast, the GLALL precipitation rate curve demonstrates the effectiveness of the advanced PBL scheme in maintaining the process through the forecast period. In fact, the excessive precipitation rate is sustained in spite of the steady decline of globally-averaged specific humidity. The

depletion of atmospheric water vapor, even though vertical moisture transports are adequate, suggests that it is MODKUUO rather than the advanced PBL that is overactive. MODKUUO, acting as a sink of water vapor, exceeds the supply process of the advanced PBL and is depleting the atmospheric reservoir of water vapor.

Verification of the model forecasts from model runs with and without MODKUUO reinforces this conclusion. A comparison of model generated geopotential heights to radiosonde values (Figure 2) shows an increase in model layer thicknesses (and thus, temperatures) when MODKUUO is included (compare GWC84IL to GWC84 and GLALL to GLNOC). In both comparisons, including MODKUUO contributes to a warm bias by 24 hr, a bias that grows steadily during the four days. MODKUUO acts to increase temperature through latent heat release in proportion to precipitation rate. Yang et al¹⁴ concluded that excessive MODKUUO large-scale warming causes the warm bias. Figure 3 indicates that a significant drying of the model atmosphere is due to inclusion of MODKUUO. The RH decrease is due in part to a temperature increase with MODKUUO, but also to a decrease in the model atmospheric specific humidity. This is also consistent with the fact that MODKUUO produces excessive convective precipitation. As can be seen in Figure 4, the warm bias is most evident in low latitudes where convective processes play a major role in the heat budget of the atmosphere. Figure 5 reinforces the point that atmospheric water vapor depletion is greatest in low latitudes where MODKUUO activity is greatest. Thus, Yang et al¹⁴ have established the direct link between overactive precipitation and excessive warming and drying of the model atmosphere by MODKUUO.

3. CORRECTIONS AND IMPROVEMENTS TO THE CONVECTIVE PARAMETERIZATION SCHEME

The conclusions of the previous section led us to begin an exhaustive investigation of the MODKUUO parameterization to ensure that there were no obvious flaws or omissions that could account for its overactivity and to undertake a series of modifications aimed at achieving more realistic global, regional, and point

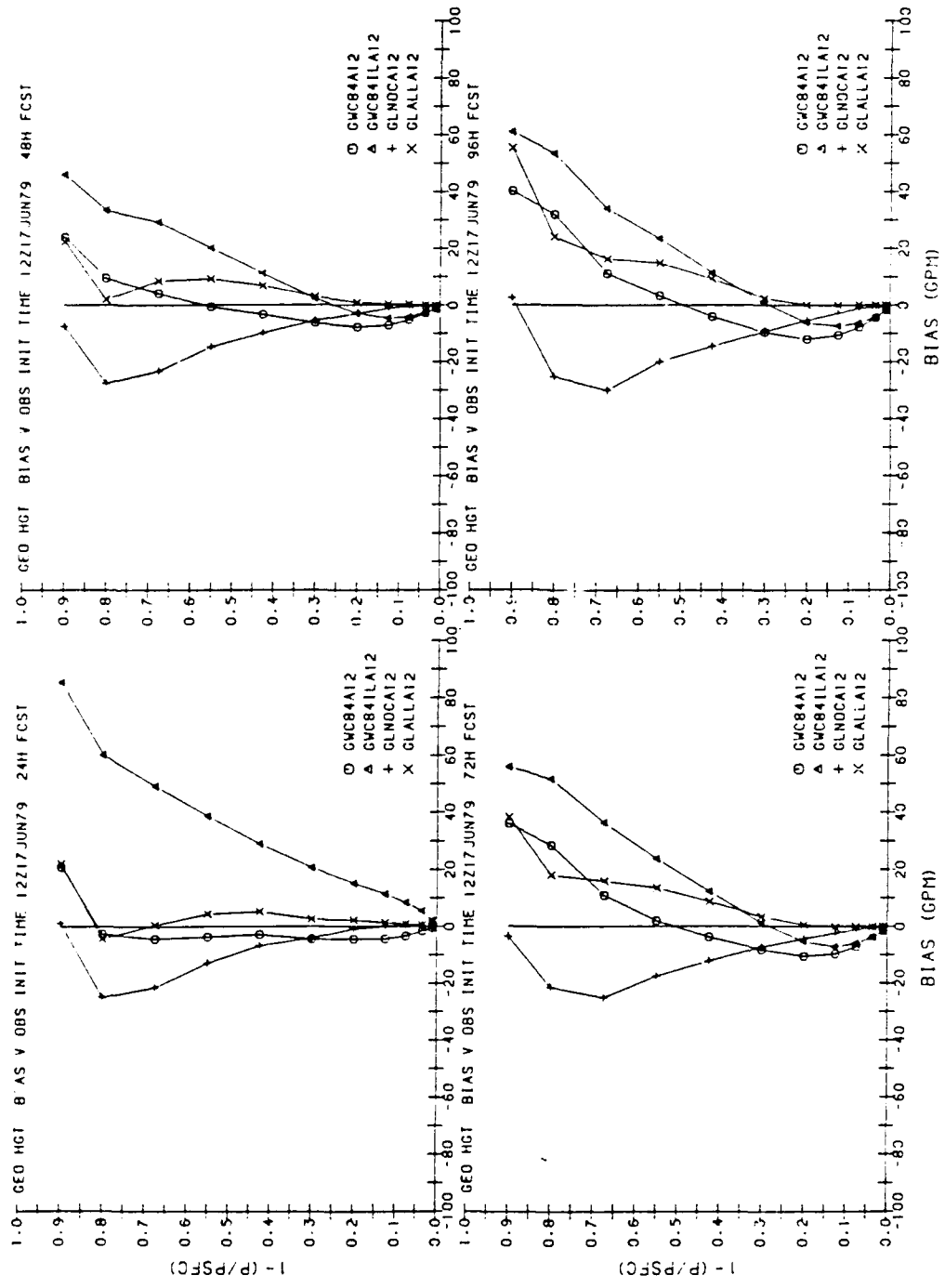


Figure 2. Geopotential Height Bias (m) of Four Versions of the GSM (GWC84, GWC84IL, GLNOC, GLALL) Initialized 1200 UTC 17 June 1979 When Evaluated Against the Global Radiosonde Network.

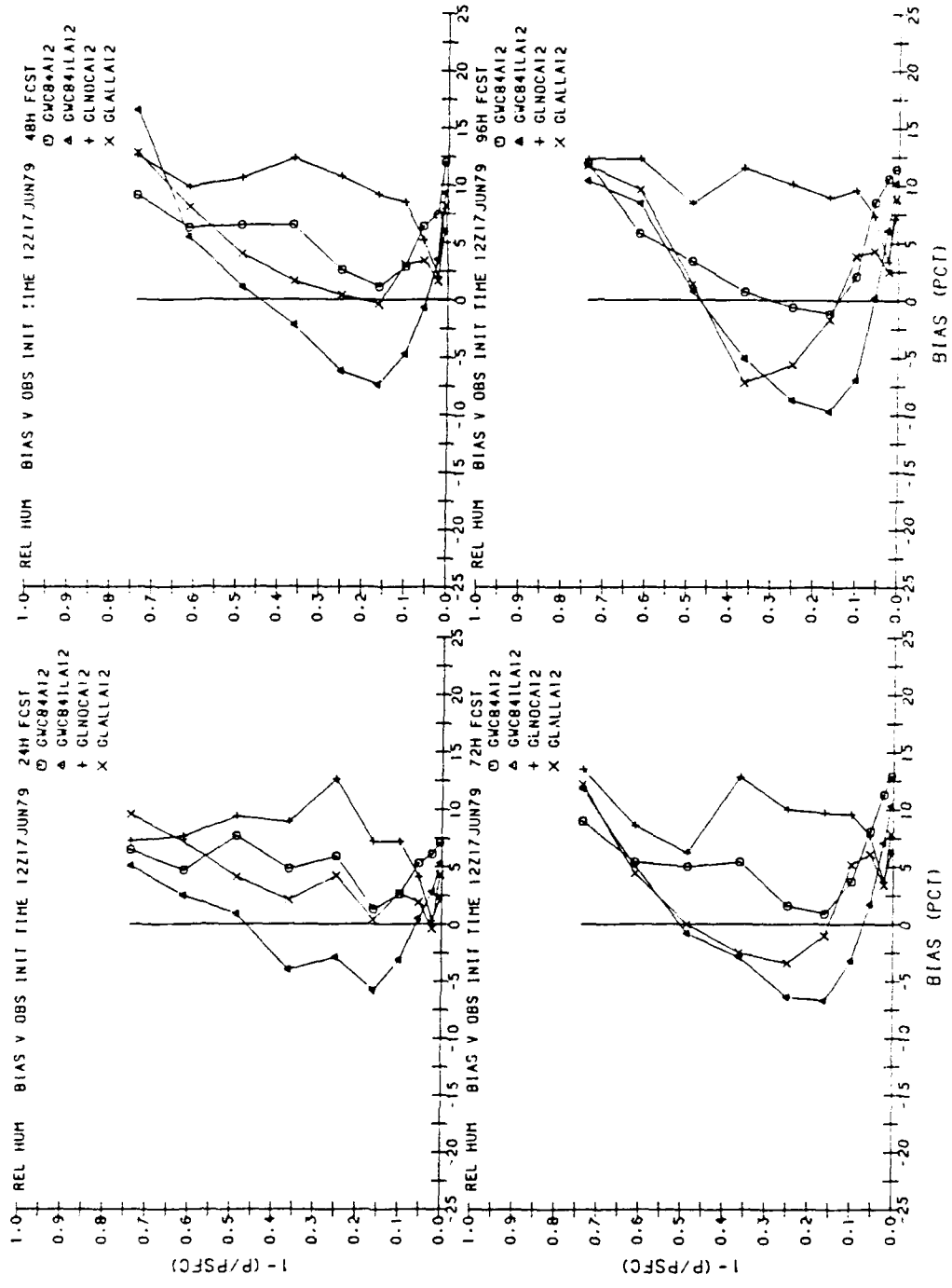


Figure 3. Relative Humidity Bias (percent) of Four Versions of the GSM (GWC84, GWC84IL, GLNOC, GLALL) Initialized 1200 UTC 17 June 1979 When Evaluated Against the Global Radiosonde Network.

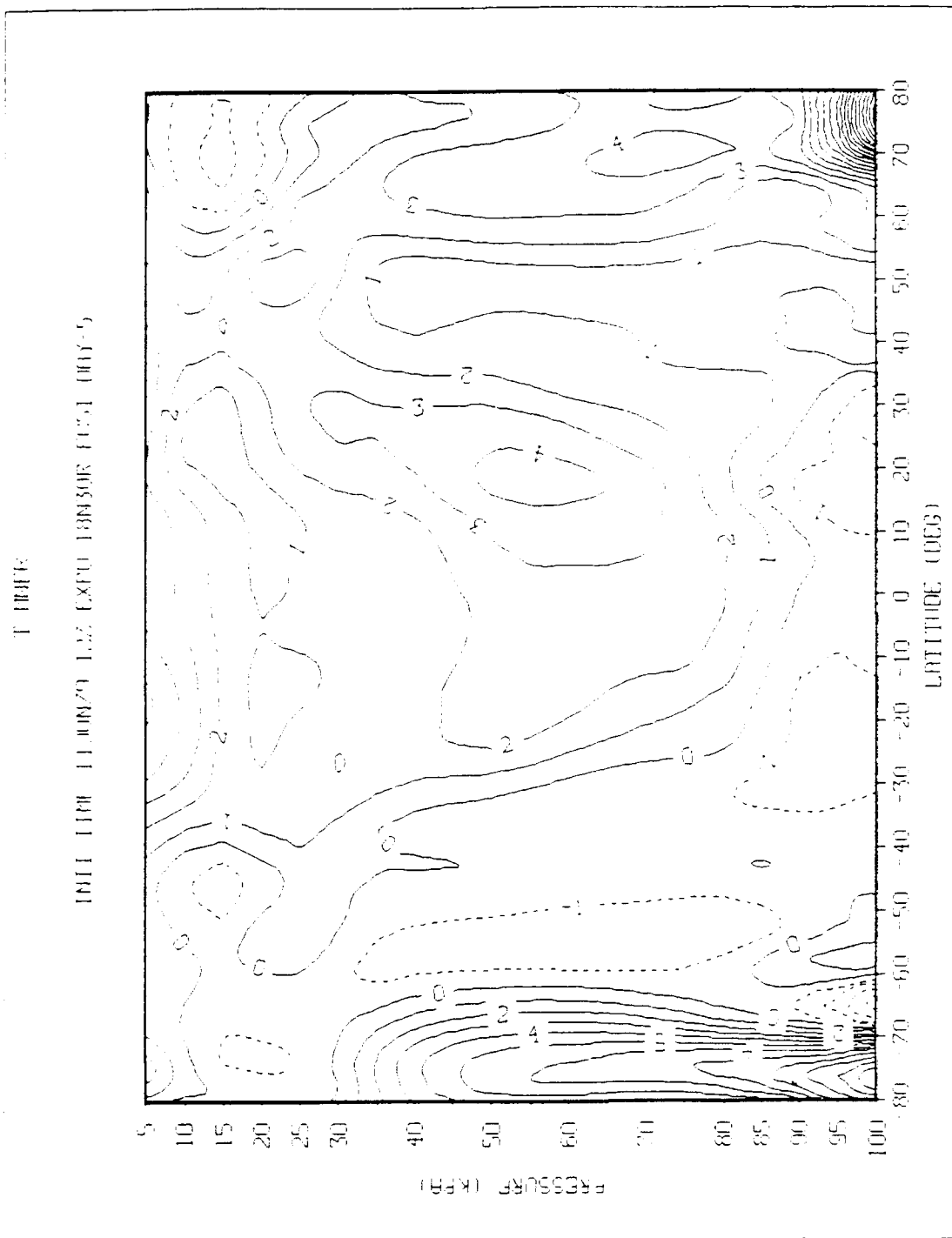


Figure 4. Forecast Day 5 Zonally-Averaged Temperature Bias (K) of GSM Experiment 0 (Original MODKUU) Initialized 1200 UTC 11 June 1979 When evaluated Against FGGE III-B Analysis.

R NMER

INIT TIME 11 JUN 79 12Z EXFO 18130R F051 00Y-5

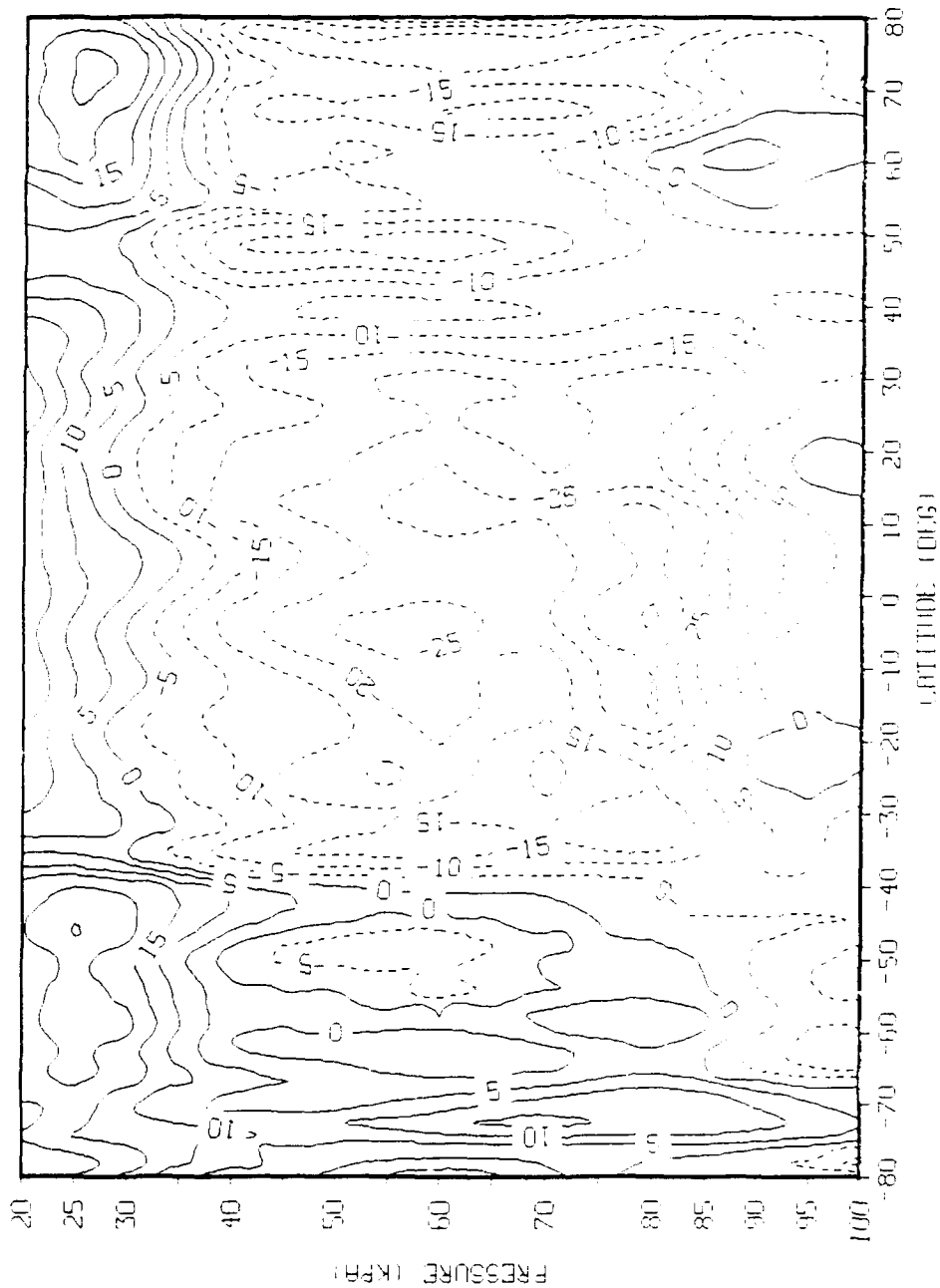


Figure 5. Forecast Day 5 Zonally-Averaged Relative Humidity Bias (percent) of GSM 12 Experiment 0 (Original MODK00) Initialized 1200 UTC 11 June 1979 When Evaluated Against FGGIE III-B Analysis.

precipitation forecasts. We were, on the one hand, encouraged by the GSMs ability to generate and sustain precipitation and, on the other, obviously concerned about its overabundance.

3.1 Code and Methodology Corrections

A central feature of the MODKUO algorithm is the calculation of cloud temperature and specific humidity, T_c and q_c respectively. In the University of Illinois code, it is assumed that the lowest model layer is saturated, therefore, the lifting condensation level exists there and it is used as the base of the moist adiabat to be computed. Values of T , q , and p (model layer pressure) in the lowest model layer are used to compute the equivalent potential temperature θ_e on which the moist adiabat is based. This is done whether the lowest model layer is saturated or not. In its first execution at a grid point, the moist adiabat algorithm (obtained in the original code from NMC), computes a table of values of temperature T as a function of specified increments of θ_e and p and a table of θ_e as a function of T and p . On subsequent passes through the algorithm, the T and p values of the lowest model layer (assumed to be saturated) are used to interpolate a value of θ_e from its table. This θ_e and the model sigma layer pressure values of the layers above the lowest model layer are then used to interpolate values of T from the temperature table. These temperatures represent the moist adiabat (cloud) temperatures T_c , and are used to compute the saturation (cloud) specific humidity values q_c . In each successive model layer, T_c is compared with the model's large-scale (predicted) temperature T . As long as $T_c - T > 0$, the layer in question is considered conditionally unstable and hence, a part of the cumulus cloud vertical domain. This comparison continues upward through the layers until two successive conditionally stable layers are found. The symbols KBOT and KTOP represent the lowest and highest model layers in this conditionally unstable domain (that is, the two stable layers are excluded) that represents the cumulus cloud. In the original code⁹, KBOT is always the second lowest model layer. In the tropics, KTOP was often found to be the model layer just below the tropopause.

In our examination of the MODKURO computer code, we discovered and corrected several design errors. First, two changes were made that generalized the computation of the cloud top sigma layer and avoided negative specific humidity. Next, we noted that the temperature difference between cloud and environment ($T_c - T$) was computed and used directly in the code rather than computing the potential temperature difference ($\theta_c - \theta$) and using it in the computation of the latent heat release rate as documented in Soong et al.⁹ (see their Eq. 11).

A problem that arose in the first extended global applications of the code was the production of excessive precipitation rates at single grid points for individual time steps. We traced the problem to very small values of the quantity $\langle \theta_c - \theta \rangle$, the vertically averaged potential temperature difference between cloud and environment. Since in Soong et al.⁹ the rate of release of latent heat is inversely proportional to $\langle \theta_c - \theta \rangle$, its very small value led to the enormous heating rates. After looking at the vertical $\theta_c - \theta$ profile at a problematic grid point, we noticed that this difference was zero everywhere except at one model layer, where the difference was small. The occurrence of such a small value of $\theta_c - \theta$ was made more likely by the entrainment scheme, which reduced the difference from its moist adiabatic value. If the averaged quantities $\langle \theta_c - \theta \rangle$ or $\langle q_c - q \rangle$ (the averaged specific humidity difference) are very small, this means that there need be no adjustment to the θ, q large-scale profiles because the large-scale atmosphere is essentially moist adiabatic already. To deal with this problem, we imposed minimum threshold values for $\langle \theta_c - \theta \rangle$ and $\langle q_c - q \rangle$ of 0.1 K and 0.01 g kg⁻¹ respectively. If either $\langle \theta_c - \theta \rangle$ or $\langle q_c - q \rangle$ are less than these threshold values, all of the available converged water vapor goes to moistening or heating. If both are less than their thresholds, the convective heating and moistening adjustments of the large-scale variables are not invoked.

Another coding problem discovered in the calculation of $\langle \theta_c - \theta \rangle$ and $\langle q_c - q \rangle$ involved their computation over the vertical domain of convective instability. In its original form, the code integrated these quantities by summing the product of the cloud-environment difference and the sigma thickness of the layer over just those layers where the difference was positive. This implies that the heat and moisture

represented by these integral quantities should only be distributed over layers where these quantities were positive. In fact, the heat and moisture should be distributed over the total volume of the cloud (KBOT to KTOP) and not just these positive value layers. Indeed, the Soong et al⁹ Eq. (13) indicates that the summed products $\Sigma(\theta_c - \theta)\Delta\sigma$ and $(q_c - q)\Delta\sigma$ are to be divided by $\Delta\sigma = \sigma_b - \sigma_t$. This error led to values of $\langle q_c - q \rangle$ and $\langle \theta_c - \theta \rangle$ which were too small by a factor of $\Delta\sigma_+ / \Delta\sigma_c$, where $\Delta\sigma_+$ is the summed depths of the positive layers, and $\Delta\sigma_c$ the summed depth of the layers between KBOT and KTOP inclusive. To correct for this error, the factors $\Delta\sigma_+ / \Delta\sigma_c$ and $\Delta\sigma_+ / \Delta\sigma_{+,\theta}$ were used to multiply the computed quantities $\langle q_c - q \rangle$ and $\langle \theta_c - \theta \rangle$ respectively. This had the effect of increasing the magnitude of these quantities, thus, reducing the resulting convective heating and moistening in the convectively unstable layers. A related error found and corrected allowed MKT (the layer corresponding to the empirical cloud-top pressure) to lie above KTOP, which improperly allowed consideration of convectively stable layers in the computation of the entrainment effect. We allowed MKT to be no higher than KTOP to correct this error. Then the amount of the entrainment effect is such that $\theta_c - \theta$ is just zero at MKT. This magnitude of entrainment effect is imposed from KBOT to the layer just below MKT. When $\theta_c - \theta$ is so modified, it really implies a decrease in θ_c , since the large-scale temperature is not affected by entrainment itself. Therefore, we introduced a recomputation of q_c based on the altered values of θ_c .

Two new threshold values were added to the code to deal with specific problems. The moisture convergence criterion for invoking the MODKUNO scheme was raised from zero to 0.5×10^{-6} to prohibit grid points with small moisture convergence values (such as those in the high latitudes) from being considered for moist convection processes. Secondly, the convective heating fraction, $1-b$, in the Krishnamurti et al¹⁵ closure scheme was forced to be bounded by a value of 1.0 as a maximum value. A value of the convective heating fraction greater than 1.0 was often realized, especially in tropical regions, yielding excessive drying of the environment. Less frequently, the original scheme computed a negative value. Thus, the scheme was also modified to

skip over the convective heating and moistening adjustment of the large-scale variables in this case.

Incorporating all of the changes described above resulted in, for the 11 June 1979 case, globally-averaged rainfall rates of about 6 mm/day compared to about 9 mm/day for the original MODKUU and a climatological global-average precipitation rate for June of about 3 mm/day. The temporal distributions of global precipitation rates for the five-day forecasts are displayed in Figure 6. These distributions depict a diurnal signal that will be discussed later in this report. Convective processes contributed at least 80 percent of the total precipitation when either form (original or corrected) of MODKUU was used in the GSM.

Figures 7 and 8 represent, respectively, the cross-section of zonal-average mean temperature and RH forecast error (at Day-5) for the corrected MODKUU experiment (experiment G). In the plot of zonally-averaged temperature, we now see regions of cold bias in the tropics, as much as 2 to 3 K. In general, a cold bias exists through almost the entire depth of the tropical troposphere south of about 20°N latitude. Two cold bias maxima occur: one at 90 kPa that extends throughout the tropics, and one just above 40 kPa where it is confined to the very low latitudes. Another major region of cold bias exists at 50-60°S, but this is probably not directly related to moist convective processes. In the RH plot, negative biases as large as 25 percent are evident. The RH bias maxima in the tropics appear primarily at two levels: throughout the low latitudes at 80 kPa, and around 10-20°N from 35 to 65 kPa.

We next focused on the entrainment formulation⁹ which is invoked for each grid point. It begins with a computation of the empirically-based cloud-top pressure which is a function solely of partition parameter (b) and sets the entrainment-based cloud-top at levels as high as 20 kPa (for b=0) and as low as 90 kPa (for b=1). Deep convection in the tropics commonly rises higher than the 20 kPa level, bringing into question the validity of a formulation that limits cloud-tops to 20 kPa. In our model run of 17 June 1979, we diagnosed the computed values of convective heating fraction in a convectively active region of tropical western Africa. The precipitation rates and convective heating fraction values for four model grid points in this region are shown

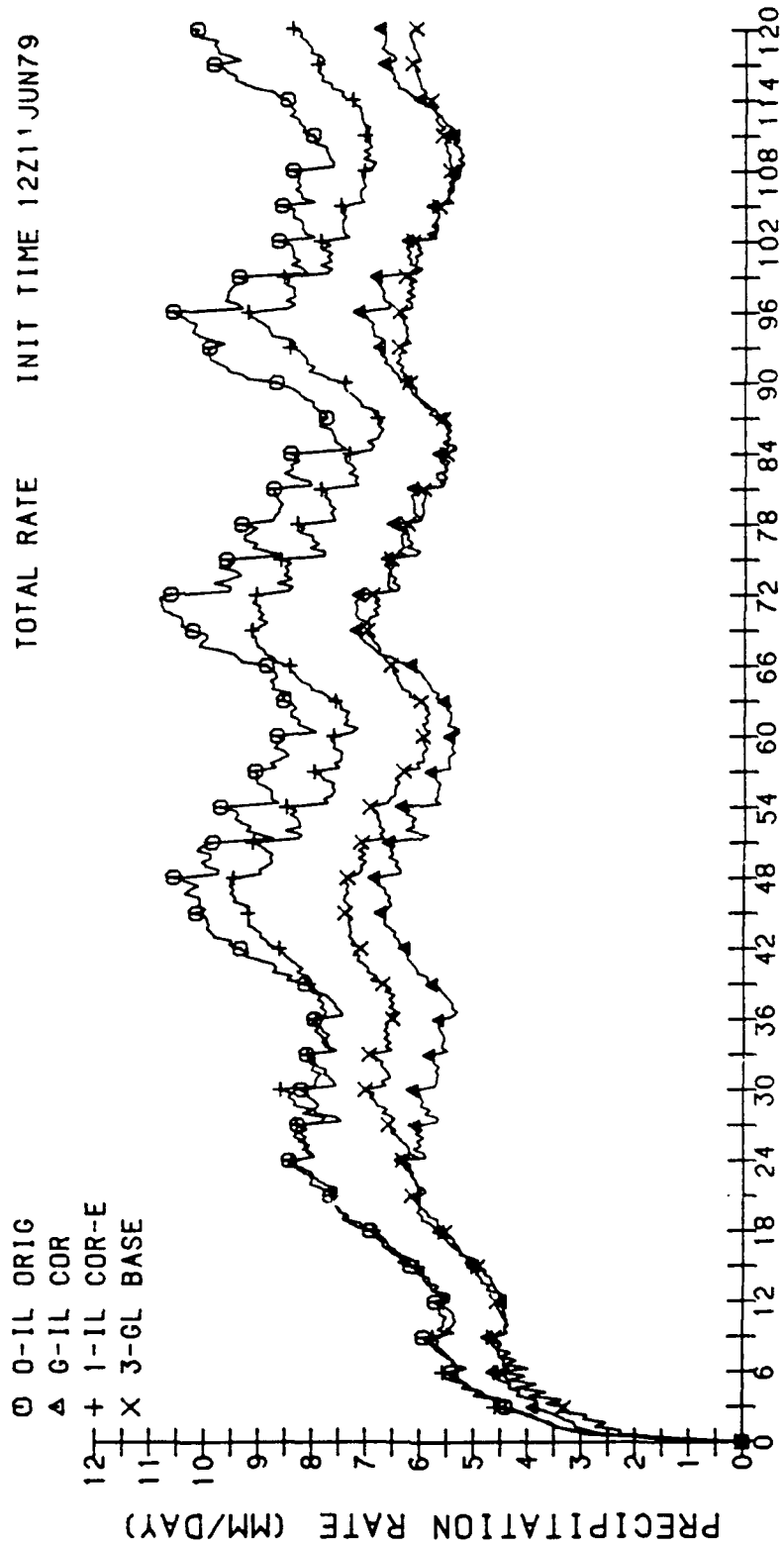


Figure 6. Globally-Averaged Total Precipitation Rates (mm day⁻¹) for Four Versions of the GSM (Exp. 0,G,1,3) Initialized 1200 UTC 11 June 1979.

T MINER

INIT TIME 11 JUN 79 12Z EXFG 18N30R FCST DAY-5

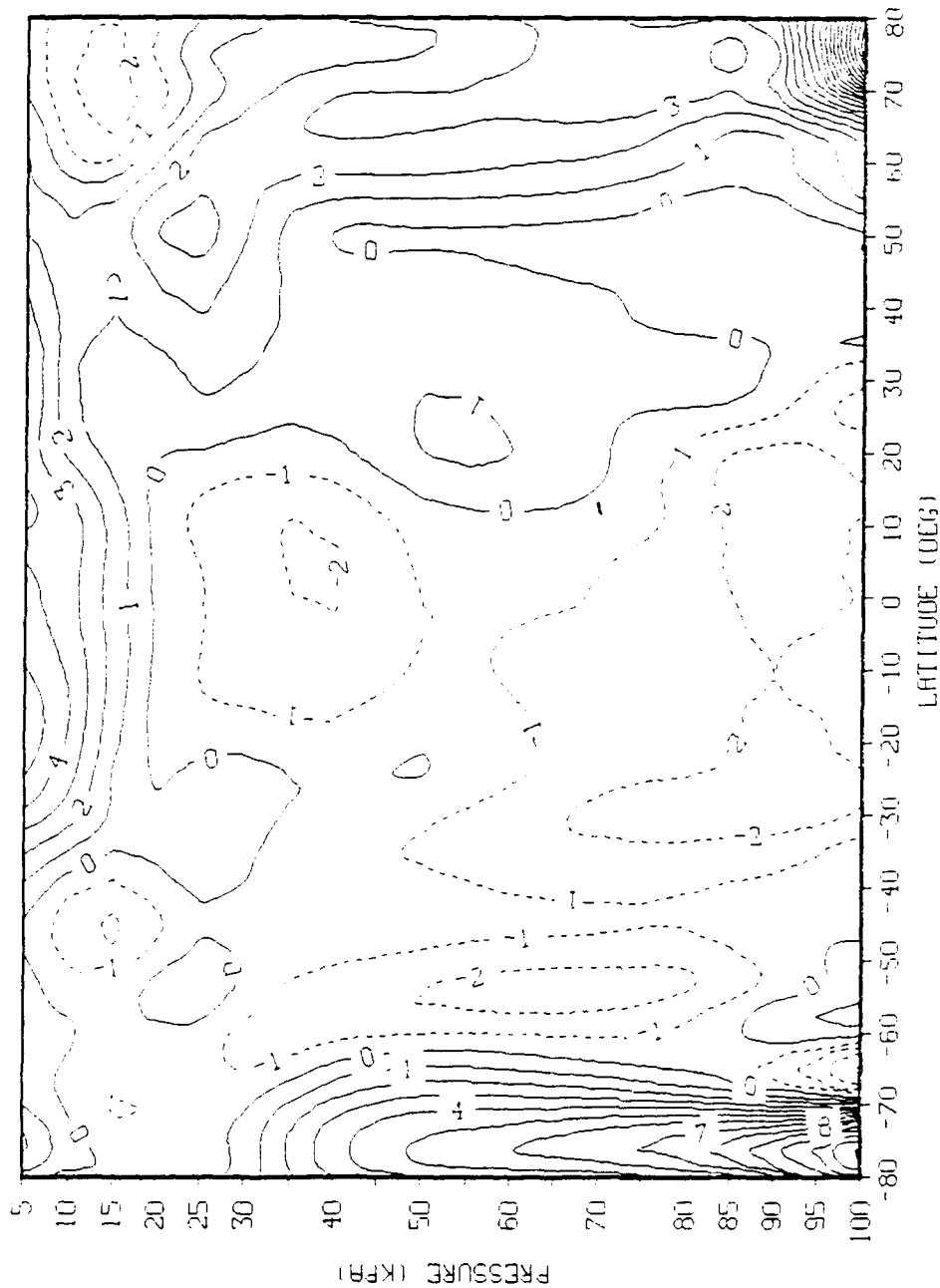


Figure 7. Forecast Day 5 Zonally-Averaged Temperature Bias (K) of GSM Experiment G (Corrected MODKUU) Initialized 1200 UTC 11 June 1979 When Evaluated Against FGGE III-B Analysis.

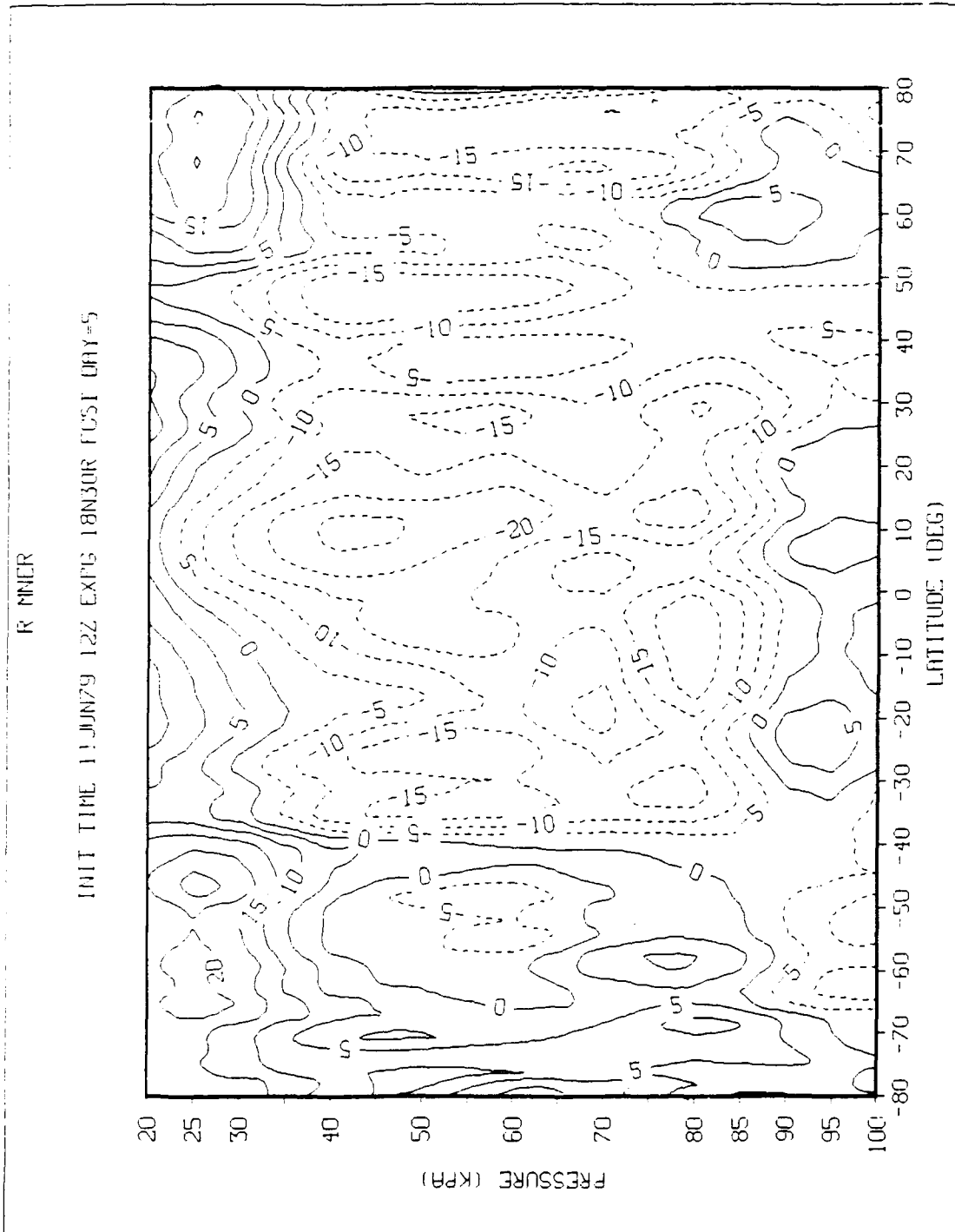


Figure 8. Forecast Day 5 Zonally Averaged Relative Humidity Bias (Percent) of GSM 19 Experiment G (Corrected MODKUG) Initialized 1200 UTC 11 June 1979 When Evaluated Against FGGE III-B Analysis.

in Figures 9 and 10 respectively. During the period of high precipitation rates depicted in Figure 9, especially forecast hours 24 to 48, computed values of convective heating fraction ranged between 80 and 90 percent. Using the empirical P_T formulation, cloud-tops are limited to the 34.5 and 26.7 kPa range. By contrast KTOP, the highest level of conditional instability, was regularly observed to lie at the model layer represented by a nominal pressure of 12.5 kPa. Thus, for areas of deep convection, the entrainment formulation eliminated convective heating between 35 and 12.5 kPa; this explains the cold bias maximum centered near 35 kPa in the tropics in Figure 7.

A simple alternative was to modify MODKUO by turning off the entrainment effect. We would thus expect the global precipitation rate to increase with respect to the corrected MODKUO (shown as G-IL COR in Figure 6). The increase is reflected in the curve labeled 1-IL COR-E in which the globally-averaged precipitation rate is 8 mm/day. The corresponding zonal cross-sections of five-day forecast temperature and RH mean error in Figures 11 and 12 reveal the effects on the large-scale fields of withholding the entrainment formulation. Now a warm bias of greater than 4 K exists in the tropical upper troposphere where a cold bias existed with entrainment. The upper one-half of the tropical troposphere is warmed from significant latent heating at these levels. This warming and accompanying drying of the large-scale atmosphere has resulted in a negative RH bias of over 30 percent as shown in Figure 12.

Recall the moist adiabat computation included in the original MODKUO⁹ used the lowest model layer as the lifting condensation level (LCL) in all cases. Furthermore, values of $\theta_e(T)$ (equivalent potential temperature as a function of temperature) and $T(\theta_e)$ were interpolated from tables using ad hoc and (to us) unclear computations. Therefore, we next devised routines to compute the pressure of the LCL (P_{lcl}) given the temperature, specific humidity, and pressure of the lowest model layer and to calculate the temperature and specific humidity along the moist adiabat, based on the θ_e value corresponding to P_{lcl} . In both routines, basic thermodynamic principles were

CONVECTIVE PRECIP.
INIT TIME 12Z17JUN79

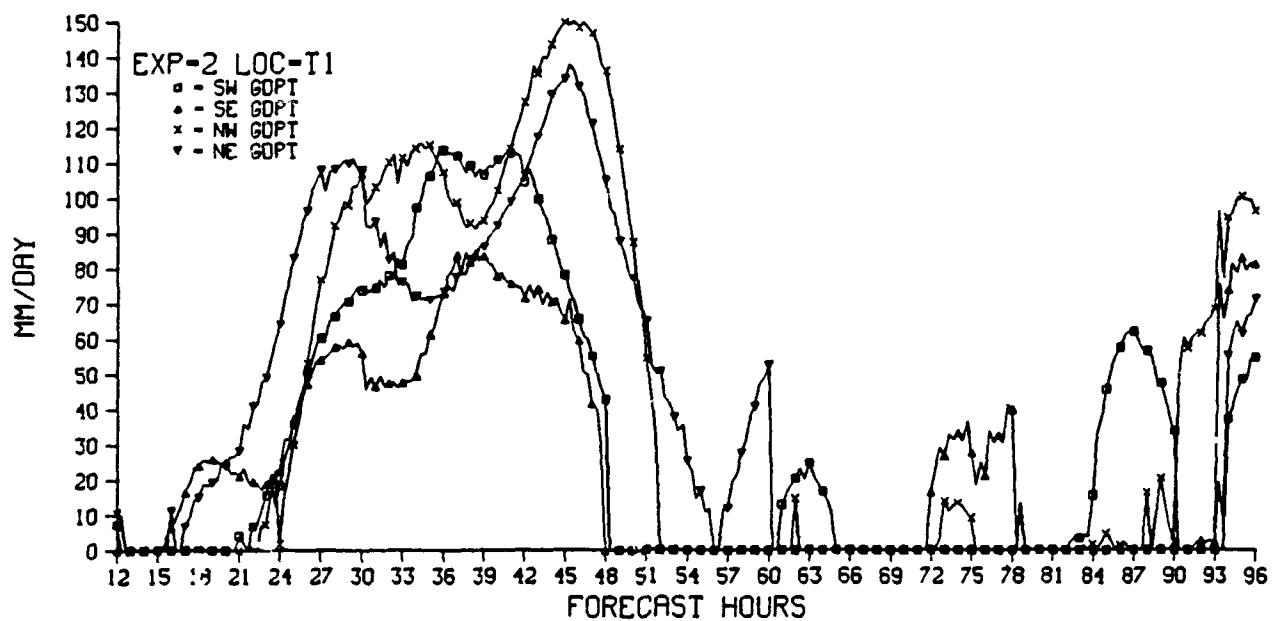


Figure 9. Convective Precipitation Rates (mm day⁻¹) Over Four Grid Points in Western Africa from GSM Experiment 0 (Original MODKUU) Initialized 1200 UTC 17 June 1979.

CONVECTIVE HING FRAC
INIT TIME 12Z17JUN79

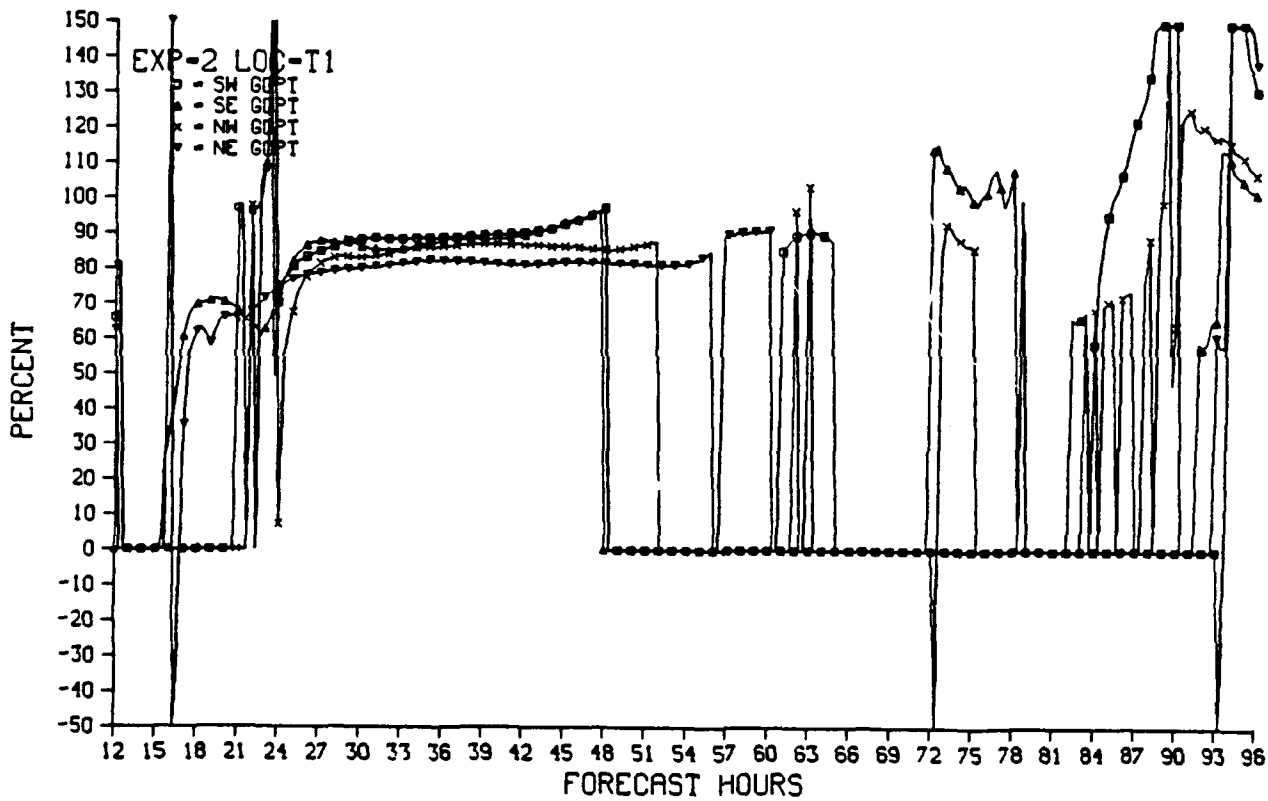


Figure 10. Convective Heating Fraction (percent) Over Four Grid Points in Western Africa from GSM Experiment 0 (Original MODKUO) Initialized 1200 UTC 17 June 1979.

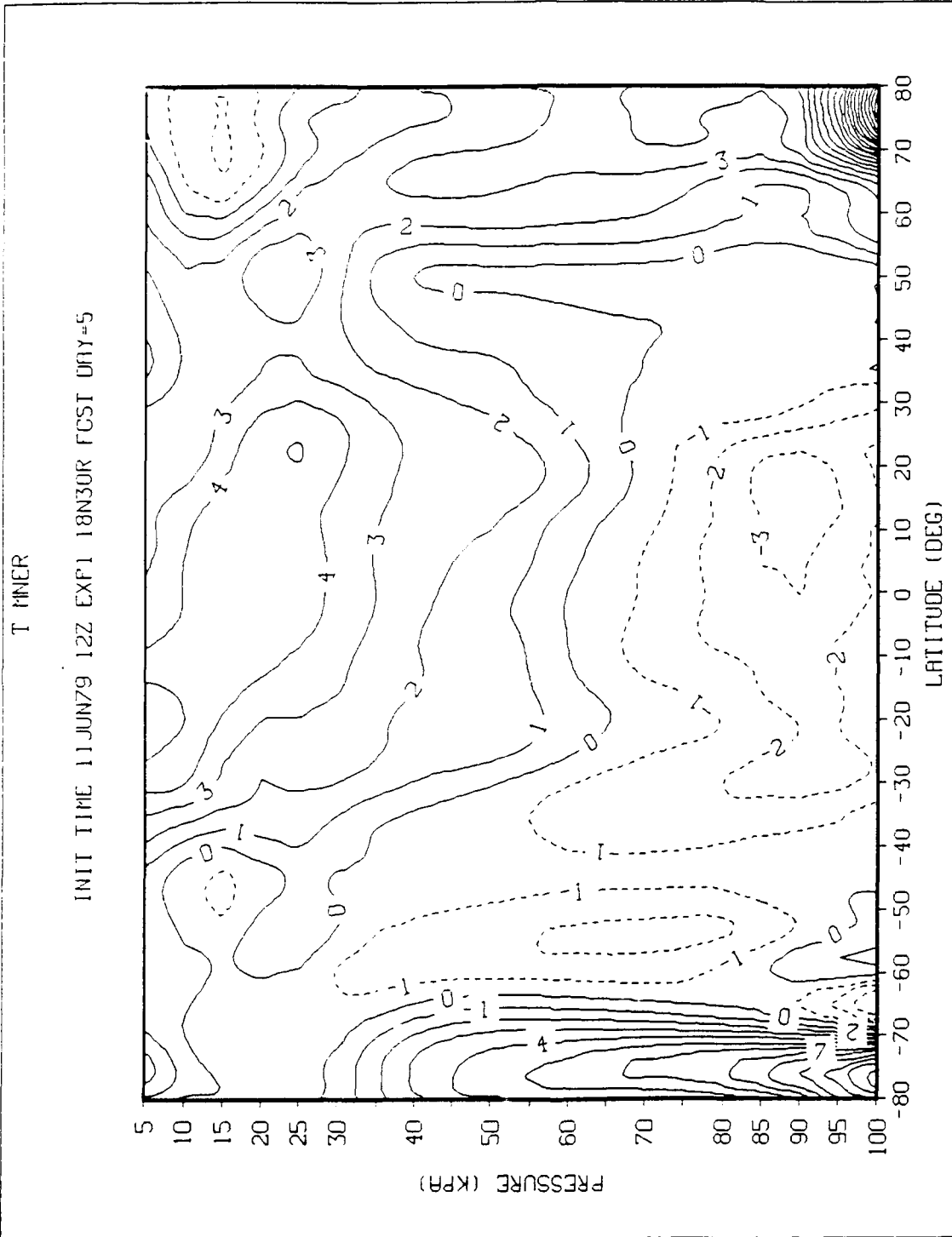


Figure 11. Forecast Day 5 Zonally-Averaged Temperature Bias (K) of GSM Experiment 1 (Corrected MODK10 Without Entrainment) Initialized 1200 UTC 11 June 1979 When Evaluated Against FGGE III-B Analysis.

R MNER

INIT TIME 11JUN79 12Z EXP1 18N30R FCST DRY=5

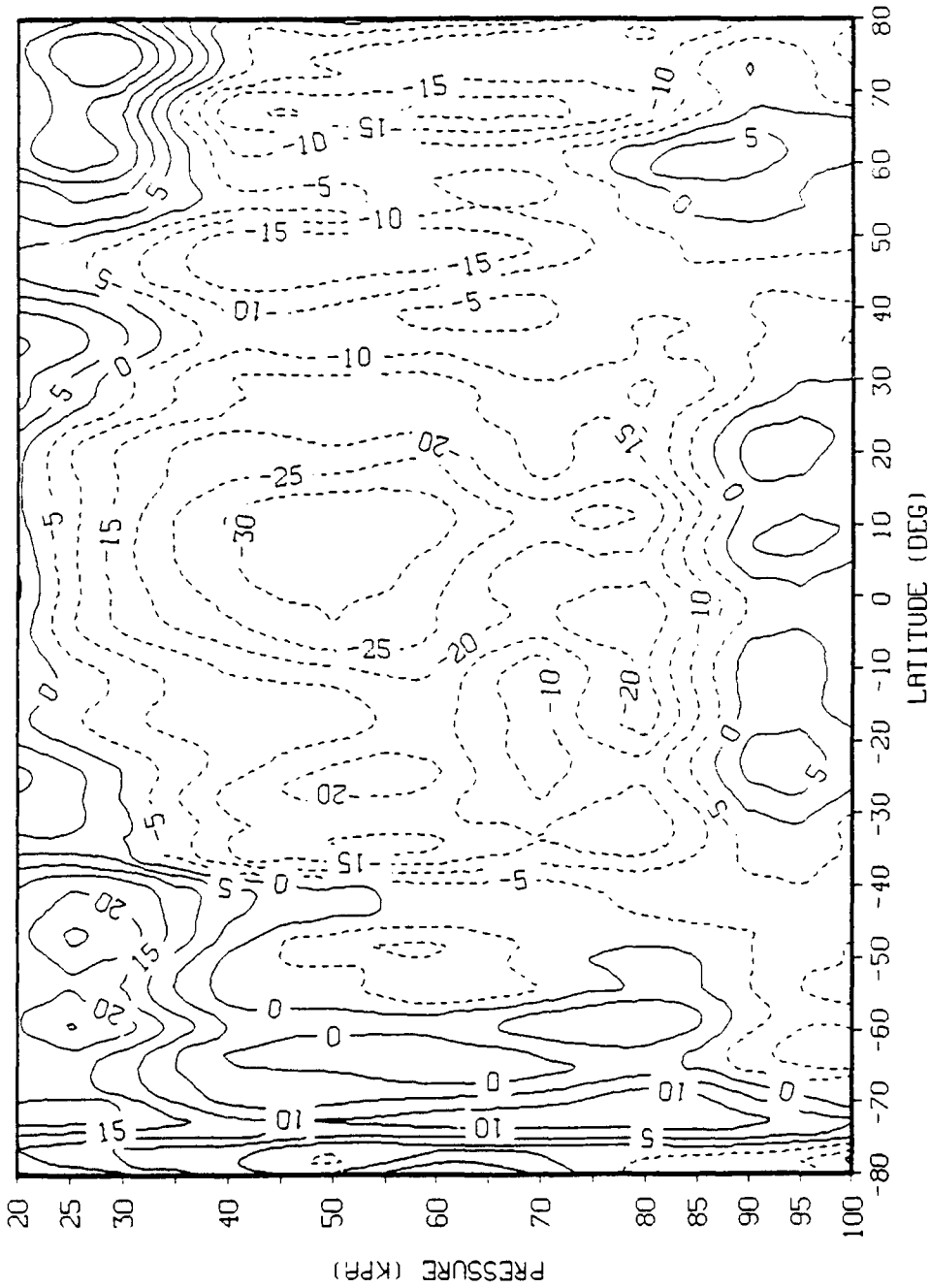


Figure 12. Forecast Day 5 Zonally-Averaged Relative Humidity Bias (percent) of GSM 24 Experiment 1 (Corrected MODK10 Without Entrainment) Initialized 1200 UTC 11 June 1979 When Evaluated Against FGGE III-B Analysis.

used as described by Yang and Norquist.¹⁶ While the base model level for the computation of the LCL can be varied, Slingo et al¹⁷ found that in their Kuo convection scheme the most realistic results were obtained using the lowest model layer.

With these changes, we should expect cloud temperatures no warmer, and in many cases cooler, than in the original version which, in turn, should lead to reduced overall convective activity. Again referring to Figure 6, these changes yielded a globally-averaged precipitation rate of about 6 mm/day (see curve labeled 3-GL BASE). The resulting zonal cross-sections of five-day forecast temperature and RH mean error are shown in Figures 13 and 14. The tropospheric warm bias is now only 2 K in the tropical upper troposphere while an enhanced region of cold bias of more than 2 K appears at 30°S latitude. Corresponding to the generally cooler atmosphere are the more moist low latitudes as seen in Figure 14. The maximum dry bias now is about 25 percent, and at 30°S the zonal mean is only about 5 percent too dry.

3.2 Impact of Deficiency Corrections-Summary

In a comparison of the four curves of globally-averaged precipitation rates in Figure 6, we can see the effects of our attempt to correct MODKURO deficiencies. The corrected MODKURO (labeled experiment G-IL COR) reduced the global rate from 9 to 6 mm/day. We attribute most of this reduction to the imposition of the latent heat release on all of the cumulus column rather than to just those layers where $T_c - T > 0$ after entrainment. In so doing, the effect on the large scale temperature of any given model layer is lessened. This can be seen by comparing Figures 4 and 7, the zonal mean temperature forecast errors for experiments O and G respectively

¹⁶Yang, C.-H., and Norquist, D. (1990) An assessment of a moist convection parameterization through a comparison of scheme-generated clouds with observational statistics, submitted to *Weather and Forecasting*.

¹⁷Slingo, J.M., Mohanty, U.C., Tiedtke, M., and Pearce, R.P. (1988) Prediction of the 1979 summer monsoon onset with modified parameterization schemes, *Mon. Wea. Rev.*, **116**:328-346.

T MINER

INIT TIME 11JUN79 12Z EXP3 18N30R FCST DAY=5

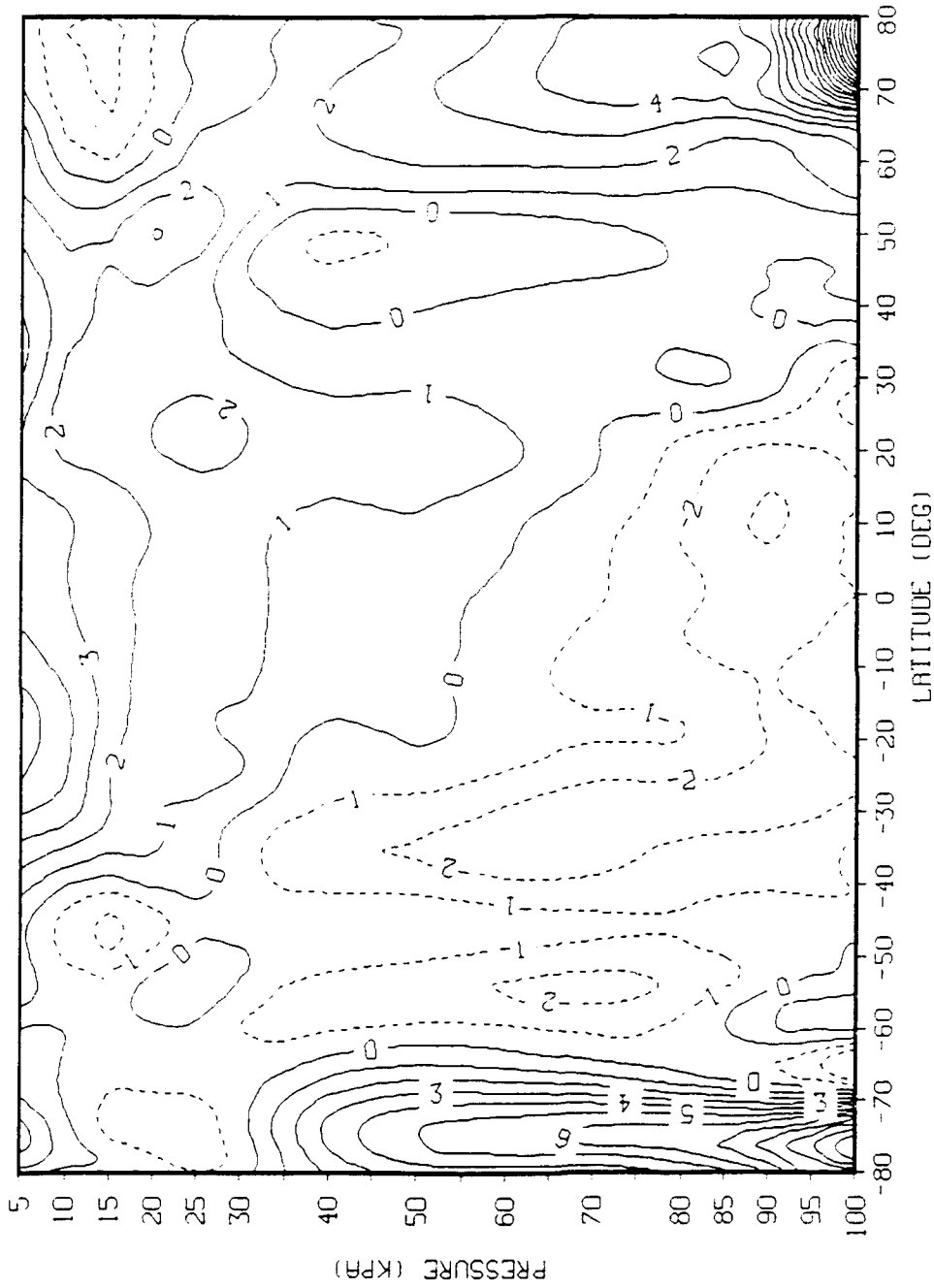


Figure 13. Forecast Day 5 Zonally-Averaged Temperature Bias (K) of GSM Experiment 3 (GL Baseline) Initialized 1200 UTC 11 June 1979 When Evaluated Against FGGE IIIB Analysis.

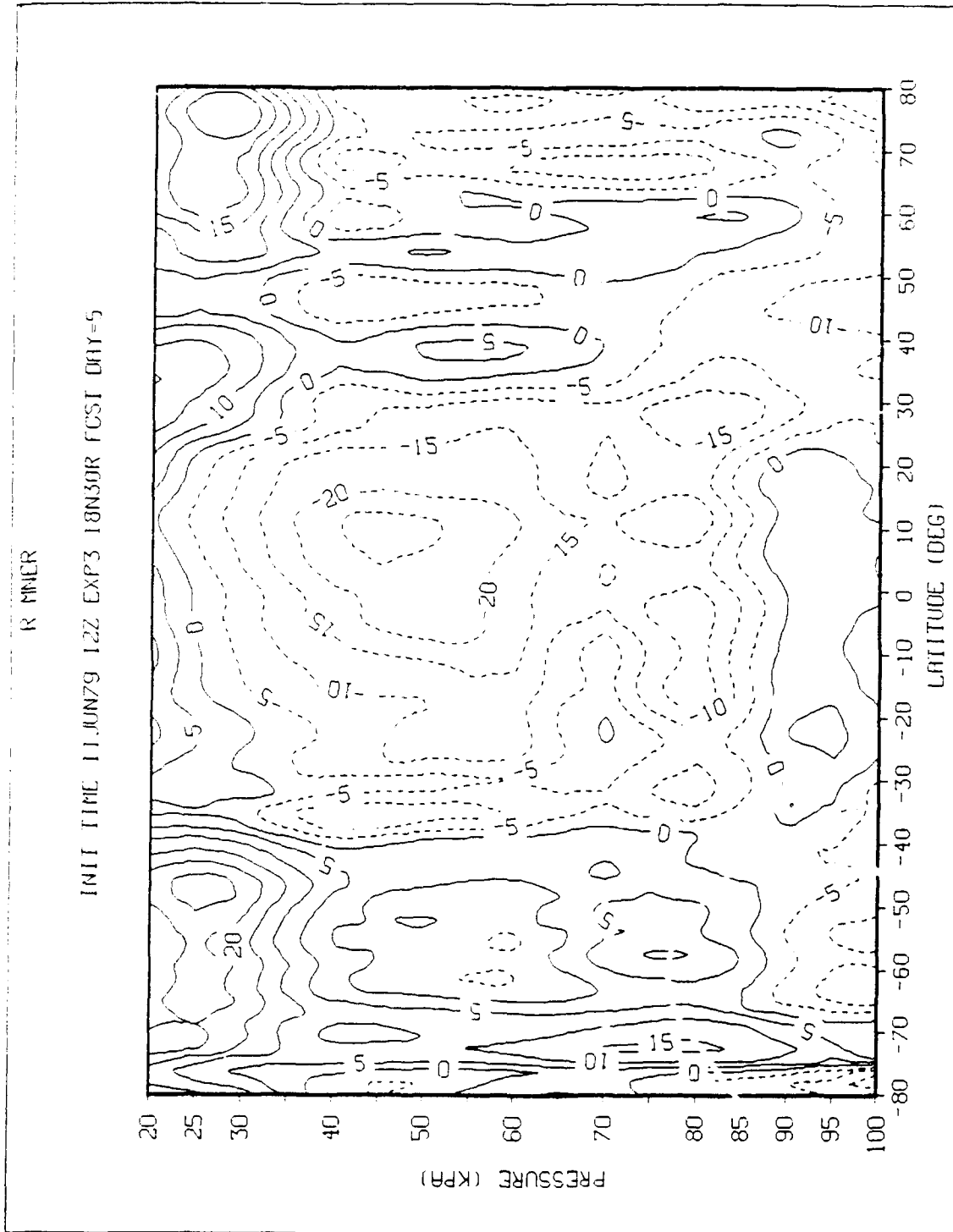


Figure 14. Forecast Day 5 Zonally-Averaged Relative Humidity Bias (percent) of GSM 27 Experiment 3 (GL Baseline) Initialized 1200 UTC 11 June 1979 When Evaluated Against FGGE III-B Analysis.

(original and corrected MODKUU). The latter plot shows tropical zonal means up to 3 K cooler than the original MODKUU. Since precipitation in the algorithm is effectively represented by the vertically-integrated latent heat release, the convective precipitation was reduced accordingly.

The entrainment formulation of the original scheme⁹ was found to be the cause of a tropical upper troposphere cold bias. While computed cloud top pressures for deep convection were found to be typically greater than 30 kPa, the entrainment algorithm was effectively eliminating convective heating of the upper troposphere by setting the latent heating above this computed cloud top pressure to zero. When the entrainment formulation was switched off, the T_c-T difference computed originally from the moist adiabat was not reduced. This led to greater cumulus heating and precipitation. A comparison of Figures 7 and 11 indicate that most of the increased convective heating occurs at the upper levels, above 50 kPa. This is because the entrainment formulation reduces T_c-T at a rate that increases with decreasing pressure. Thus, the effect of removal of the entrainment formulation is an increased latent heating that is greater in the upper layers than it is in the lower layers. The increased latent heating eliminated the upper tropospheric cold bias (see Figure 11) and produced a greater globally-averaged precipitation rate (see Figure 6).

Finally, we changed the code to include a computation of the LCL and put in a new moist adiabat computation. With the LCL allowed to be higher than the lowest model layer, the moist adiabat temperatures will be cooler than in the original MODKUU. For this reason, T_c-T will generally be reduced overall and the latent heating reduced to a more physically reasonable level. Both the globally-averaged precipitation rate (Figure 6) and the zonal mean temperature (Figure 13) of experiment 3 reflect this reduction with respect to experiment 1. For example, tropical zonal mean temperatures are reduced as much as 3 K at upper levels and the precipitation rate is reduced from 8 to 6 mm/day.

3.3 Modifications to Improve the Methodology

The corrections made to MODKUO produced a desired (partial) reduction in the overactivity of the code. However, the 6 mm/day globally-averaged precipitation rate was still twice the climatological mean. It should be noted that the convective precipitation rate for the GL Baseline (experiment 3) version of the code is about 4.5 mm/day. Thus, just the convective portion of the total precipitation exceeds climatology. This fact encouraged more study of MODKUO rather than LRGSCS, the routine that parameterizes large-scale (stratiform) precipitation processes.

Soong et al⁹ included a scheme that allowed falling convective precipitation to evaporate in layers that were not saturated. Based on their tests, it was their conclusion and recommendation to turn off the evaporation scheme. Because the GL Baseline version of the MODKUO was producing too much convective precipitation, we decided to experiment with the impact of including an evaporation scheme. We considered two schemes which are described below.

The convective precipitation evaporation scheme⁹ was drawn from an earlier version of the NMC global spectral model¹. Its calculation starts with the topmost cloud layer. Each layer's computed convective temperature adjustment T_c is multiplied by the ratio of specific heat of air at constant pressure to latent heat of vaporization and by the model sigma layer thickness to determine its contribution to the precipitation falling out of that layer. This precipitation is added to the net precipitation from the layers above and the layer is then checked to see if the convectively adjusted specific humidity is less than 80 percent of the saturation specific humidity. If so, that portion of the net precipitation necessary to increase the relative humidity to 80 percent is evaporated into the layer. MODKUO makes a corresponding adjustment to reduce the adjusted layer temperature and increase the adjusted layer specific humidity. Whatever net precipitation is left after all layers are considered constitutes the model-generated convective precipitation. We shall refer to the GL Baseline version of MODKUO configured with this scheme as NMC EVAP.

The NMC evaporation scheme discussed above makes the implicit assumption that the grid box water vapor deficit (the difference between 80 percent of saturation specific humidity and grid box specific humidity) is available to receive the evaporation of cumulus precipitation. In comparing the grid box water vapor deficit to the net precipitation in a layer, we could alternatively consider only that portion of the grid box water vapor deficit into which the *cloud process* can evaporate water. The grid box water vapor deficit represents an amount of water that can be taken up by evaporation over the *entire grid area*. We altered the NMC evaporation scheme by multiplying this deficit by the fractional coverage of cumulus in the grid box to represent the amount of water that can be taken up by evaporation of the falling cumulus precipitation. This fraction of the grid box water vapor deficit more properly represents the amount of cumulus precipitation that can be evaporated into the layer.

The fraction of a grid square covered by cumulus in a time interval of cloud formation is given by Soong et al⁹ as

$$a = M_t \frac{\Delta\tau}{M_c} \quad (1)$$

where $M_t = \Delta q/\Delta t$ is the moisture convergence into the grid box and

$$M_c = g^{-1} \int_{PTOP}^{PBOT} [(c_p/L)(T_c - T) + q_c - q] dp \quad (2)$$

In the above equation, PBOT, PTOPT represent the bottom and top (in pressure units) of the cloud, g is the acceleration due to gravity, c_p is the specific heat of air at constant pressure, and L is the latent heat of vaporization. M_c represents the amount of moisture needed to fill the grid square with convective clouds.

Alternatively in the ECMWF Research Manual 3¹⁸, the cumulus cloud cover is

$$a = (1 - b)\Delta q \frac{\Delta\tau}{M_{cT}} \Delta t \quad (3)$$

where M_{cT} is just the portion of M_c due to condensational heating. Since convective heating $1-b$ represents just the portion of moisture convergence M_i that actually leads to cumulus cloud formation (that is, latent heating), the Soong et al.⁹ form and the ECMWF form are theoretically consistent. The ECMWF form was used in the GL Baseline version of MODKUO that we shall refer to as GL EVAP. We used a prescribed $\Delta\tau$ value of 1800 s. The model time step Δt is 1200 s for the 30 wave rhomboidal truncation version.

NMC EVAP and GL EVAP were used to generate five-day forecasts beginning with the 1200 UTC 11 June 1979 initial conditions. The globally-averaged precipitation rates for these configurations as well as the GL Baseline configuration are plotted in Figure 15. The global rates for the last four days of the forecast (avoiding the "spin-up" in the first day) are about 4.25, 4.5, and 6 mm/day for NMC EVAP, GL EVAP, and GL Baseline respectively. Much of the diurnal signal is damped out of the plots when the EVAP algorithms are used. In all three experiments, the precipitation is maintained at a reasonably steady level throughout the forecast period.

Figures 16 and 17 show the zonal mean five-day forecast errors for temperature and RH in experiment 4 (GL EVAP). Figures 18 and 19 depict the same zonal mean errors for experiment 5 (NMC EVAP). In both temperature error plots, it is clear that cold temperature biases prevail throughout the convectively active latitudes (50°S to 50°N) below 30 kPa. A region of cold bias greater than 3 K at 10-20°N present in experiment 3 (see Figure 13) has enlarged in experiments 4 and 5. As in experiment 3, warm biases of greater than 2 K are evident in the upper tropical troposphere. Related to the lower and middle tropospheric cold bias is the positive

¹⁸Research Manual 3, ECMWF Forecast Model, Physical Parameterization (1984) ECMWF Research Department, Ref:M1.6/2.

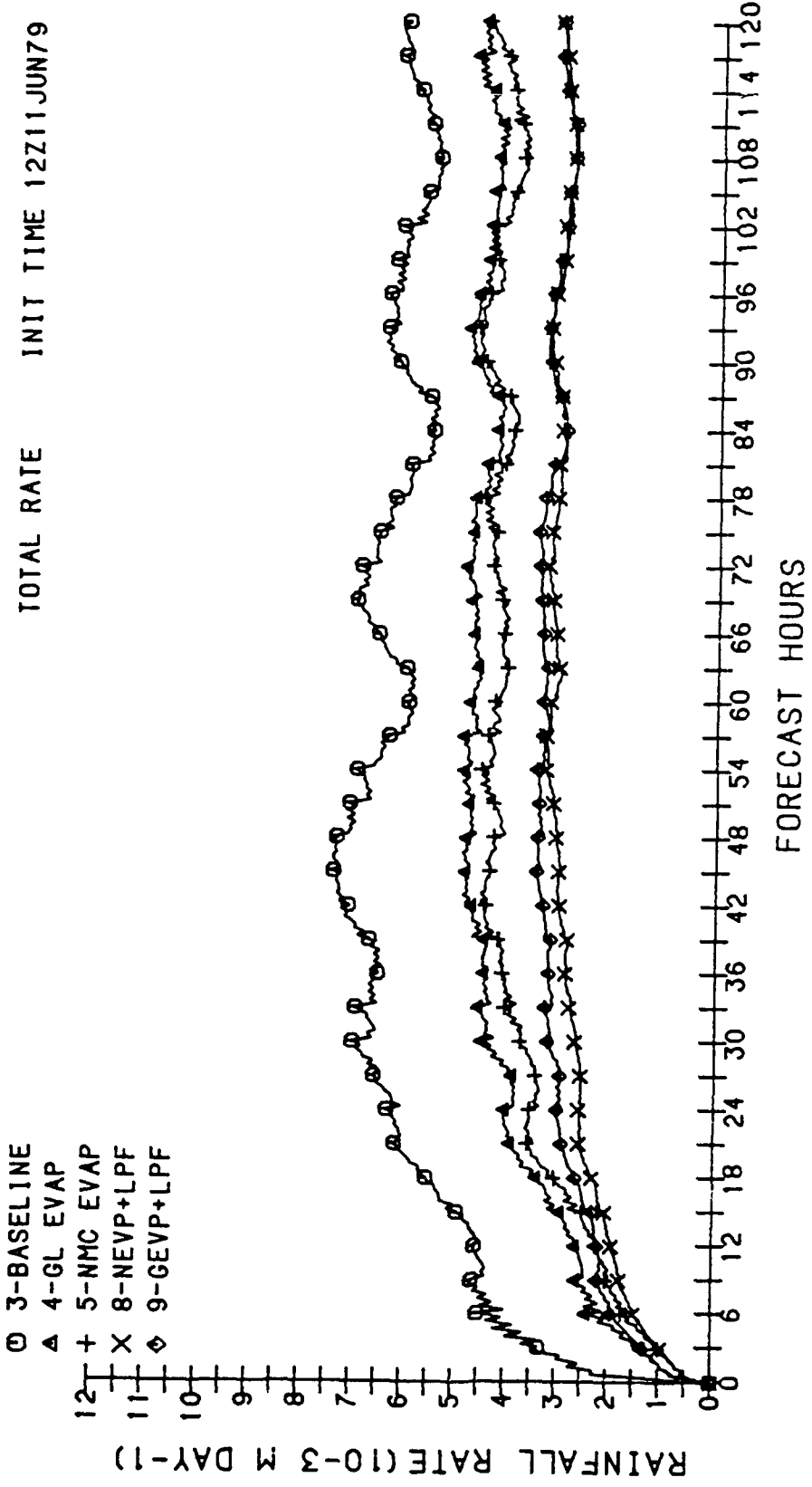


Figure 15. Globally-Averaged Total Precipitation Rates (mm day⁻¹) for Five Versions of the GSM (Exp. 3,4,5,8,9) Initialized 1200 UTC 11 June 1979.

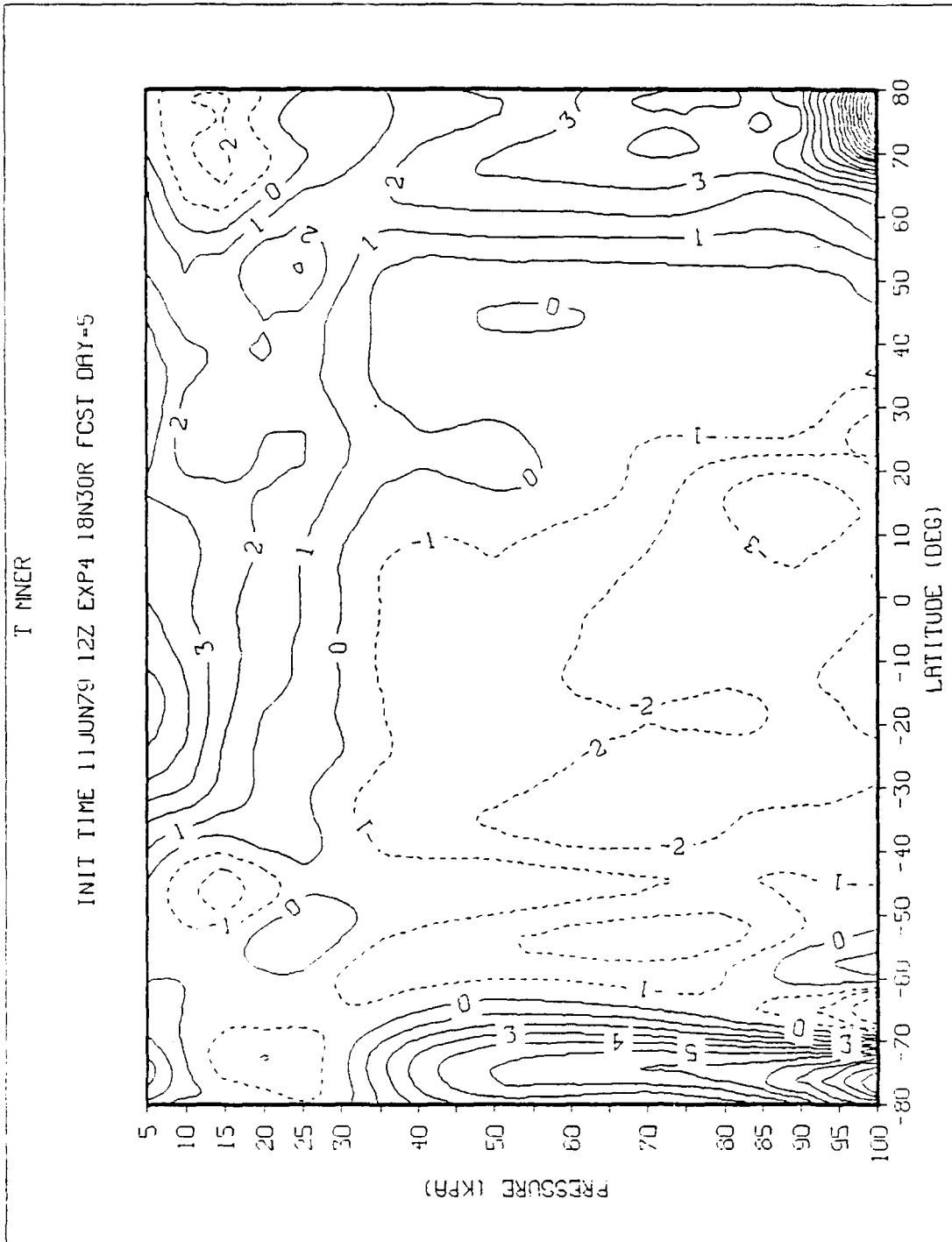


Figure 16. Forecast Day 5 Zonally-Averaged Temperature Bias (K) of GSM Experiment 4 (GL Evap) Initialized 1200 UTC 11 June 1979 When Evaluated Against FGGE III-B Analysis.

R MNER

INIT TIME 11JUN79 12Z EXP4 18N30R FCST DAY-5

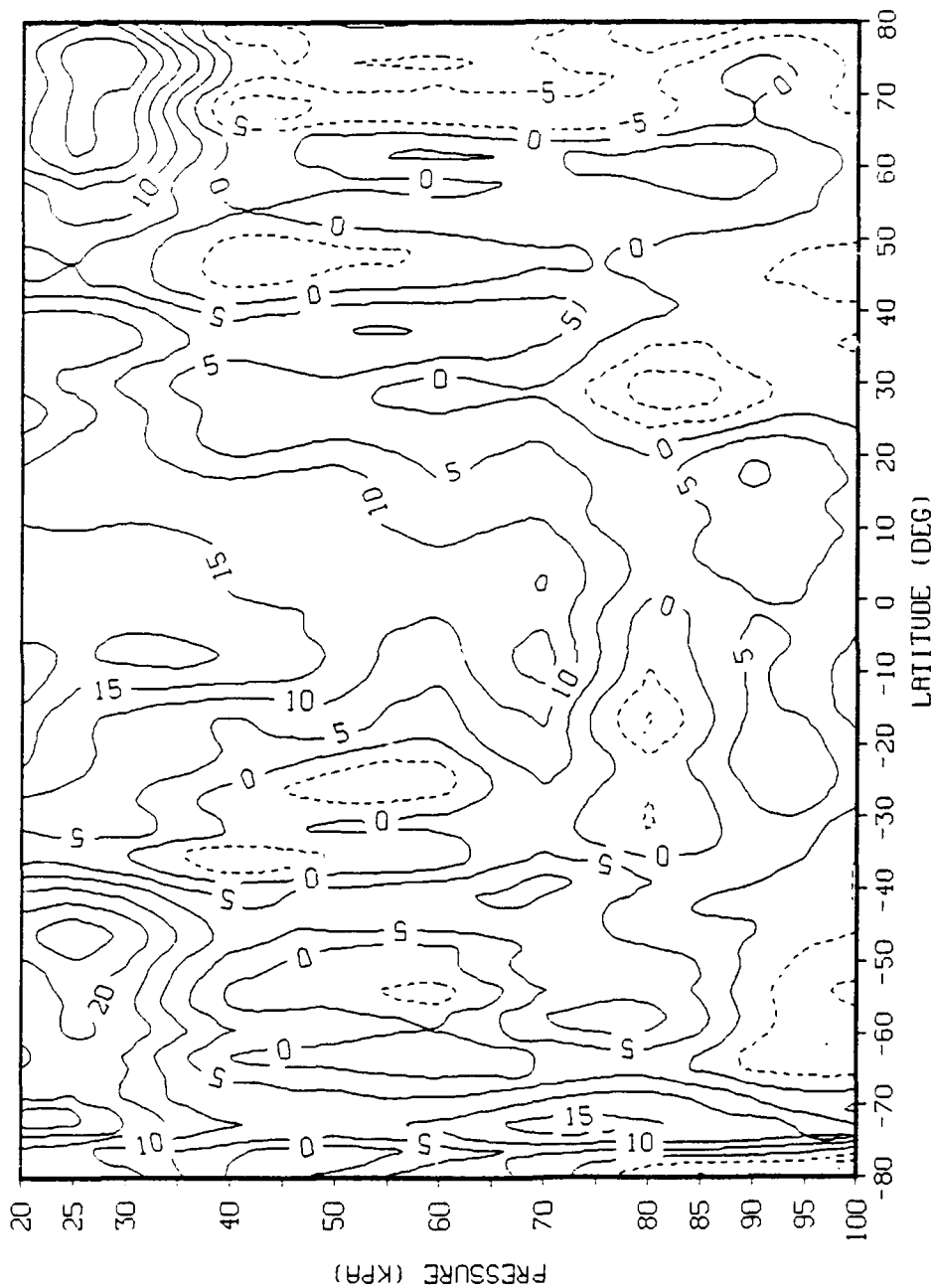


Figure 17. Forecast Day 5 Zonally-Averaged Relative Humidity Bias (percent) of GSM 34 Experiment 4 (GL Evap) Initialized 1200 UTC 11 June 1979 When Evaluated Against FGGE III-B Analysis.

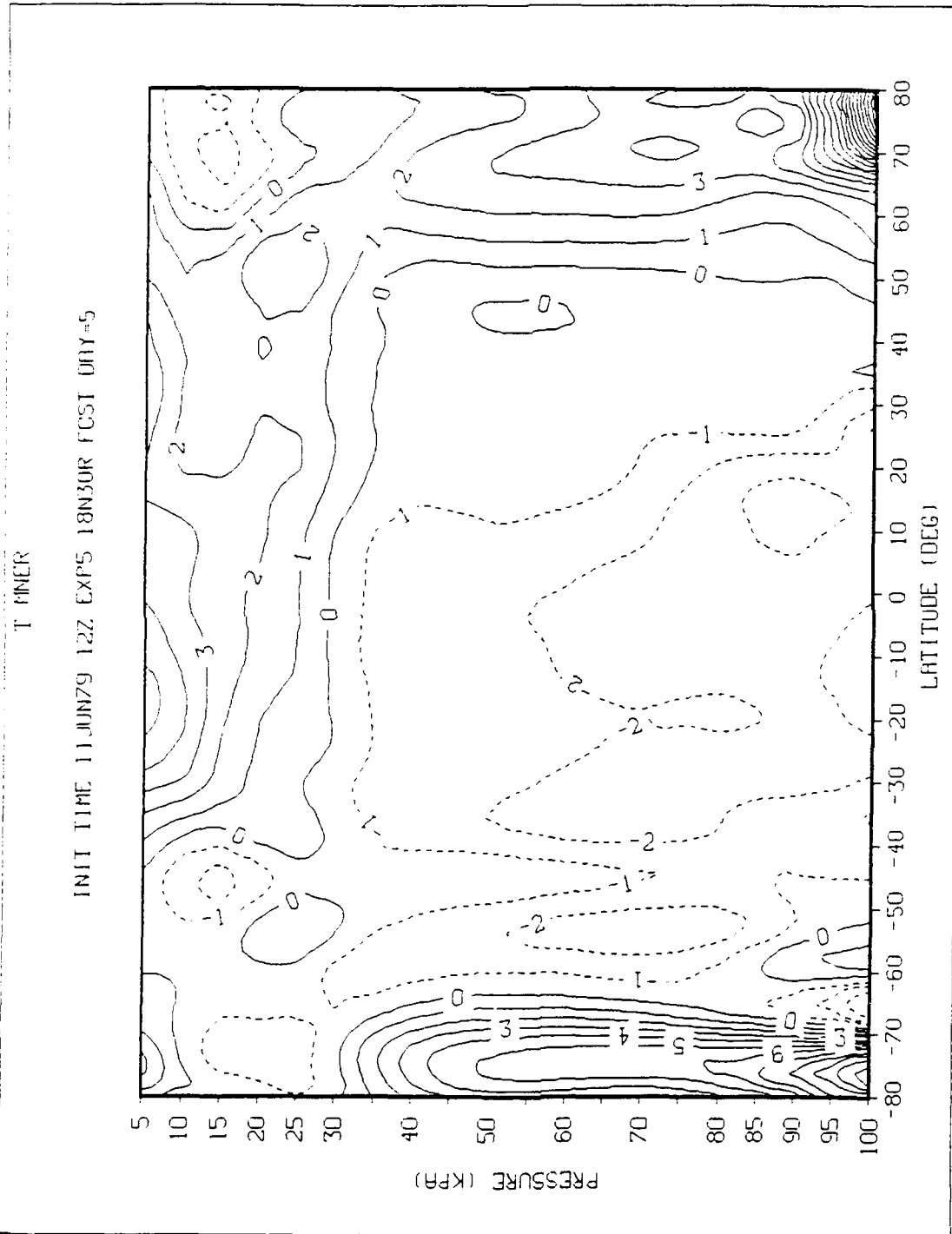


Figure 18. Forecast Day 5 Zonally-Averaged Temperature Bias (K) of GSM Experiment 5 (NMC Evap) Initialized 1200 UTC 11 June 1979 When Evaluated Against FGGE III-B Analysis.

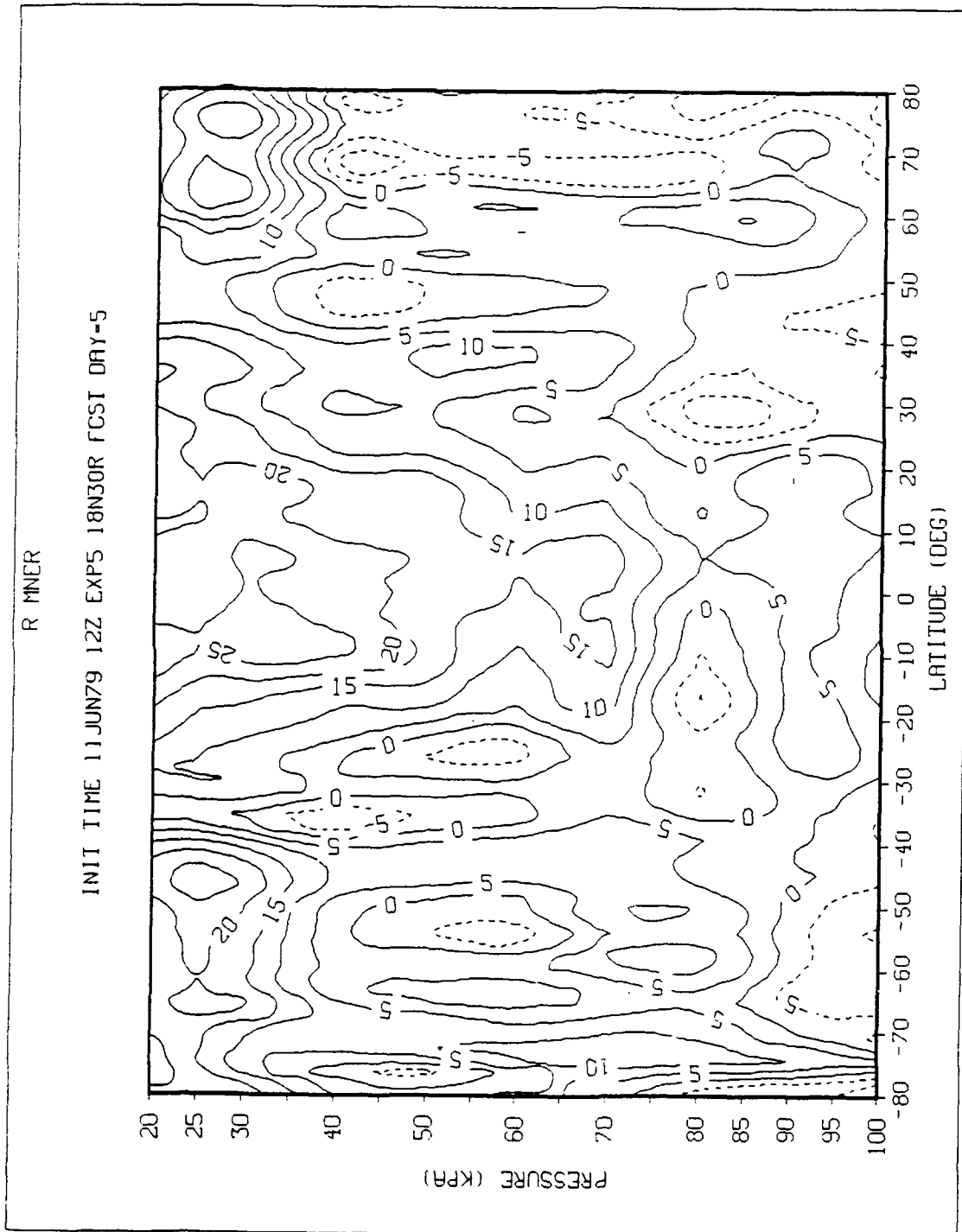


Figure 19. Forecast Day 5 Zonally-Averaged Relative Humidity Bias (percent) of GSM 36 Experiment 5 (NMC Evap) Initialized 1200 UTC 11 June 1979 When Evaluated Against FGGE-III-B Analysis.

bias in RH evident in Figures 17 and 19. Negative biases greater than 25 percent in experiment 3 have been replaced by positive biases of 15 percent in experiment 4 and 20 percent in experiment 5 in the tropical mid-troposphere.

Sundquist¹⁹ drew our attention to yet another possible shortcoming in the formulation. The baseline code computes the moisture change Δq for the moisture supply from the difference between the preliminary (that is, before convective adjustment) forecast value of specific humidity q^{n+1} and the present timestep value q^n . This amounts to forward differencing, which has the possibility of being numerically unstable. He suggested that instead we compute moisture change at the present timestep using the preliminary forecast value and the previous timestep value of specific humidity [that is, $(q^{n+1}-q^{n-1})$]. This is the centered-difference (or "leapfrog") approximation to the moisture change, and can be computed at all timesteps except the first one, where a forward difference is computed.

We observed several indications of greater stability in MODKUO when the leapfrog moisture change computation was implemented. We found that the time series of convective precipitation at a typical grid point was much smoother than it was before implementation (see Figure 9 for a pre-implementation example). This suggests some reduction of instability resulted from the leapfrog scheme. Also, excessive rates (also seen for example in Figure 9) were reduced, and sudden drops and rises in rates changed to more gradual changes. Overall, the more stable performance of MODKUO was deemed to be an improvement.

Since the moisture change over two timesteps is now to be used as the source for cumulus heating and moistening, the form of moisture adjustment equation should be $q_A^{n+1} = q^{n-1} + \alpha_c (q_c^{n+1} - q^{n+1})$. Here q_A^{n+1} is the cumulus adjusted forecast specific humidity, and α_c the adjustment parameter computed in the KUO formulation. Thus, it is now the previous (q^{n-1}) rather than the present (q^n) time level of specific humidity that is the basis for cumulus adjustment. Finally, we use half of the cumulus heating

¹⁹Sundquist, H.. (1988) Personal Communication

portion of the moisture change over two timesteps in the vertical integration to compute precipitation corresponding to a single timestep.

In the KUO convection scheme, the moisture converged (here, $q^{n+1} - q^{n-1}$) in the grid box from large-scale moisture advection and surface evaporation forms the supply for cloud growth (1-b) and for moistening the environment (b). The fraction b of this supply moistens the large-scale environment (modify q^{n-1} to form q_A^{n+1}), but in strong moist convection, b is small so the bulk of the moisture supply goes to cumulus heating of the large-scale atmosphere through cloud formation (latent heat release). In other words, the final adjusted value q_A^{n+1} is less than the preliminary forecast value q^{n+1} because most of the converged water that led to q^{n+1} went to cumulus heating rather than moistening of the large-scale environment. The difference between the cloud moistening component $\alpha_c(q_c^{n+1} - q^{n+1})$ and the moisture converged $q^{n+1} - q^{n-1}$ is referred to as the cloud drying effect. This difference can be shown to be equivalent to $q_A^{n+1} - q^{n+1}$ and will always be negative for $b > 0$.

The leapfrog moisture differencing scheme was employed using both experiment 4 (GL EVAP) and experiments 5 (NMC EVAP) as base versions of MODKUO. The resulting experiments are designated experiment 8 (NMC EVAP + LPFRG) and experiment 9 (GL EVAP + LPFRG). The globally-averaged precipitation rates for the five-day forecasts are shown in Figure 15. Both experiment 8 and experiment 9 produced precipitation rates of about 3 mm/day that remained steady through the forecast period. More damping of the diurnal signal is evident in these curves than in the experiment 4 and 5 curves.

Figures 20 and 21 show the zonal mean five-day forecast errors for temperature and RH in experiment 8 (NMC EVAP + LPFRG). Figures 22 and 23 depict the same zonal mean errors for experiment 9 (GL EVAP + LPFRG). As in experiments 4 and 5, cold biases dominate in the lower and middle tropical troposphere. A small region of cold bias greater than 3 K exists in the experiment 8 plot, but is absent from the plot of experiment 9. There is some suggestion of slight warm bias in both experiment 8 and 9 plots, more extensive in the latter, in the summer mid-latitudes at 85 kPa. The upper troposphere warm biases in experiments 8 and 9 are largely

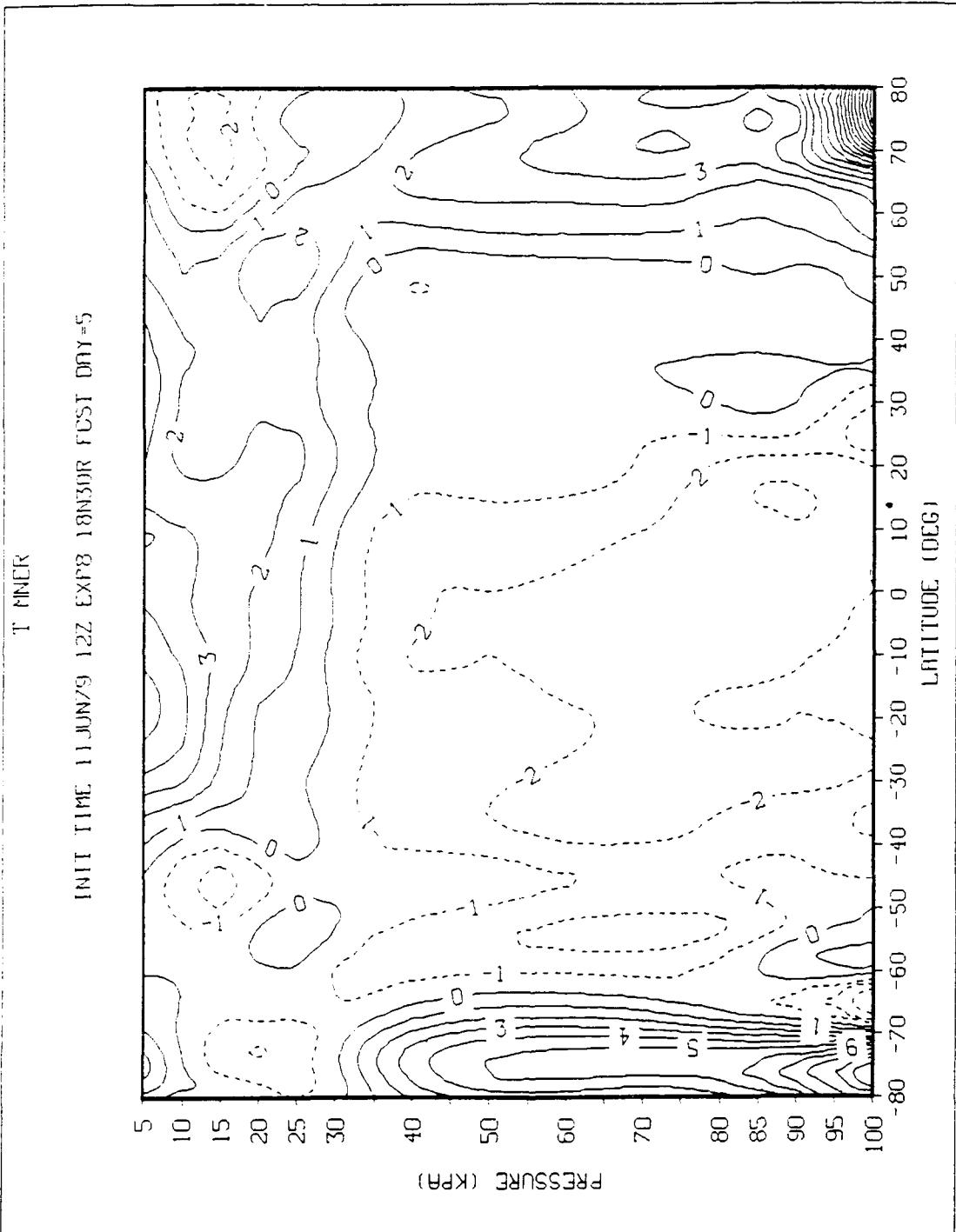


Figure 20. Forecast Day 5 Zonally-Averaged Temperature Bias (K) of GSM Experiment 8 (NMC Evap & Lpfrg) Initialized 1200 UTC 11 June 1979 When Evaluated Against FGGE III-B Analysis.

R 11NER

INIT TIME 11JUN79 12Z EXP8 18N30R FCST DAY=5

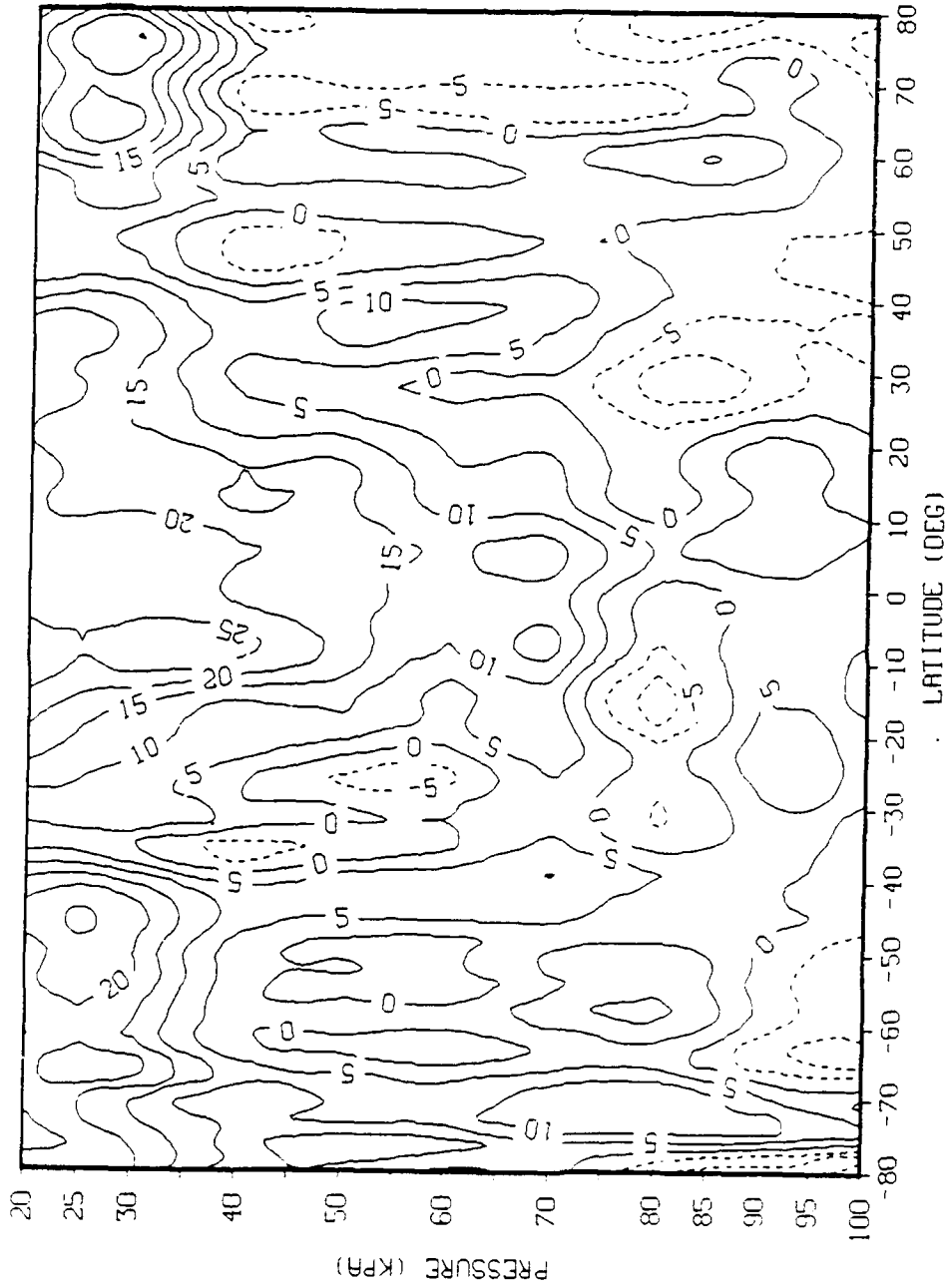


Figure 21. Forecast Day 5 Zonally-Averaged Relative Humidity Bias (percent) of GSM Experiment 8 (NMC Evap & Lpfrg) Initialized 1200 UTC 11 June 1979 When Evaluated Against FGGE III-B Analysis.

T MINER

INIT TIME 11JUN79 12Z EXP9 18N30R FCSI DAY-5

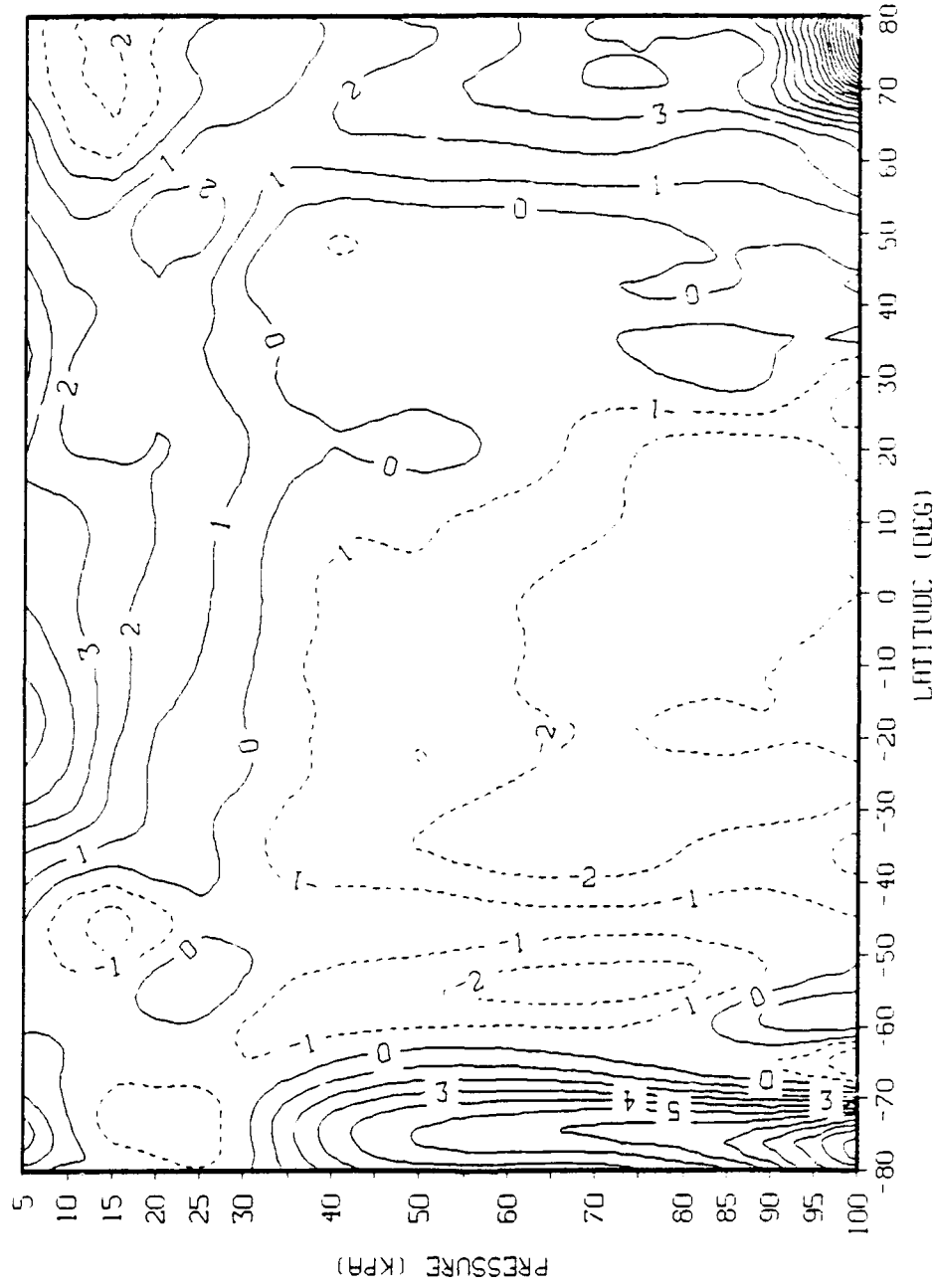


Figure 22. Forecast Day 5 Zonally-Averaged Temperature Bias (K) of GSM Experiment 9 (GL Evap & Lpfrg) Initialized 1200 UTC 11 June 1979 When Evaluated Against FGGE III-B Analysis.

P. MIER

INIT TIME 11 JUN 79 12Z EXPD 18NSUR F0ST 00Y=5

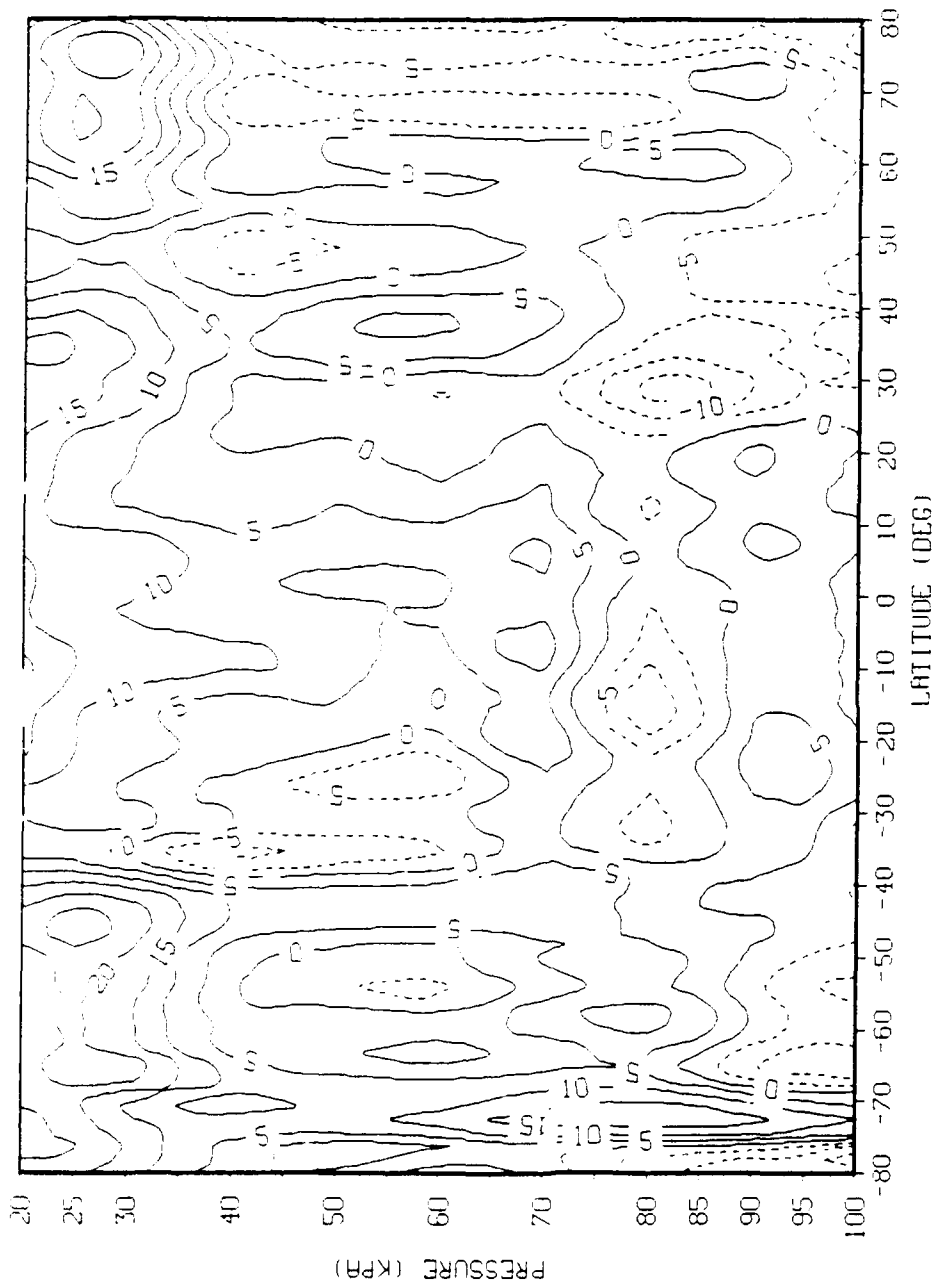


Figure 23. Forecast Day 5 Zonally-Averaged Relative Humidity Bias (percent) of GSM Experiment 9 (GL Evap & Lpfrg) Initialized 1200 UTC 11 June 1979 When Evaluated Against FGGE III-B Analysis.

unchanged from experiments 4 and 5. Positive RH biases in Figures 21 and 23 in the middle and upper tropical troposphere are now evident, with maxima of 25 percent and 10 percent respectively for experiments 8 and 9. Both NMC EVAP and GL EVAP have a tendency to over-moisten the upper troposphere in the tropics, but this tendency is reduced when using the leapfrog moisture differencing scheme.

3.4 Impact of Methodology Improvements-Summary

A scheme that parameterizes the evaporation of falling convective precipitation into unsaturated lower model layers was invoked in the GL Baseline MODKUU. This resulted in a reduction of globally-averaged precipitation rate from 6 to 4.25 mm/day. When this evaporation scheme was modified to allow evaporation only within the cumulus cloud-covered portion of the model grid box, the resulting global rate was 4.5 mm/day. In both versions of the model when the evaporation effect was included, the lower and mid-tropospheric tropical cold bias was increased from GL Baseline values. The negative bias was replaced by a positive bias in the mid-troposphere. These trends result from the large-scale cooling and moistening of the atmosphere associated with the evaporative phase change.

When a temporal center-difference (leapfrog) scheme replaced a forward-difference scheme of computing moisture convergence in the two versions of the model with evaporation effects, a further reduction of globally-averaged precipitation rate to 3 mm/day was realized. A diurnal signal in the globally-averaged rate that was clearly evident in the GL Baseline version of MODKUU was not present in either of these upgraded model results. The addition of the leapfrog scheme increased the mid-tropospheric cold bias of the full grid box evaporation version of the model but resulted in a decrease of the low level cold bias of the partial grid box evaporation model version. The leapfrog scheme reduced the middle and upper tropospheric positive RH bias down to maxima of 25 percent and 10 percent, respectively, for the full and partial evaporation schemes. The combination of the partial evaporation

scheme and the leapfrog moisture differencing led to a smaller tropical cold bias and positive RH bias than the full evaporation and leapfrog combination.

Figure 24 is a plot of the zonally-averaged precipitation accumulated over forecast days 2-4 (1200 UTC 12 June - 1200 UTC 15 June). The accumulated precipitations for each of the forecasts have been multiplied by 10 to give an estimate of the 30-day accumulation. This was done to compare the forecast results with the climatological values of Jaeger²⁰ for the month of June. The curve referred to as GWCGSM is the GWC84 model referenced earlier in the report. All of the curves display maxima near the equator in the summer hemisphere tropics. This region of most active convection corresponds to the intertropical convergence zone. The four GL versions of the model generate precipitation in varying degrees of excess over climatology at the latitude of maximum precipitation. The figure shows the effect of the leapfrog and the different evaporation formulations on precipitation as a function of latitude. The leapfrog scheme has a significant reducing effect at all three maxima in the summer hemisphere (all of which are presumed to be significant convection zones). By contrast, no effect is seen in the winter hemisphere maxima in mid-latitudes (which are thought to be primarily stable precipitation). The effect of the partial grid box evaporation scheme is greatest in the tropical maximum zone, and comparatively small elsewhere.

Experiment 9 combined the benefits of a desirable globally-averaged precipitation rate with the smallest zonal mean temperature and RH errors in the tropics better than the other alternatives considered. It was selected, therefore, as the version we subjected to further evaluation (discussed below).

²⁰Jaeger, L. (1983) Monthly and areal patterns of mean global precipitation, in *Variations in the Global Water Budget*, A. Street-Perrott, M. Beran, R. Ratcliffe, Eds., D. Reidel, Dordrecht.

4. DETAILED DIAGNOSIS OF SELECTED VERSION OF MODKURO

In an attempt to quantify local characteristics of its moist convection performance, we have sought to use climatological records and even conventional observations of precipitation as a standard against which the performance of the selected version of MODKURO could be measured.

The areal distribution of the three-day accumulations shown in Figure 24 is depicted for much of the Eastern Hemisphere for the GL Baseline (experiment 3) and experiment 9 in Figures 25 and 26 respectively. The purpose of showing both plots is to illustrate the spatial distribution of the reduction of precipitation caused by employing GL EVAP and the leapfrog differencing scheme. Notice that most of this precipitation reduction takes place over the Indian Ocean. The maxima over central Africa, southern India, and southeast Asia remain, but are reduced in magnitude. A maximum occurring over Europe in experiment 3 is reduced in experiment 9.

To see if these reductions represent improved precipitation forecasts, we compared the three-day accumulations with conventional precipitation measurements where available. We performed these comparisons over three regions: representative of tropical ocean areas (Indonesia and Philippines), tropical land areas (western Africa), and extratropical land areas (western Europe). All 24-hour accumulated precipitation observations in the FGGE II-C data set within the three-day period were averaged for each GSM grid box following the procedure of Molteni and Tibaldi²¹. The average 24-hour accumulation for each grid box was then multiplied by 3 to represent the 3-day accumulated precipitation. The resulting values and the number of observations averaged within each grid box, are shown with their corresponding forecast values from experiments 3 and 9 in Figures 27, 28, and 29. In the tropical ocean region (Figure 27), experiment 9 has reduced precipitation amounts compared to experiment 3 in most of the grid boxes. However, both forecasts produced

²¹Molteni, F., and Tibaldi, S. (1985) *Climatology and Systematic Error of Rainfall Forecasts at ECMWF*, Tech. Rep. No. 51, European Centre for Medium Range Weather Forecasts, Shinfield Park, Reading, Berkshire RG2 9AX, England.

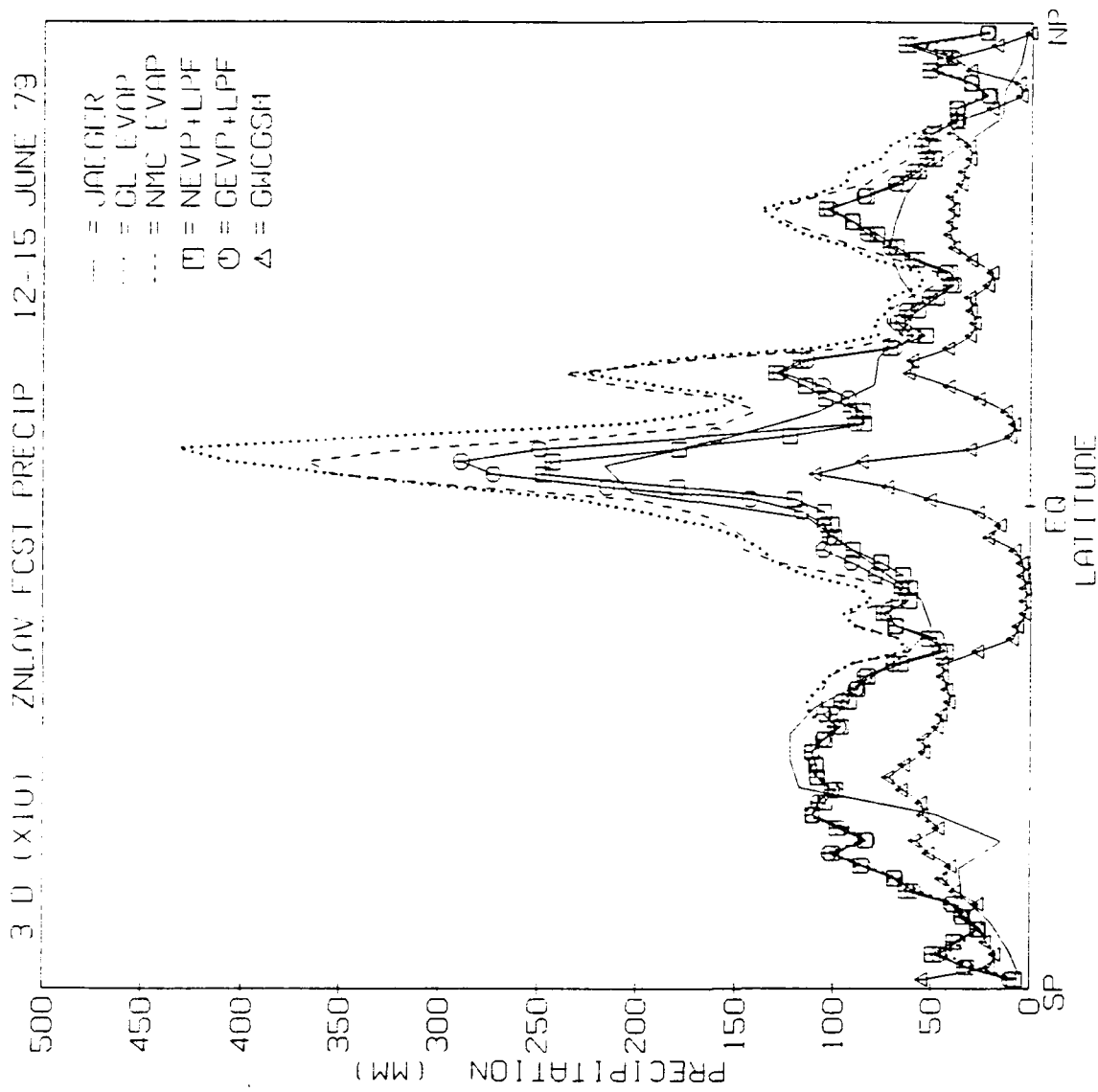


Figure 24. Zonally-Averaged Total Precipitation (mm) Accumulated Over Days 2-4 (X 10) for Five Versions of the GSM Initialized 1200 UTC 11 June 1979 as Compared with Jaeger²⁰ June Climatology Precipitation.

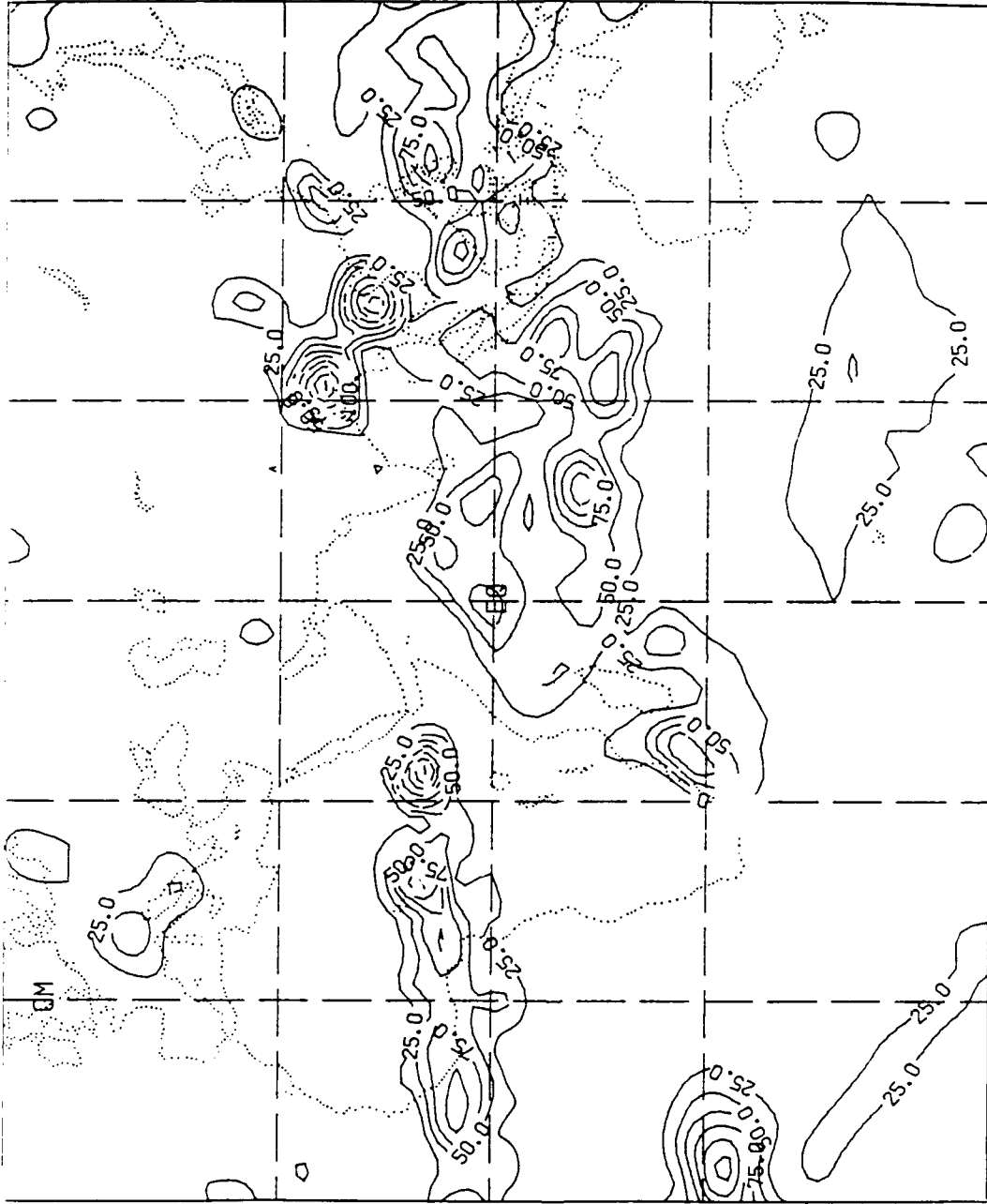


Figure 25. Map of 3-Day Total Precipitation Accumulation (mm) for 1200 UTC 12-15 June 1979 of GSM Experiment 3 (GL Baseline) Initialized 1200 UTC 11 June 1979.

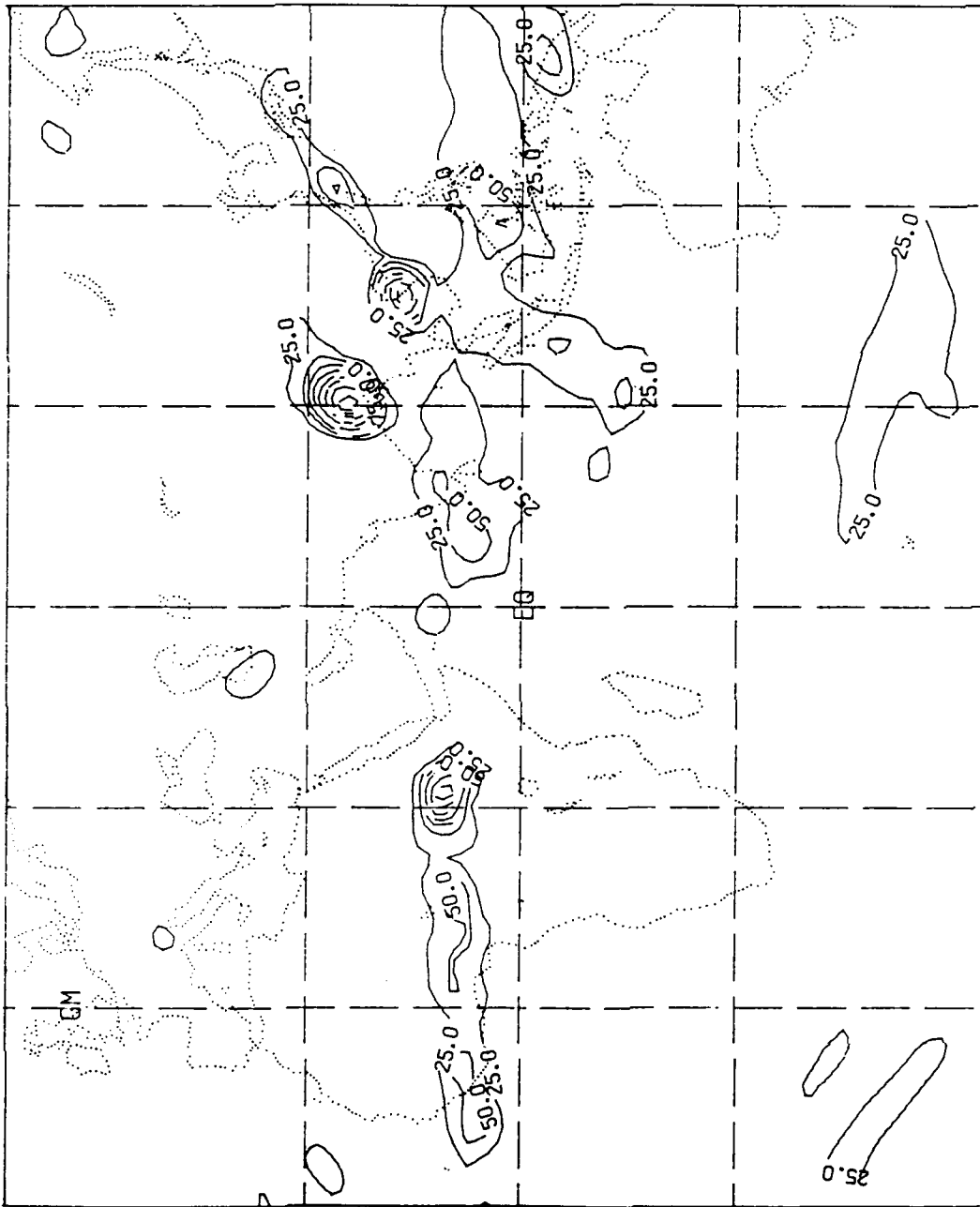


Figure 26. Map of 3-Day Total Precipitation Accumulation (mm) for 1200 UTC 12-15 June 1979 of GSM Experiment 9 (GL Evap & Lpfrg) Initialized 1200 UTC 11 June 1979.

precipitation accumulations that generally exceed the observed amounts. Both forecasts produce a local maximum over the Philippines. For the 10 grid boxes over or near the Philippines that have 25 or more observations, the average grid box values for observations, experiment 3, and experiment 9 are 26, 79, and 30 mm respectively. The better average agreement between experiment 9 and observations is partially explained by too little precipitation predicted in the four northernmost grid points (northern Philippines). However, at the four grid points where experiment 3 predicts over 100 mm, the average is reduced from 124 mm to 46 mm compared to 27 mm observed. Clearly, experiment 9 has reduced the average local maximum which was over 4.5 times too large in experiment 3.

We see a similar tendency in experiment 9 to reduce the tendency, in experiment 3, to overforecast precipitation over the tropical land region (Figure 28). This is a case where only three grid boxes with 30 or more observations yielded observed amounts that exceeded 25 mm accumulation (the observed 32, 36, and 27 mm amounts in the western portion). However, both experiments result in predictions of 25 mm or more through most of this region of western Africa. The model is predicting heavy precipitation in a region where in fact only modest amounts occurred. Both experiments yield a local maximum at the nine grid points lying south and southwest of Lake Chad, but the averaged forecasted values represent a nearly 50 percent reduction for experiment 9 (89 mm for experiment 3, 47 mm for experiment 9).

Another positive result from the model is that the northerly gradient of precipitation toward the Sahara appears qualitatively to be realistic. Even so, the model produces substantial rainfall amounts in this region that are not substantiated by observations. It is not clear from a single experiment if this is a regional pattern for the model or a quirk in a single episode.

Finally, a comparison of precipitation accumulations for the 3 days over western Europe (Figure 29) indicates yet another area of appropriate reduction for experiment 9. The observation amounts reveal two areas of precipitation amounts over 25 mm: the two grid points in northern Italy and several grid points over northwestern

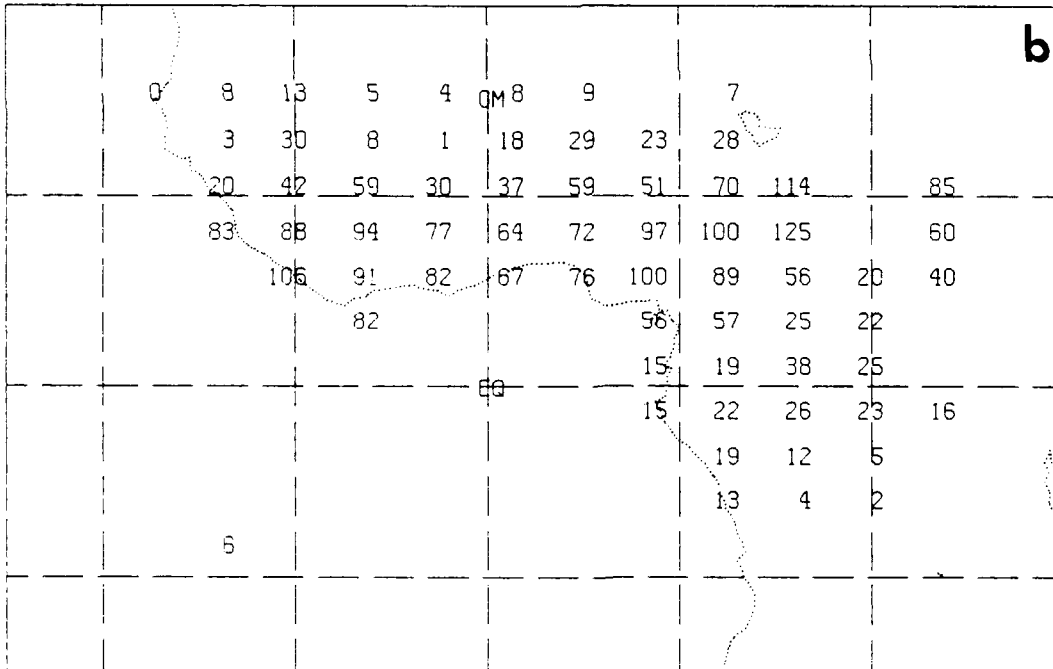
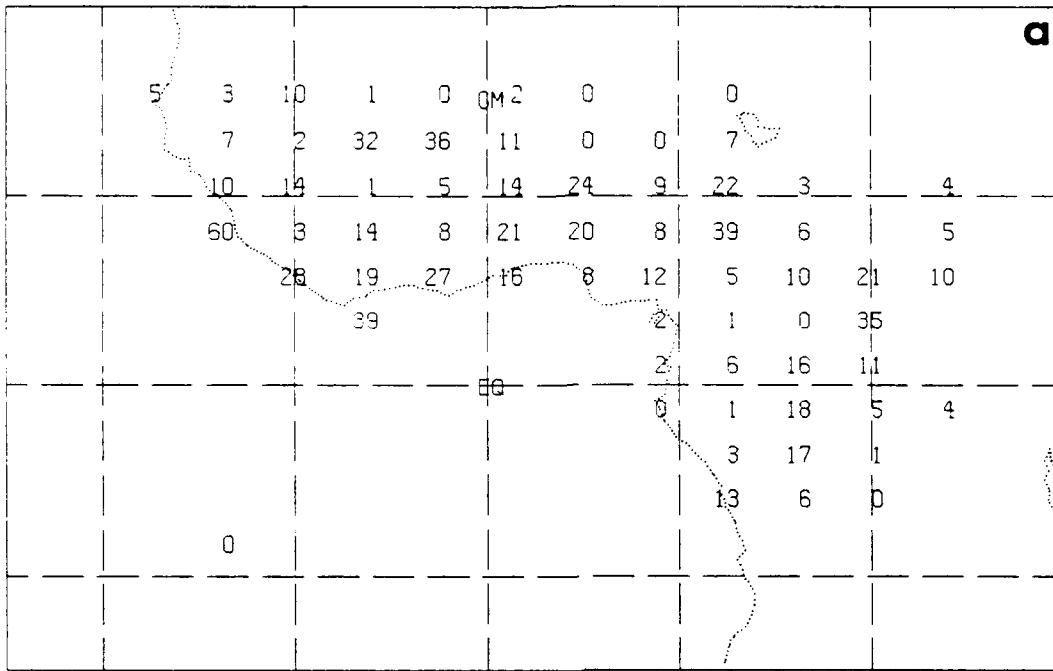


Figure 28. GSM Grid Box 3-Day Precipitation (mm) for 1200 UTC 12-15 June 1979 Over the Tropical Land Area: (a) Observed, (b) GSM Exp. 3, (c) GSM Exp. 9, (d) Number of Observations in Grid Box Average.

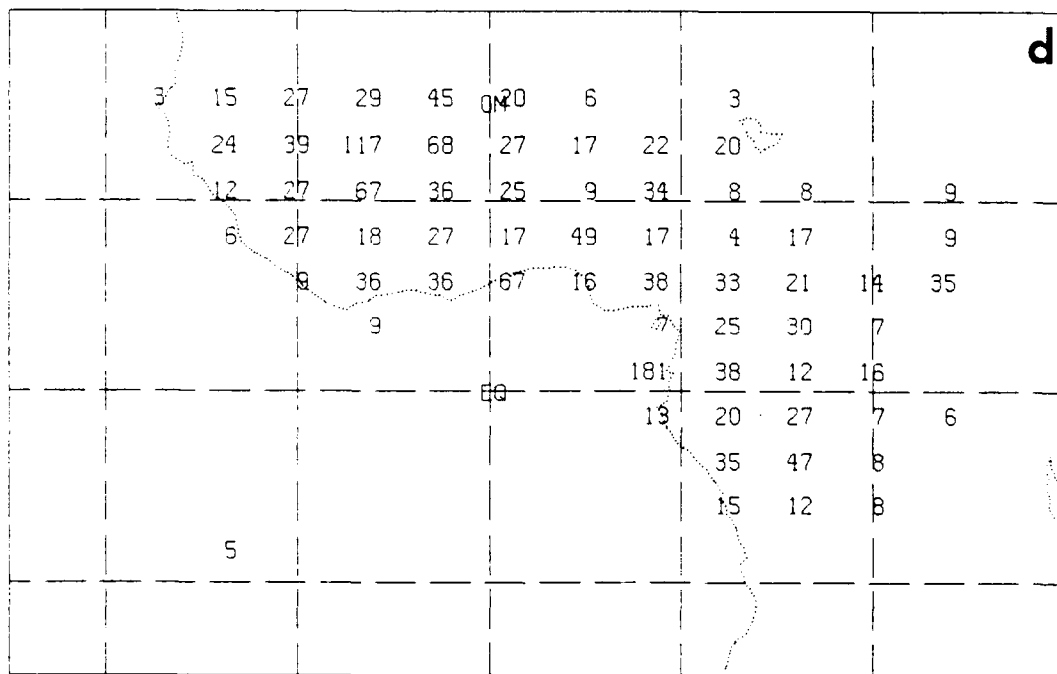
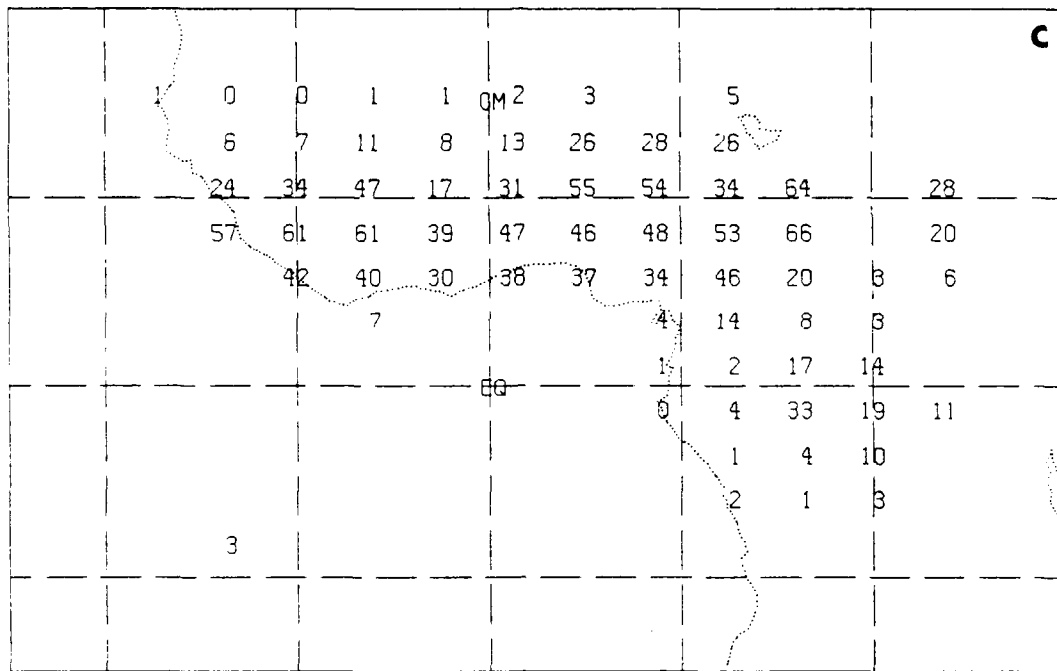


Figure 28. GSM Grid Box 3-Day Precipitation (mm) for 1200 UTC 12-15 June 1979 Over the Tropical Land Area: (a) Observed, (b) GSM Exp. 3, (c) GSM Exp. 9, (d) Number of Observations in Grid Box Average.

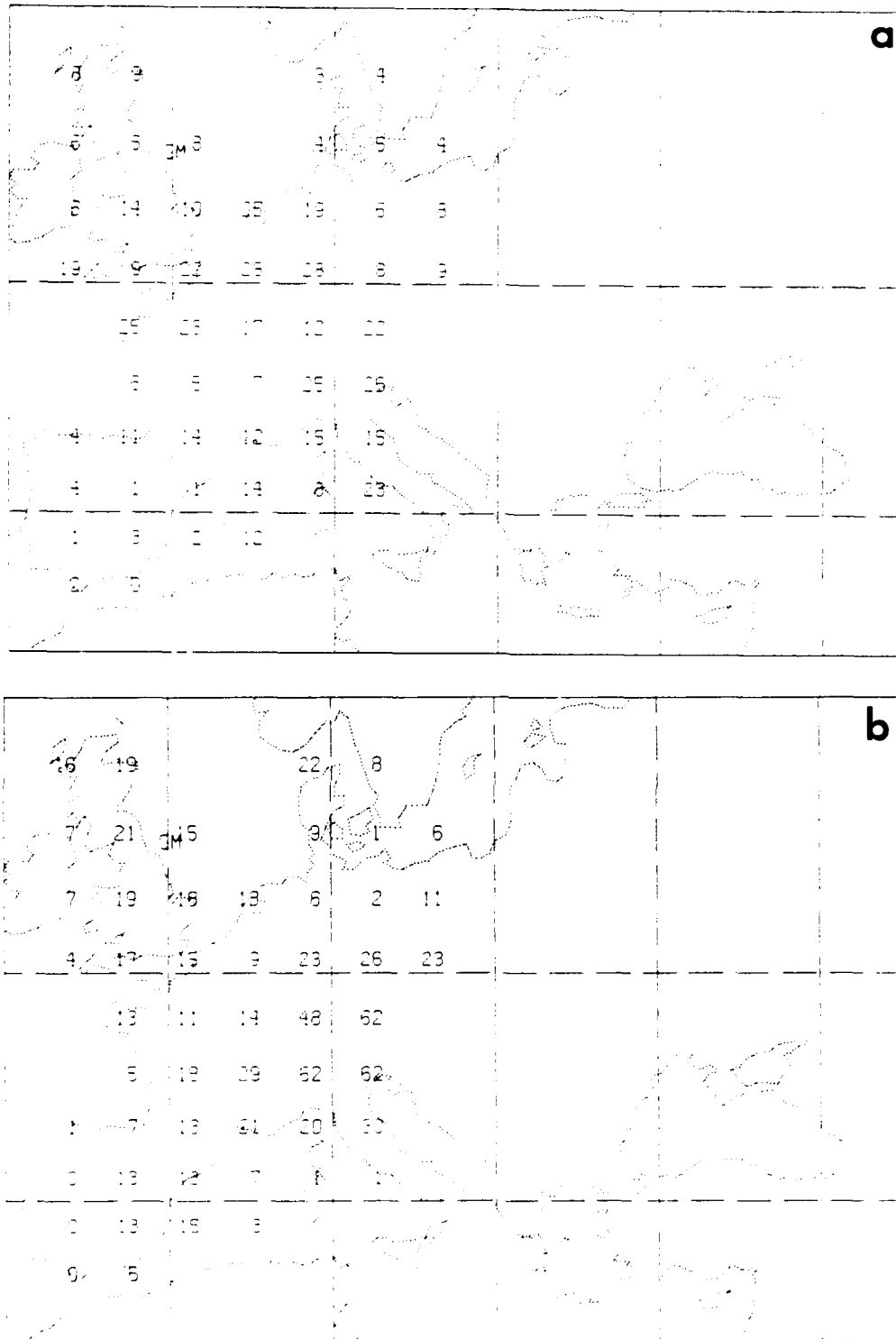


Figure 29. GSM Grid Box 3-Day Precipitation (mm) for 1200 UTC 12-15 June 1979 Over the Extratropical Land Area: (a) Observed, (b) GSM Exp. 3, (c) GSM Exp. 9, (d) Number of Observations in Grid Box Average.

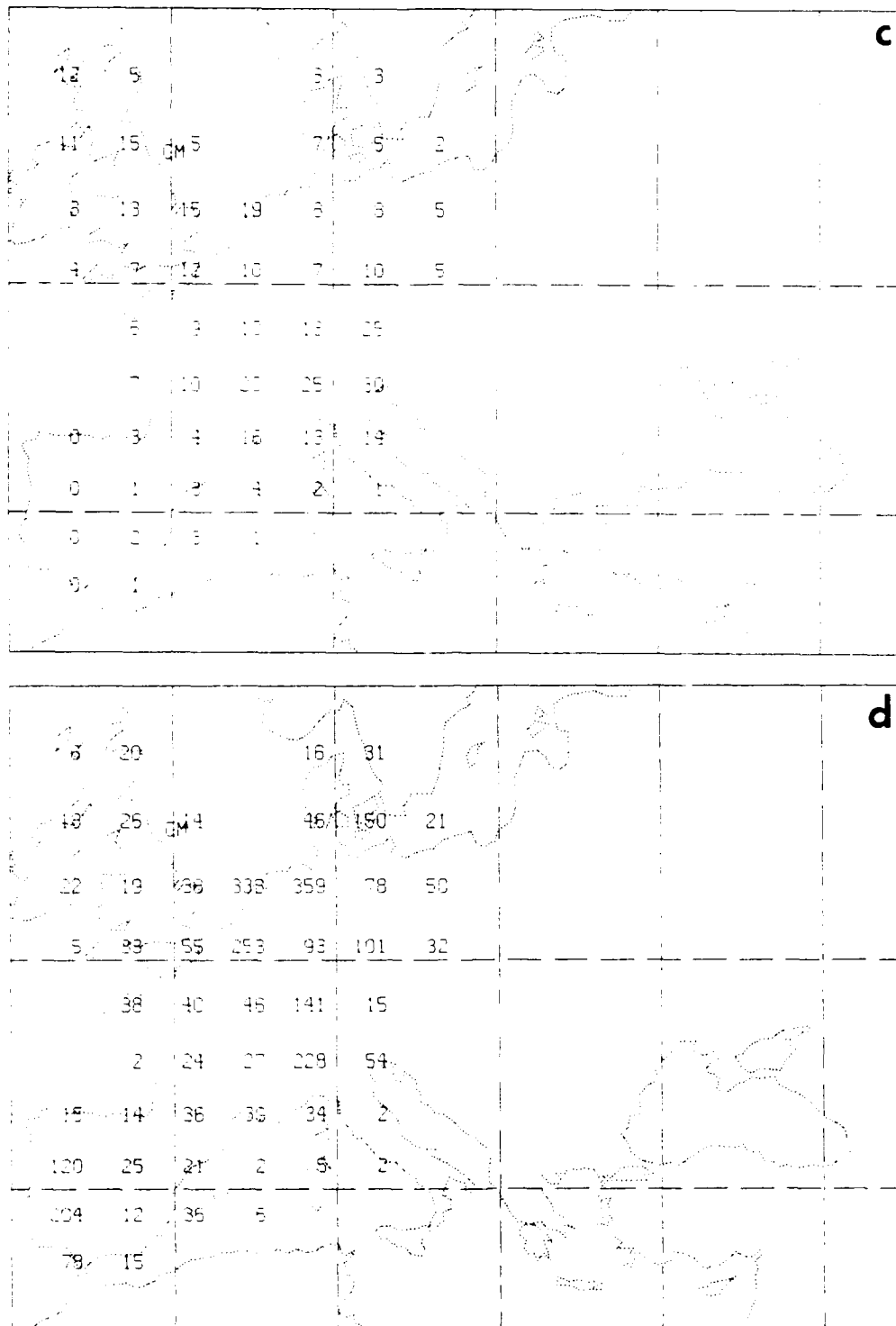


Figure 29. GSM Grid Box 3-Day Precipitation (mm) for 1200 UTC 12-15 June 1979 Over the Extratropical Land Area: (a) Observed, (b) GSM Exp. 3, (c) GSM Exp. 9, (d) Number of Observations in Grid Box Average.

continental Europe. The former maximum seems to be well placed by the models, especially in experiment 9. In fact, there is remarkable agreement between the six grid points centered on the two northern Italy points in their north-south direction. Experiment 3, by contrast, yields a 140 percent increase over experiment 9 in the average over these six points. However, neither experimental result detects the northwestern Europe maximum. Molteni and Tibaldi²¹ documented a tendency of the ECMWF model to produce too much precipitation over areas of steep topography in the model, and too little over smooth topography. Though consistent with the ECMWF tendency, it cannot be known from a single experiment if local terrain could have similarly influenced the production of a local maximum over the Alps and insufficient precipitation over coastal lowlands in these experiments.

We have primarily relied upon precipitation, which represents the vertically-integrated heating rate, to diagnose the realism of the MODKURO convective scheme. To ascertain the realism of the model-produced vertical distribution of convective heating, we must compare profiles of this quantity with observations. Unfortunately, observations of the vertical distribution of cumulus heating are generally unavailable. Other researchers (for example, Reed and Recker²² and Miller and Vincent²³) have deduced observed cumulus heating rates from budget studies. This involves the use of analyses of conventional observations to solve for all of the terms except condensational effects in the classic heat and moisture budget equations and then compute the condensational term as a residual. This approach is prone to uncertainties and can lead to a range of results, as illustrated by Miller and Vincent.²³ However, while the absolute magnitude of heating rates varies with geographic location and study, there is fairly good agreement as to the location of the level of maximum heating for tropical convection. Therefore, the reference profile shown in Figure 30, taken from Reed and Recker,²² represents a nominal relative

²²Reed, R.J., and Recker, E.E. (1971) Structure and properties of synoptic-scale wave disturbances in the equatorial western Pacific, *J. Atmos. Sci.*, **28**:1117-1133.

²³Miller, B.L., and Vincent, D.G. (1987) Convective heating and precipitation estimates for the tropical South Pacific during FGGE, 10-18 January 1979, *J.R. Meteorol. Soc.*, **113**:189-212.

EXPERIMENT 9 CONVECTIVE HEATING RATES FOR 11-14 JUNE 79
 AVERAGE OVER ALL CONNECTIVELY ACTIVE POINTS IN 15°N-15°S

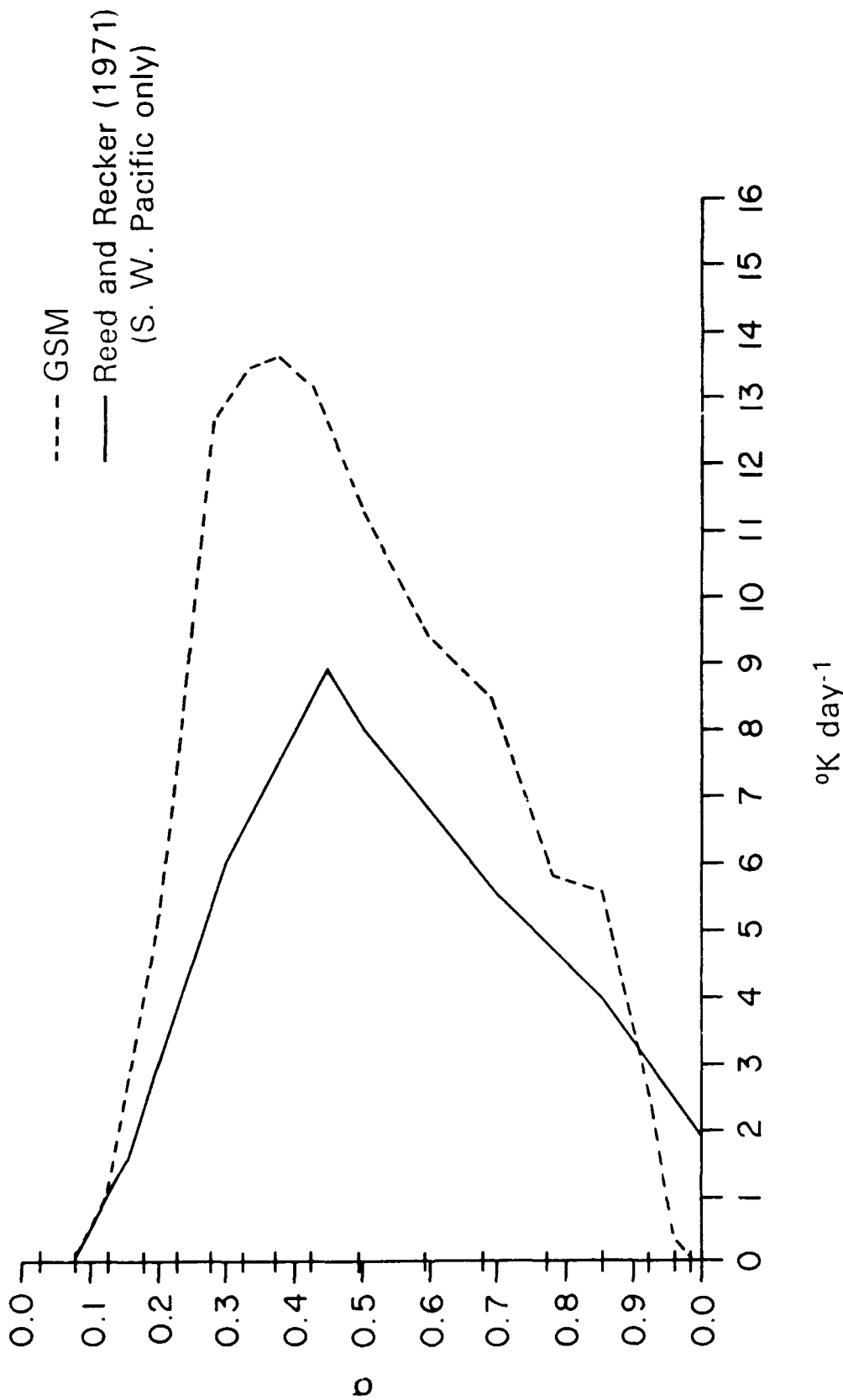


Figure 30. Vertical Profile of Convective Heating Rates (K day⁻¹) for 11-14 June 1979 Averaged Over All Convectively Active Points in +15° Latitude Band for GSM Experiment 9 as Compared with Southwestern Pacific Observed Profile from Reed and Recker²¹.

distribution of heating per day in the tropics. The other curve shown represents the cumulus heating rates diagnosed from experiment 9. The rates were averaged over all convectively active grid points at each hour over the period 1200 UTC 11 June to 1200 UTC 14 June 1979 in the zone between 15°N and 15°S. Note that the vertical axis is plotted in terms of the model vertical coordinate while the reference values were plotted on mandatory pressure levels. We assumed a nominal surface pressure of 100 kPa to plot the reference values in this figure. The overall vertical distribution of heating suggested by the two curves (including, in particular, the level of maximum heating) is similar.

We now focus on spatial and temporal distributions of some other parameters in the MODKUU parameterization known to be related to convection. Using hourly values of the model's large-scale quantities (temperature, specific humidity, surface pressure, and vertical velocity), we constructed all the MODKUU-produced quantities at each hour of forecast time through the first four days of the June forecast. The relevant quantities are convective available potential energy, moisture convergence, precipitation rate, convective heating fraction, cumulus cloud cover, cloud top temperature, and cloud top pressure. The following paragraphs discuss, qualitatively, the spatial and temporal trends seen in the experiment 9 version of MODKUU of these terms.

Moncrieff and Miller²⁴ have defined convective available potential energy (CAPE) as

$$CAPE \equiv \int_{z_0}^z g \delta \phi_p dz \quad (4)$$

where $\delta \phi_p$ is the natural logarithm of the potential temperature difference between the buoyant parcel and environment ($\theta_c - \theta$). According to Betts,²⁵ the net buoyancy

²⁴Moncrieff, M.W., and Miller, M.J. (1976) The dynamics and simulation of tropical cumulonimbus and squall lines, *Q.J.R. Meteorol. Soc.*, **102**:373-394.

²⁵Betts, A.K. (1982) Saturation point analysis of moist convective overturning, *J. Atmos. Sci.*, **39**:1484-1505.

of the parcel must take into account the liquid cloud water that forms as the parcel ascends above the LCL. If q_T represents the total water content of the parcel in vapor form at the LCL, then the liquid cloud water is $\lambda = q_T - q_s$, where q_s is the saturation specific humidity following the moist adiabat. Then the virtual potential temperature of the cloud parcel is expressed as $\theta_{vc} = \theta_s(1 + 0.61q_s - \lambda)$ where θ_s is the moist adiabat potential temperature. It is the difference between θ_{vc} and θ that determines the buoyancy of the parcel. Thus, $\delta\theta_p = \ln(\theta_{vc} - \theta)$. Introducing the hydrostatic equation, and expressing the integral as a discrete summation, CAPE can be computed in the form

$$CAPE \sim \sum_{k=KTOP}^{KBOT} R_d T_v(k) \{ \ln[\theta_{vc}(k) - \theta(k)] \} [\delta\sigma(k)/\sigma(k)] \quad (5)$$

where $T_v = T(1 + 0.61q)$ and R_d is the specific gas constant for dry air. The magnitude of CAPE will be influenced by the magnitude of conditional instability ($\theta_c - \theta$), the virtual temperature of the environment T_v , and by the specific humidity of the LCL, q_T .

Figure 31 shows the distribution of CAPE over the tropical ocean region for hours 24 and 48 of the forecast. A general north-south gradient is evident, with larger values of CAPE lying to the north. Notice that the value of CAPE in this region decreases during the 24-hour period between forecast hours 24 and 48.

The other independent factor in determining convective intensity in the Kuo formulation is moisture convergence. As we shall see, moisture convergence displays a definite diurnal signal over this region. For this reason, we have chosen to display plots of moisture convergence at its daily minimum time (0100-0400 local time) and its maximum time (1300-1600 local time) in Figure 32. In the Kuo formalism, precipitation rate and convective cloud cover are directly proportional to moisture convergence. Thus, we have displayed them in Figures 33 and 34 respectively to draw comparisons with the moisture convergence patterns. The important features in all three figures are the maxima northwest of Borneo and east of Celebes in the early morning, and the maxima over Borneo and Mindanao in the early afternoon.

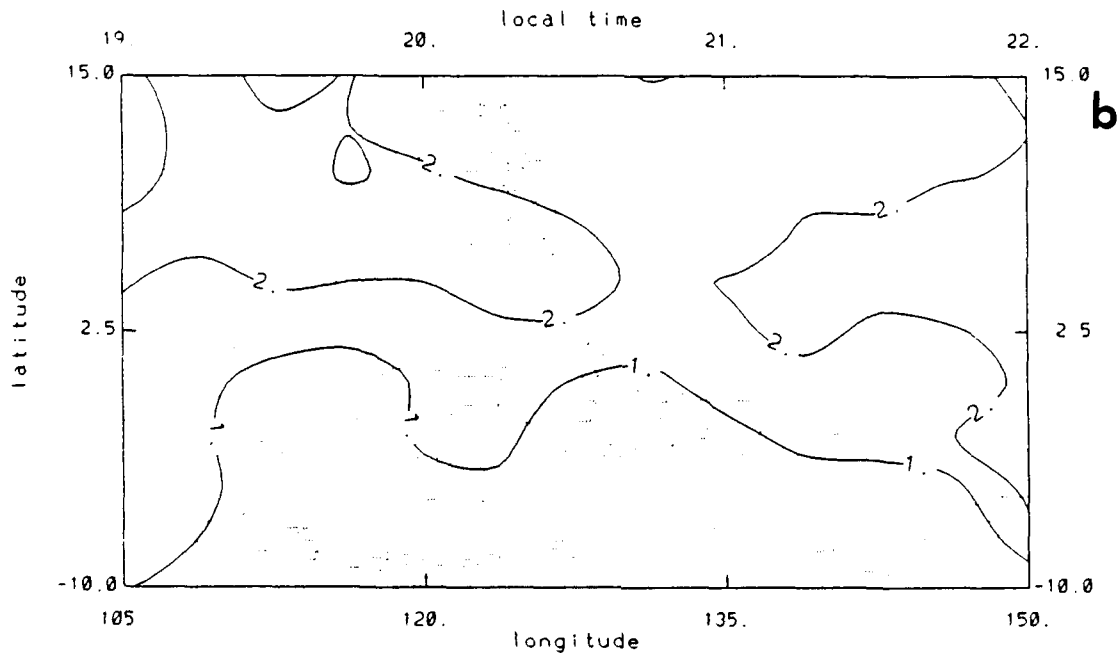
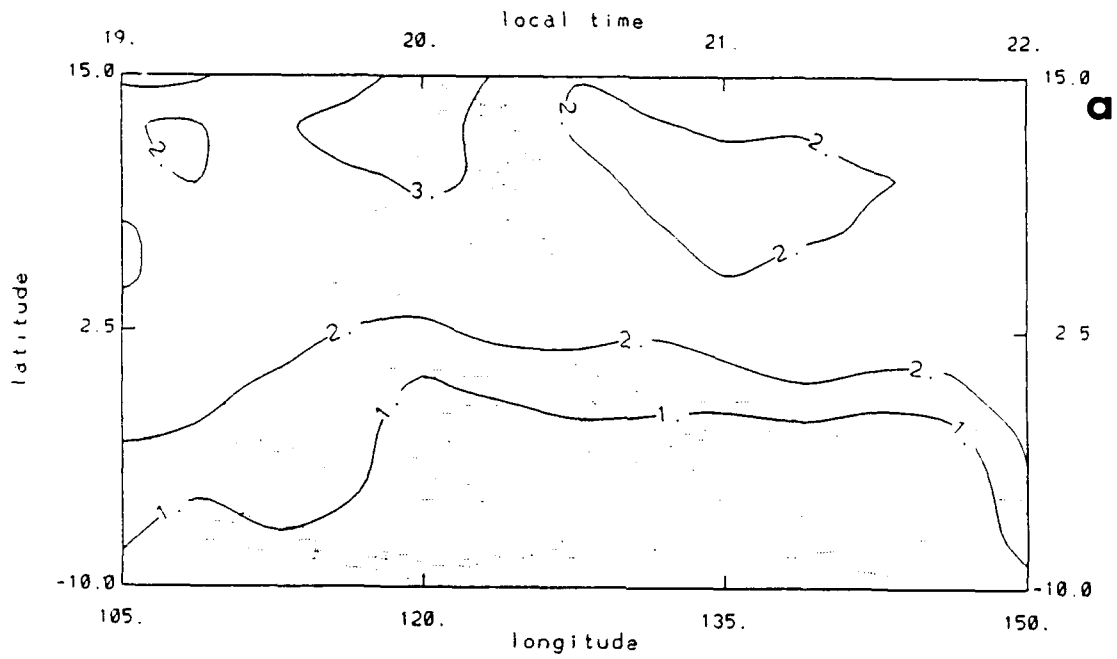


Figure 31. CAPE ($10^{-5} \text{ m}^2 \text{ s}^{-2}$) Over the Tropical Ocean Area for (a) 24h and (b) 48h Forecast Times From the 1200 UTC 11 June 1979 Experiment 9 Forecast.

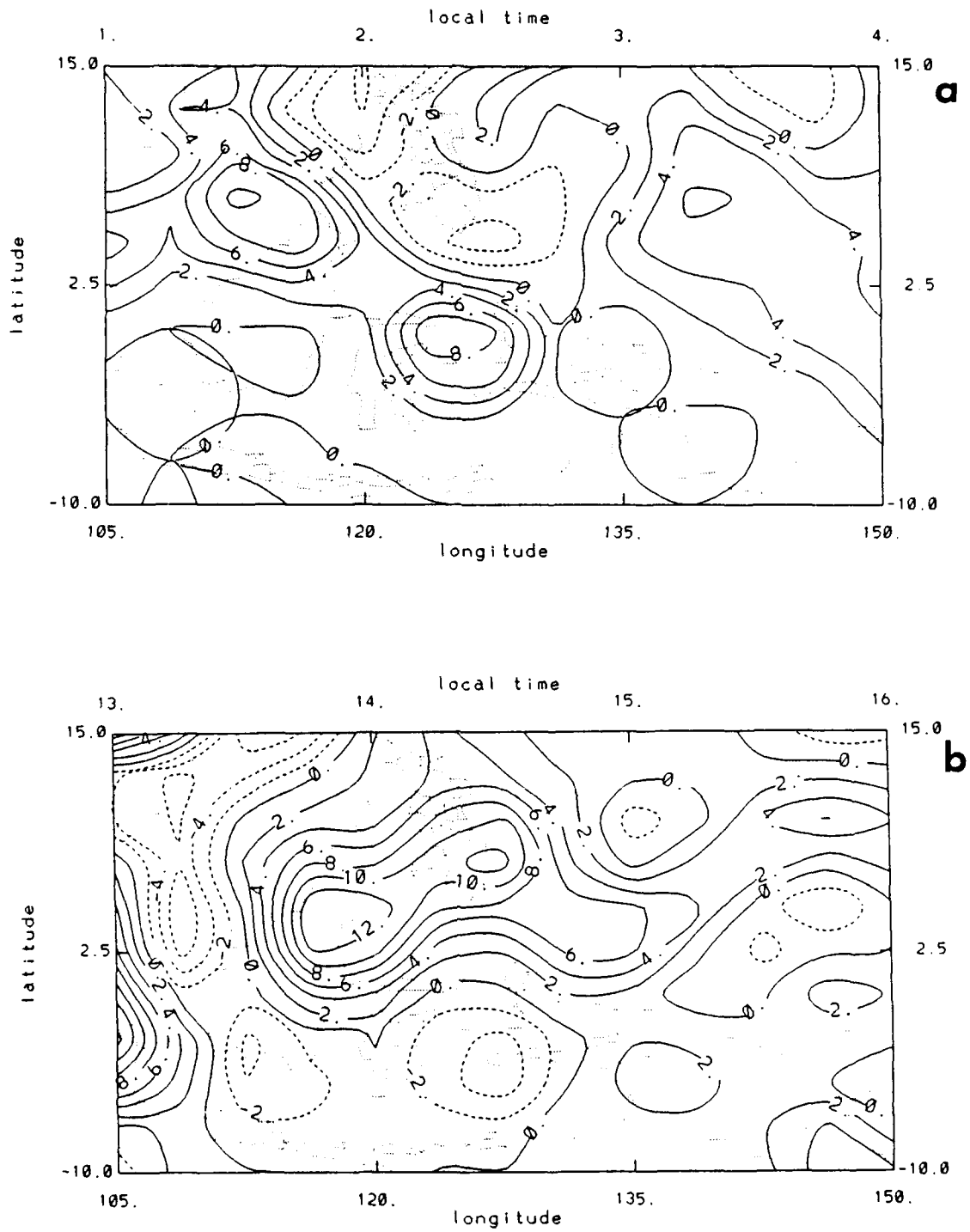


Figure 32. Moisture Convergence ($\text{g kg}^{-1} \text{ day}^{-1}$) Over the Tropical Ocean Area for (a) 30h and (b) 42h Forecast Times From the 1200 UTC 11 June 1979 Experiment 9 Forecast.

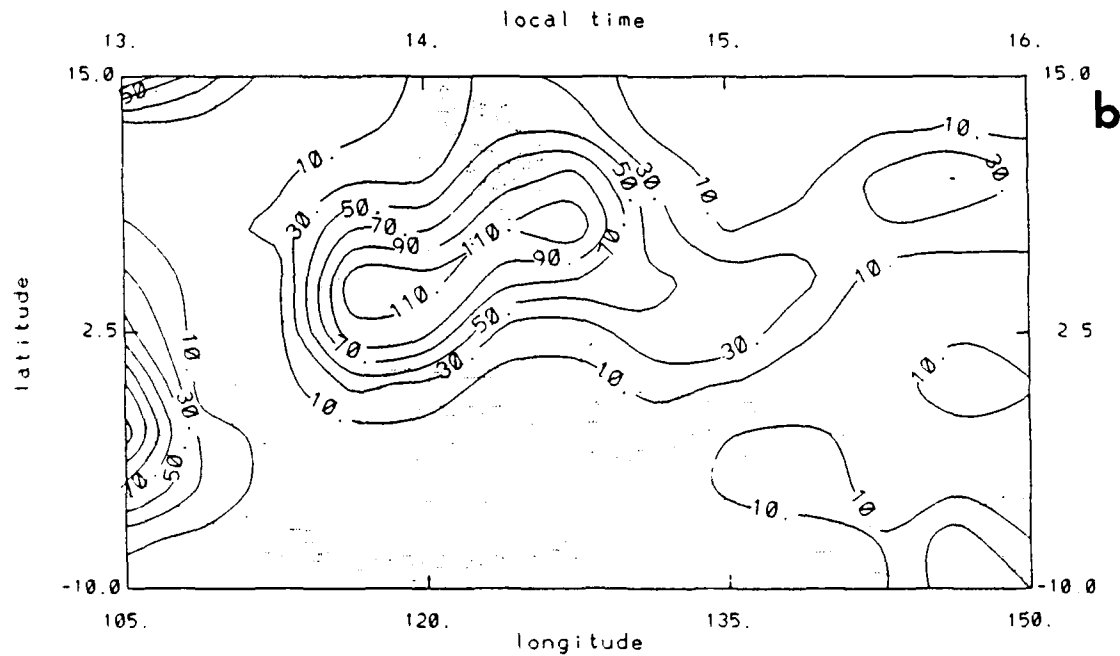
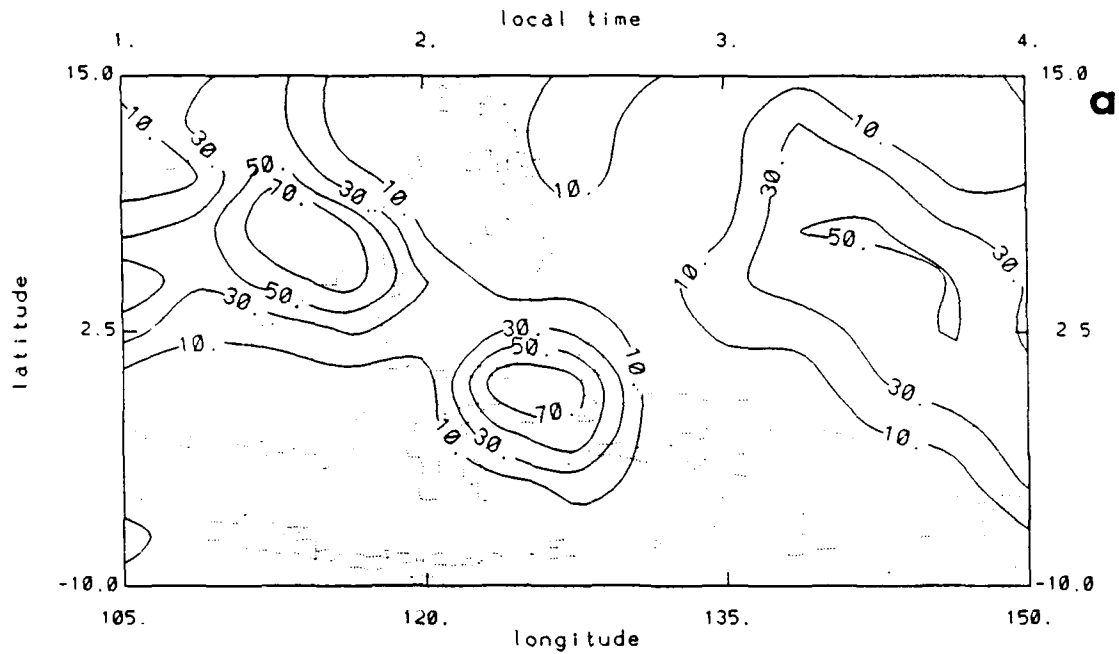


Figure 33. Precipitation Rate (mm day^{-1}) Over the Tropical Ocean Area for (a) 30h and (b) 42h Forecast Times From the 1200 UTC 11 June 1979 Experiment 9 Forecast.

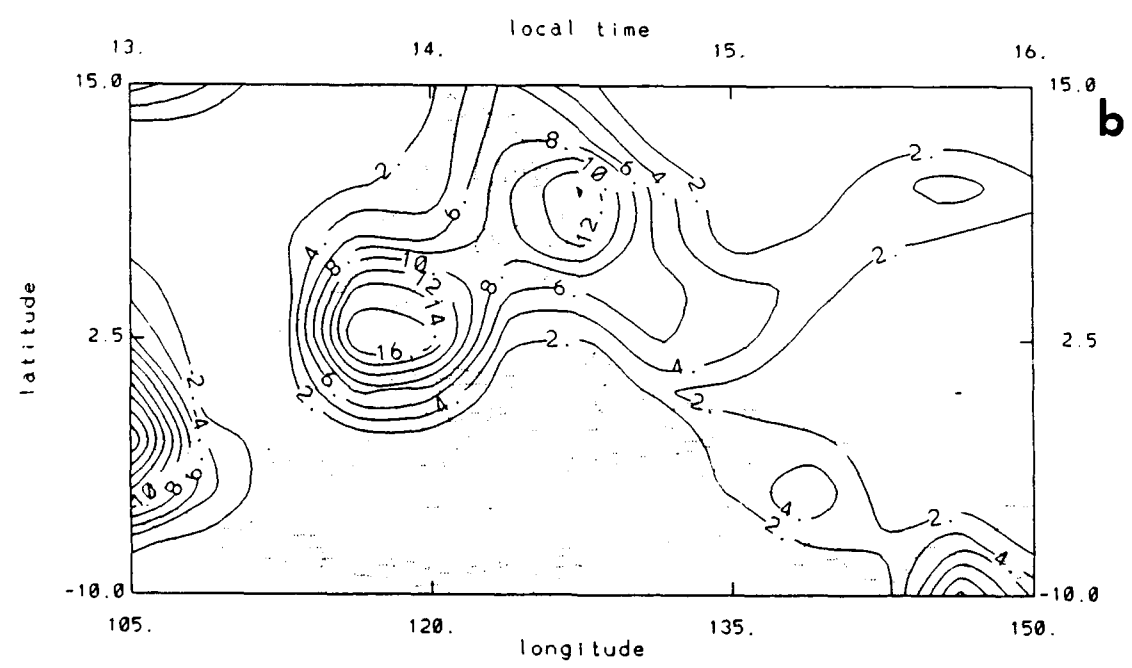
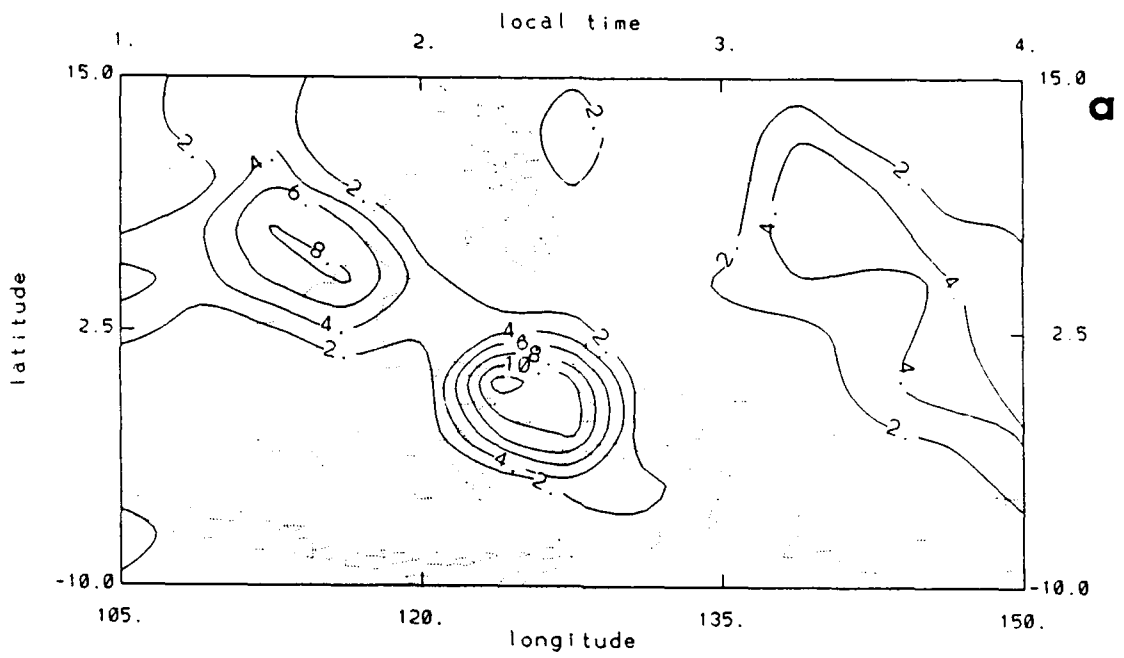


Figure 34. Convective Cloud Cover (percent) Over the Tropical Area for (a) 30h and (b) 42h Forecast Times From the 1200 UTC 11 June 1979 Experiment 9 Forecast.

The strong spatial correlations between moisture convergence, precipitation rate, and cloud cover are evident at both times. The area of intense precipitation in the early afternoon is characterized by indicators of deep convection, as can be seen in Figures 35 and 36. The cloud top isotherm of -70°C lies generally in the area of intense precipitation indicating that the cumulus tops associated with the convective precipitation are coldest. The fact that cloud tops in the eastern part of the region lie below (in altitude) the 12 kPa level (as seen in Figure 36) indicates that the upper troposphere is cooler over this area.

A subjective evaluation of an animated sequence of hourly fields of moisture convergence, precipitation rate, and cloud amount revealed diurnal variations. Through a careful study of the animated sequence, we noticed three characteristics of the precipitation anomalies. First, there was a tendency for large precipitation anomalies to form over land areas (especially Borneo and Mindanao) in the early afternoon. Second, we observed a tendency for heavy precipitation to form over ocean areas (in the South China Sea and the western Pacific Ocean) in the early daylight hours. Third, we observed very little coherent movement (advection) of the precipitation patterns; for the most part, they seem to remain stationary during their life span.

Figure 37 is a plot of CAPE, moisture convergence, and precipitation rate averaged over the tropical ocean domain (as depicted in the previous figures) for the first four days of the forecast. We computed the time mean of the area averages of each quantity and then plotted the departure from the time mean to focus on temporal trends. A clear diurnal signal is evident in all three quantities. Peaks at forecast times 18, 42, 66, and 90 correspond to the local time of 1400 over Borneo and Mindanao while minima at forecast times 6, 30, 54, and 78 translate to local times of 0200. A long term trend of the plotted quantities is also evident. Apart from the diurnal variations, CAPE decreases steadily over the four days while moisture convergence and precipitation rate increase over the same period. Both diurnal and long term trends for CAPE can be explained largely by Figure 38, which depicts the standard level temperature departures. It shows a clear diurnal pattern, with

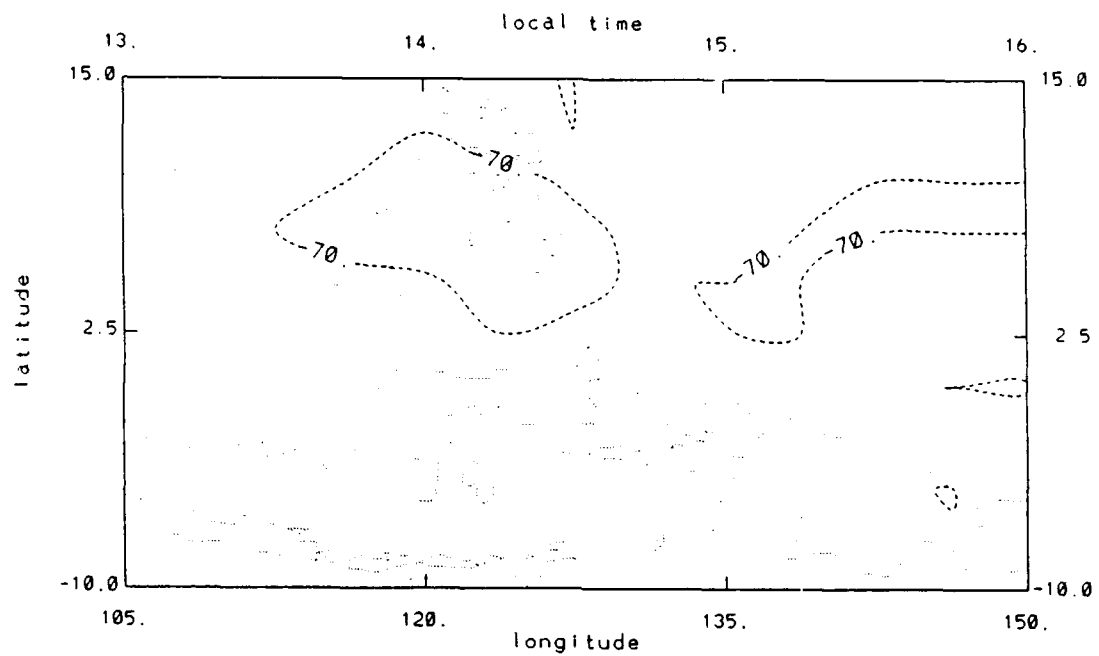


Figure 35. Cloud Top Temperature (C) Over the Tropical Ocean Area for the 42h Forecast Time From the 1200 UTC 11 June 1979 Experiment 9 Forecast.

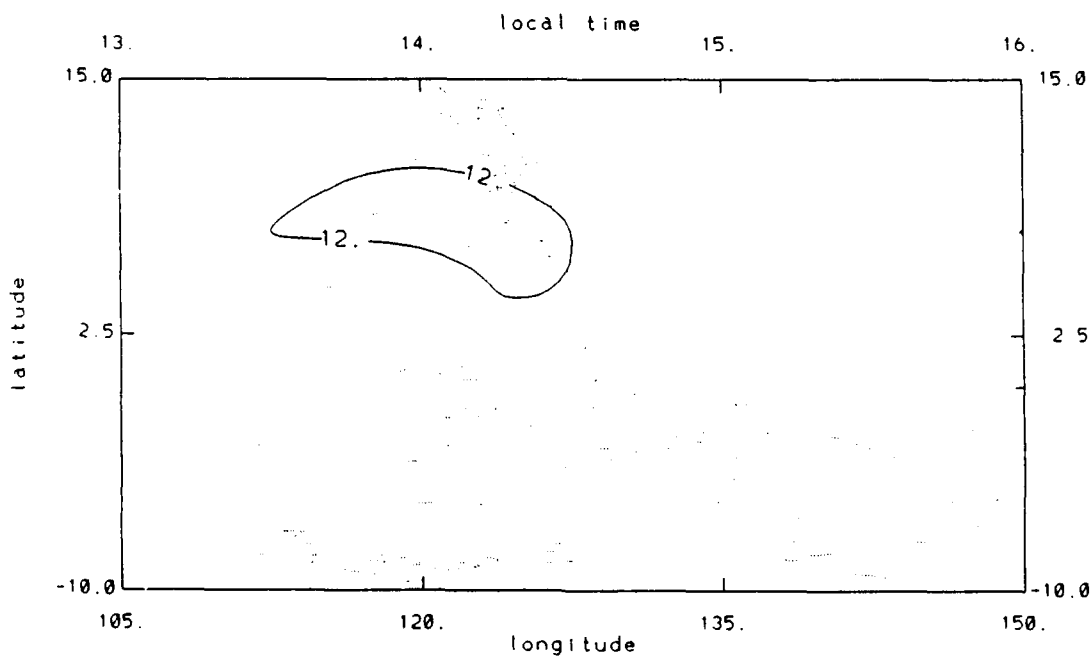


Figure 36. Cloud Top Pressure (kpa) Over the Tropical Ocean Area for the 42h Forecast Time From the 1200 UTC 11 June 1979 Experiment 9 Forecast.

11jun79 12z exp 9 fcst convection values

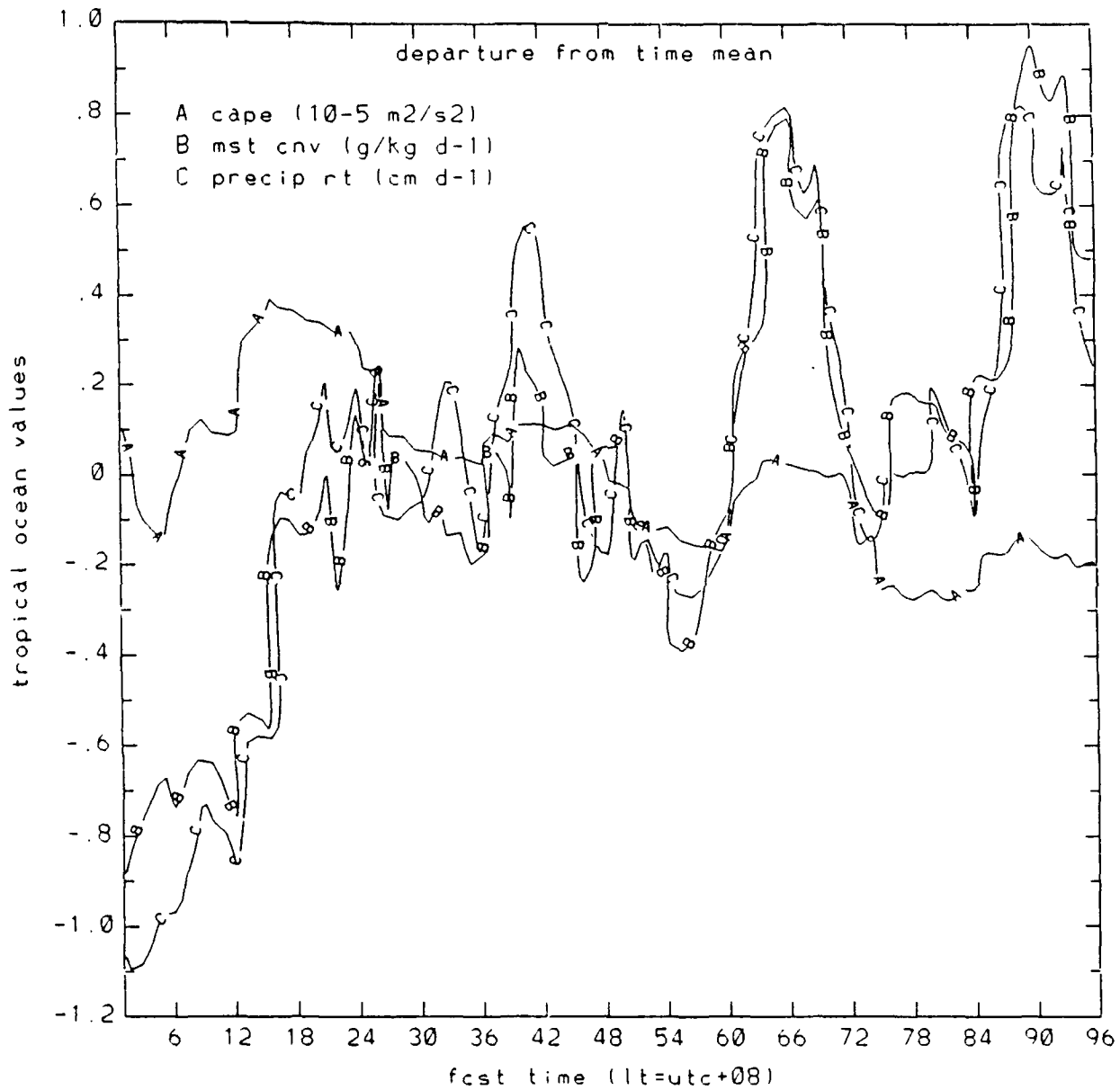


Figure 37. Areal-Averaged Convective Quantities Over the Tropical Ocean Area in Their Departure From the Time Mean Computed Over the First Four Days of the 1200 UTC 11 June 1979 Experiment 9 Forecast.

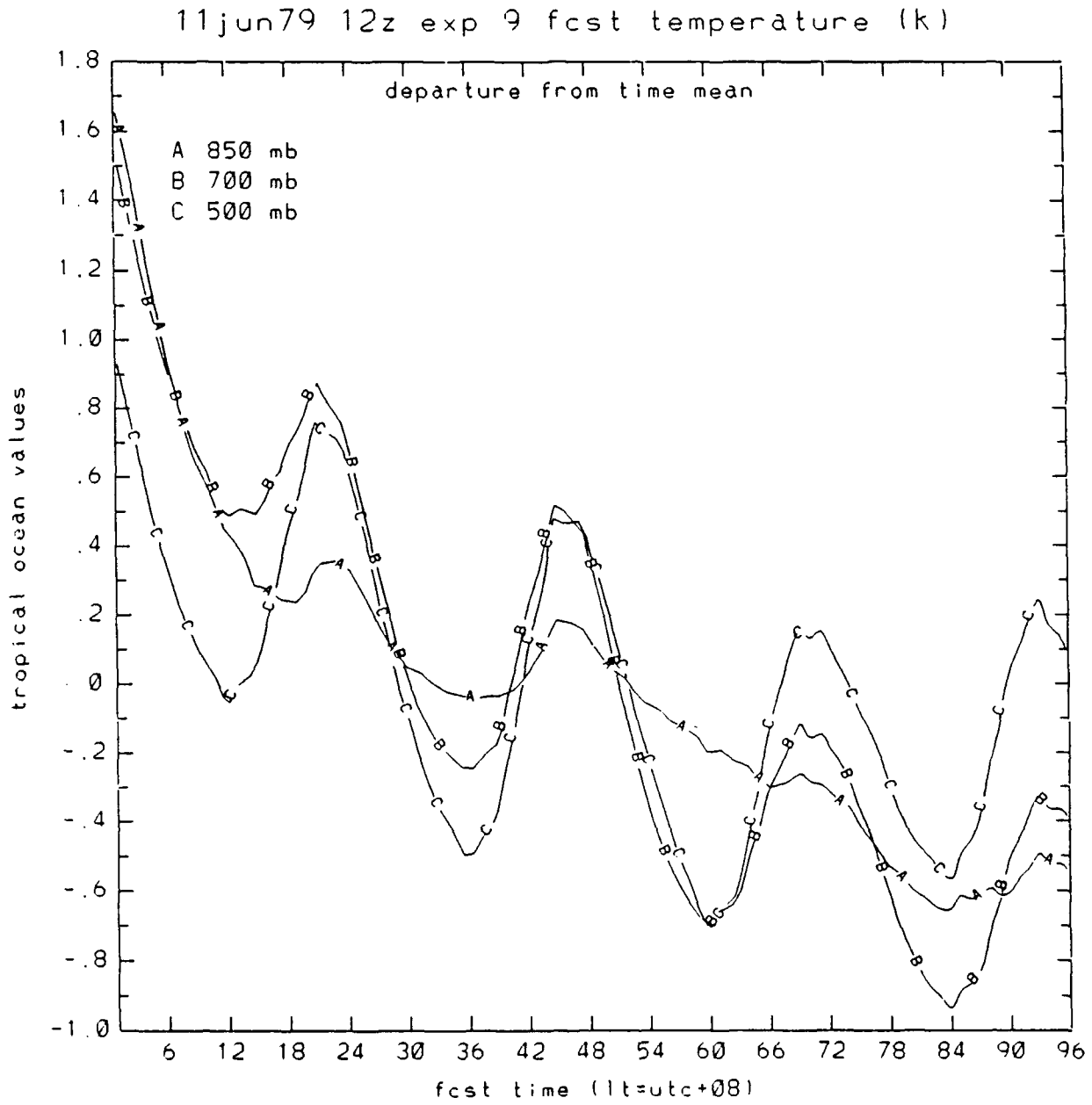


Figure 38. Areal-Averaged Isobaric Temperature (K) Over the Tropical Ocean Area in its Departure From the Time Mean Computed Over the First Four Days of the 1200 UTC 11 June 1979 Experiment 9 Forecast.

temperature maxima about three hours after maxima in the convective activity (about 1700 local) and temperature minima about six hours after convective minima (0800 local). As can be seen in Figure 38, the 850 mb temperature trend is downward, while the 500 mb trend is downward at a lesser rate and actually begins to rise at the end of the period. Thus, 850 mb temperatures are becoming cooler with respect to 500 mb temperatures throughout the region, resulting in greater stability. In fact, the trend at 300 mb (not shown) is to increase in temperature throughout the four-day period. This indicates that stability increases throughout much of the troposphere during the forecast.

To summarize this discussion then, we found that the reductions evident in experiment 9 were well represented in three sub-regions chosen for more extensive study. In the tropical ocean region (Indonesia and Philippines), this reduction led to much better agreement with precipitation observations for a precipitation maximum over the Philippines. While a similar reduction of surplus precipitation was evident over the tropical land region (western Africa), experiment 9 still produced more rainfall throughout the region than could be supported by observations. Over the extratropical land area (western Europe), experiment 9 replicated one observed precipitation maximum but completely missed the other one. Overall, experiment 9 represents improved agreement with observed precipitation compared to experiment 3 by reducing convective precipitation amounts.

We attempted to compare experiment 9 cumulus heating rates in their vertical distribution with those deduced from a tropical budget study²² using observations. It appears that the model-produced cumulus heating maximum is at a slightly higher altitude than the reference profile. Also, the overall integrated heating is considerably greater in the model than in the reference. However, the budget studies are uncertain and the variation of magnitudes of cumulus heating within the tropics can be large. It is fair to say, therefore, that the vertical distribution of model-produced cumulus heating appears to be reasonable.

Horizontal maps of the convective available potential energy (CAPE) over the tropical ocean area revealed a north-south gradient that diminished with increasing

forecast time. The gradient is probably due to the greater surface heating present in the summer hemisphere (to the north in this region). The decrease of area-averaged CAPE during the forecast was found to be caused by a stabilization in the model tropical atmosphere due to the growth of a strong cold bias at low levels and modest warm bias at upper levels. Apparently, imbalances between parameterized heat sources and sinks remain in the GSM, leading to systematic errors that were noted in a series of forecasts. Work is continuing on identifying and correcting the source of these errors.

By contrast, moisture convergence, precipitation, and convective cloud cover generally increased during the forecast period. The latter two quantities were seen to be highly correlated with each other and with moisture convergence both in space and in time. Two significant areas of clouds with tops colder than -70°C were seen: one over an area with heavy precipitation (over islands) and one over an area with moderate precipitation (over the ocean). The latter region had precipitation rates that were less than one-third the heavy precipitation rates. The fractional cumulus cloud amounts in the moderate precipitation area were also about one-third of those in the area of heavy precipitation. This agrees with observational studies (for example, Albright et al.²⁶) that have related fractional deep cumulus cloud coverage to precipitation rates.

The diurnal variation of modeled cumulus convection over the tropical ocean area led to three observations: maximum intensity over islands in the early afternoon, maximum intensity over oceans in the early daylight hours, and little horizontal movement of precipitation anomalies. Averaged over the area, moisture convergence (and thus precipitation rate and cloudiness) showed peak values at 1400 local and minimum values at 0200 local time. Model-produced convection intensified during periods of strongest environmental warming and reached a maximum just before (3h) low-level, large-scale warming changed to cooling. Similarly, decreases in convection

²⁶Albright, M.D., Recker, E.E., Reed, R.J., and Dang, R. (1985) The diurnal variation of deep convection and inferred precipitation in the central tropical Pacific during January-February 1979. *Mon. Wea. Rev.*, **113**:1663-1680.

occurred during large-scale cooling periods and reached a minimum well before (6h) large-scale warming began. Over the four-day forecast, areal-averaged precipitation increased with time even after the initial spin-up period. In just one sample time period it is impossible to determine whether this increase is typical of the model or is case-dependent.

5. GSM EXTENDED RANGE EXPERIMENTS

5.1 Description, Experimentation, and Results

We conducted a series of 10-day forecasts using both experiment 3 (the original Illinois formulation) and experiment 9 versions of MODKUU as the convective parameterization schemes in the GSM. Here, we shall refer to the former version as GL-87 and the new version as GL-89. Both versions used the same radiation and planetary boundary layer parameterizations, so the only difference between the two versions was the cumulus parameterization. The purpose of the series of experiments was to establish more solidly the performance characteristics of the original and improved cumulus schemes through a larger sample of synoptic situations. For comparison, the operational model, GWC84, was included in the 10-day forecast experiments. The 10-day forecasts were initialized from the FGGE III-B analyses of 2, 7, 12, 17, 22, and 27 January 1979 at 1200 UTC, and from 31 May and 5, 10, 15, 20, and 25 June 1979 at 1200 UTC. The 5-day interval between successive forecasts was selected to increase the statistical independence between the individual forecasts.

Figure 39 shows the day-to-day evolution of the Northern Hemisphere temperature bias (forecast-minus-analysis) for the three versions of the model in the January forecasts. An outstanding feature of the figures is the consistency of the error structure from one forecast case to another. GWC84 (part a) produces a substantial mid-tropospheric warm bias in all of the forecasts, and the growth of the bias is steady throughout the ten-day period. GL-87 (part b) is characterized by a more modest warm bias, which increases in magnitude through day 5, then becomes

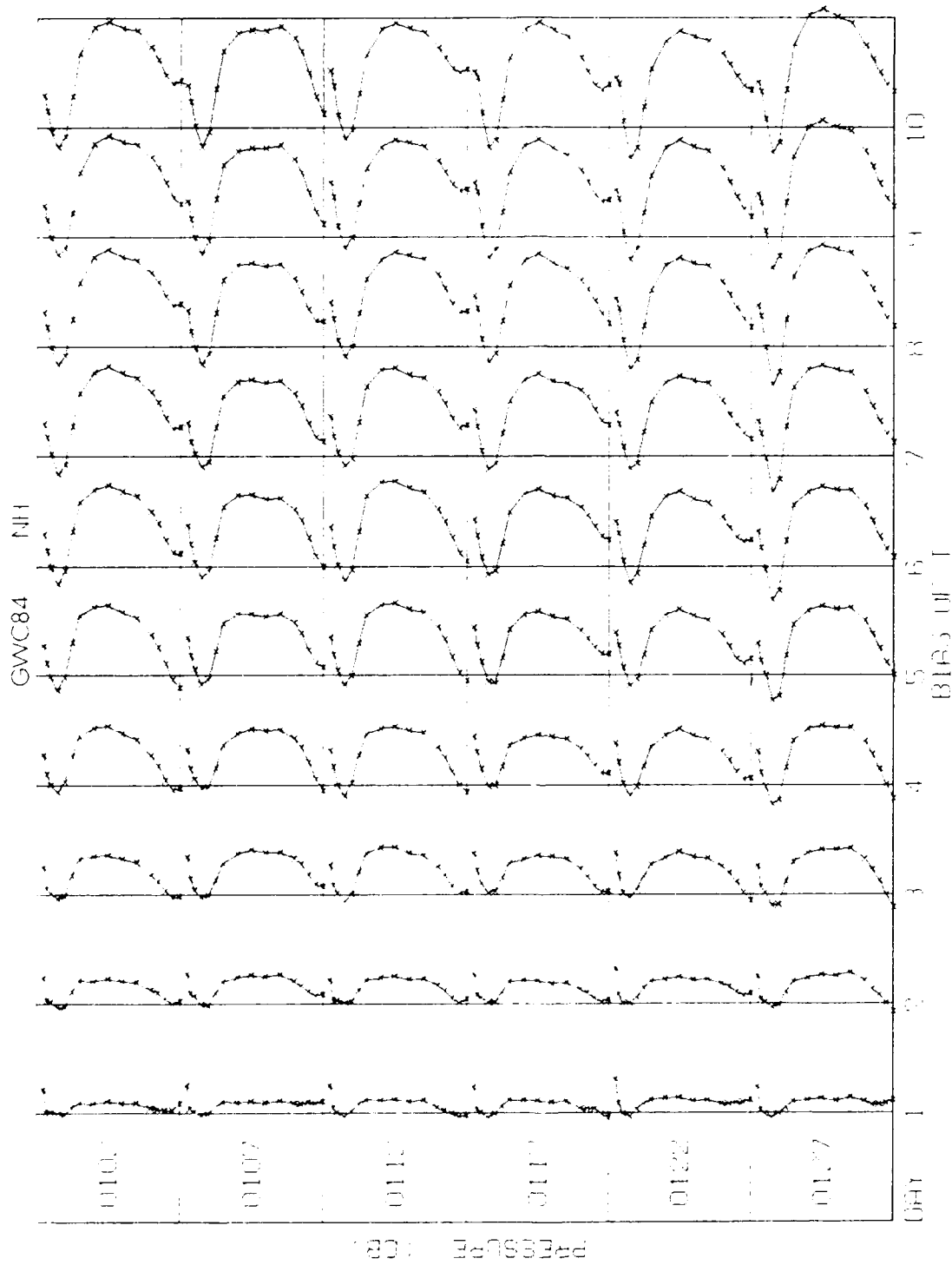


Figure 39. Forecast Days 1-10 Northern Hemisphere-Averaged Temperature Bias (K) of (a) GWC84, (b) GL-87, (c) GL89 Initialized 1200 UTC on Each of the Indicated January 1979 Dates (Width of Each Individual Graph Box is 5 K, Marks on Curves Indicate Position of Mandatory Pressure Levels to 50 kPa).

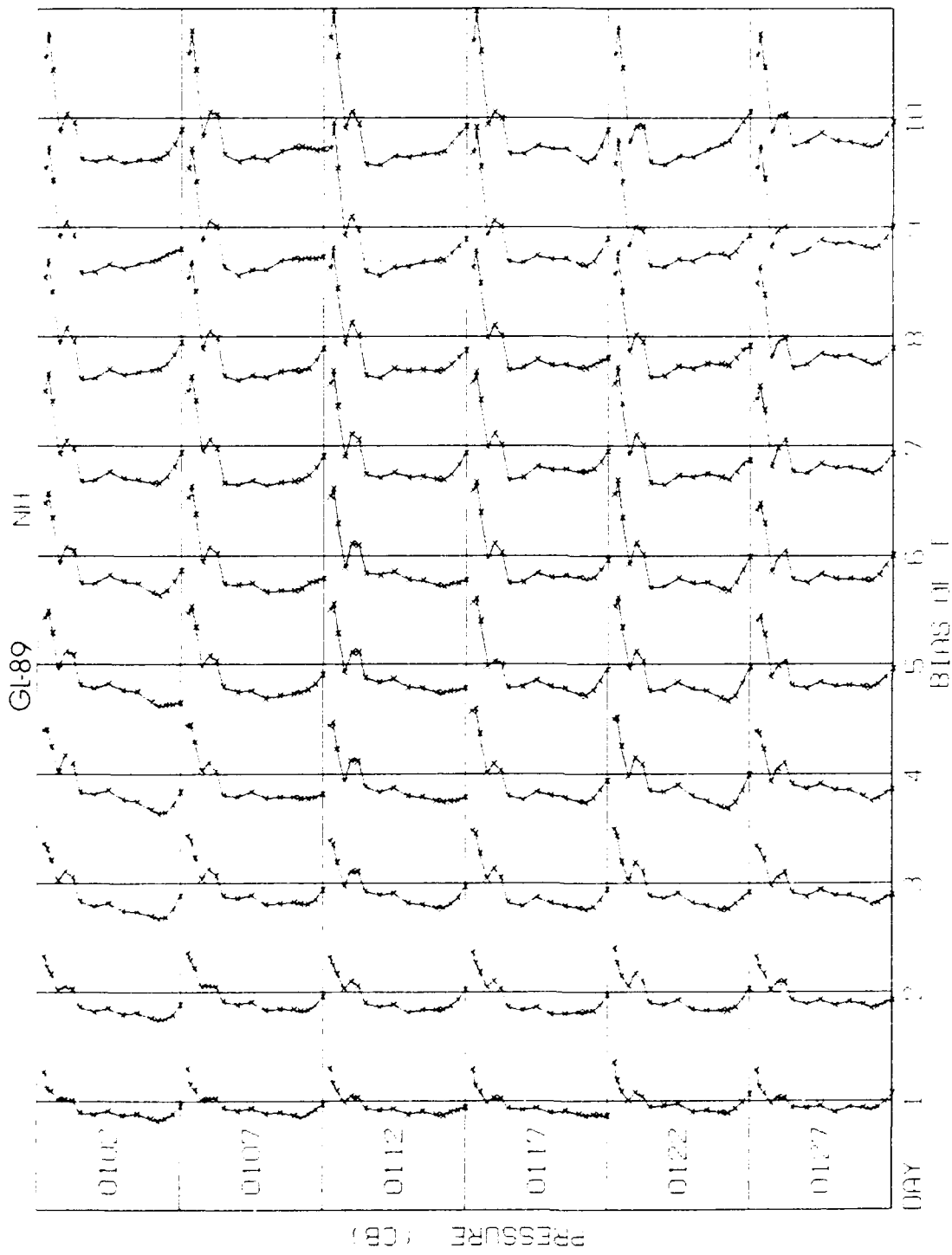


Figure 39. Forecast Days 1-10 Northern Hemisphere-Averaged Temperature Bias (K) of (a) GWC84, (b) GL-87, (c) GL89 Initialized 1200 UTC on Each of the Indicated January 1979 Dates (Width of Each Individual Graph Box is 5 K, Marks on Curves Indicate Position of Mandatory Pressure Levels to 50 kPa).

stationary. Most of the cold bias evident in GL-89 (part c) is apparent by day 5, but the cold bias is somewhat larger at day 10. This suggests that the rate of growth of the bias is considerably slower in the last half of the forecast period. While there is some variation from run to run, in each of the models there is a general pattern of error formation. The difference in the general nature of GL-87 (warm bias) and GL-89 (cold bias) agrees with the difference between zonal cross sections between the two models depicted in Figures 4 and 22.

Since there is such consistency among the six individual forecasts in each of the two periods, we have chosen to present further results of the forecasts in composite or total accumulations. This can be done to represent a typical forecast from each period, and has the advantage of reducing the volume of figures to be produced and described. (At this stage of our GSM development, our focus is on the contribution of each parameterization package to model systematic error.) The diurnal features of the forecasts are not averaged out because each of the six forecasts for the two periods started at 1200 UTC. Thus, the averages over six forecasts are made up of six values all corresponding to the same UTC time.

The case-averaged total precipitation rates for the two periods are shown in Figure 40. All three model versions depict the initial spin-up resulting in maxima that vary greatly between the models. GWC84 precipitation rates drop steadily from its initial weak maximum, while GL-87 rates are off the chart during days 2-4, then drop down to a somewhat lower level that remains basically steady (except for a pronounced diurnal effect). GL-89 depicts a slight drop in the precipitation rate during days 2-5 followed by a relatively steady rate during the last 5 days of the forecast. Both GL-87 and GL-89 exhibit diurnal signals, with amplitudes of about 2 and 0.5 mm/day respectively in the June forecasts (part b). The diurnal amplitudes are a little larger for GL-89 but smaller for GL-87 in January (part a). The climatological global average rates are 2.65 mm/day for January and 2.97 mm/day for June.

The presence of a diurnal signal in the globally-averaged precipitation rates was a surprise to us. We expected that a global average would smooth out those variations. Since the January global-average precipitation rates show the stronger

diurnal signal in Figure 40, we investigated a single January GL-89 forecast. In producing Figure 41, we were able to reveal a correlation between the global rate of total precipitation (Figure 41a) maxima and minima and local maxima and minima in the temporal record of convective precipitation rate averaged over the tropical band (15°S-15°N) (Figure 41b). A clear diurnal pattern is evident in Figure 41b, with the strongest diurnal amplitudes found in the sequence of maxima centered on 150°-165° longitude. The maxima centered on forecast hours 18 (not shown), 42, 66, and 90, correlate well with maxima in the global rates in Figure 41a. These forecast times correspond to local times of 1600-1700. We can also see secondary maxima on the global-average rates at hour 53 (corresponding to the maximum in Figure 41b over 300°-315° longitude [South America at 1500-1600 local time]) and from hour 66 to 76 (corresponding to the Figure 41b maximum over 15°-30° longitude [Africa at 1300-1400 local time]). The dominance of just one longitude sector would create a clear diurnal signal in the globally-averaged precipitation rate curve. Significant nonsynchronous contributions from two or more such sectors tended to spread out and obscure the diurnal signal, as we would expect. The well-defined minima of the globally-averaged rates occur at forecast hours 36, 60, 84, and 108, precisely 6 hours before (or 18 hours after) each of the 150°-165° longitude maxima and immediately after each of the 300°-315° longitude maxima.

The convective precipitation rates shown in Figure 42 show significant contrast in the contribution to total precipitation. By the end of the ten-day period, less than 10 percent of the total precipitation of GWC84 is contributed from convective processes. In the opposite extreme, GL-87 convective precipitation processes totally dominate the stable precipitation generation, making up some 80-90 percent of the total rate. Convective precipitation rates in GL-89 are about 45-50 percent of the total globally-averaged precipitation rates. Not surprisingly, the convective scheme accounts for the entire amplitude of the diurnal variation in the total precipitation rate curve.

The evaporation rates shown in Figure 43 show the same seasonal character as is apparent in the precipitation; the rates for June are somewhat (0.25 mm/day)

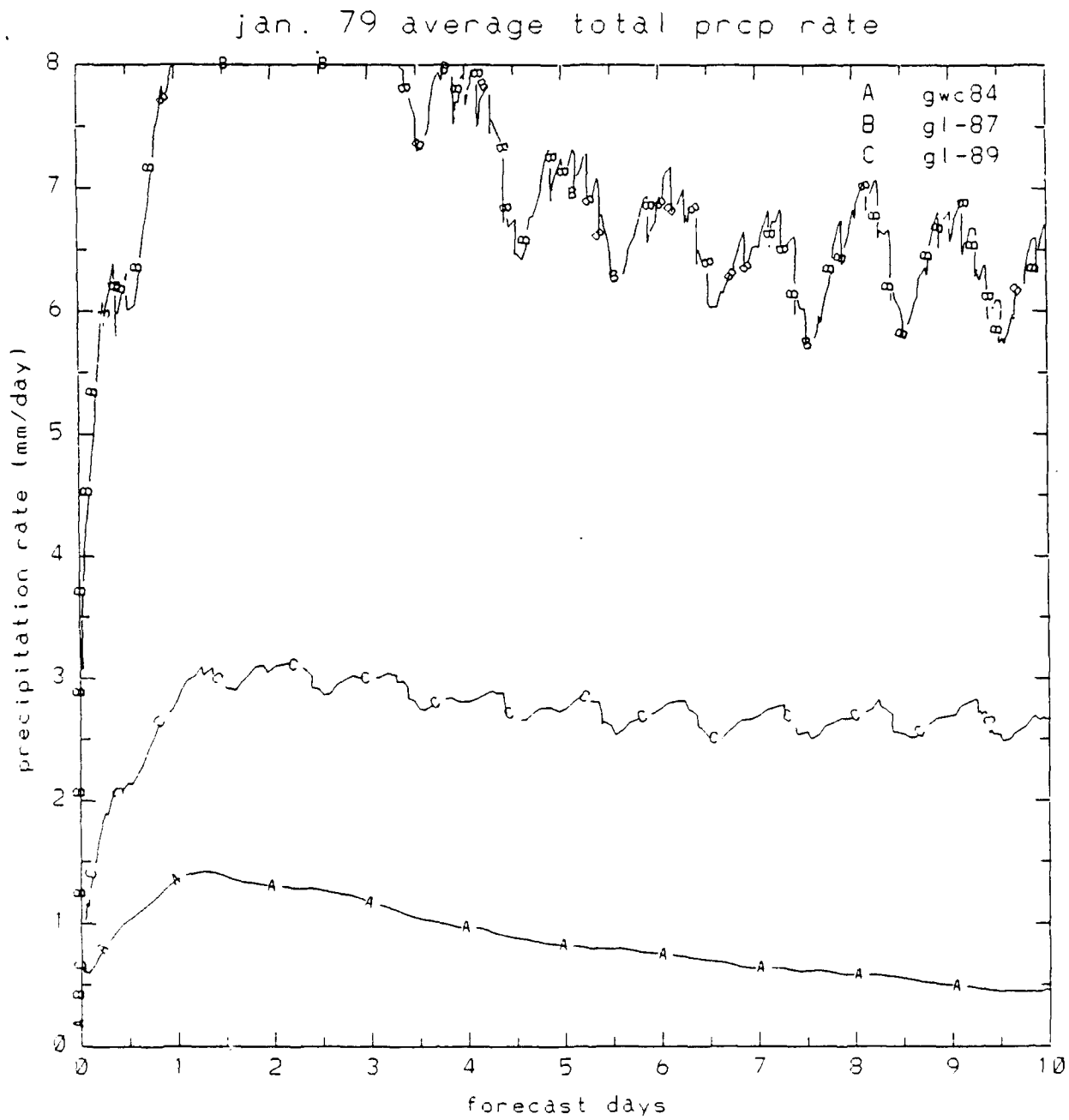


Figure 40. Globally-Averaged Total Precipitation Rates (mm day^{-1}) Averaged Over (a) January and (b) June Forecasts of GWC84, GL-87, and GL-89.

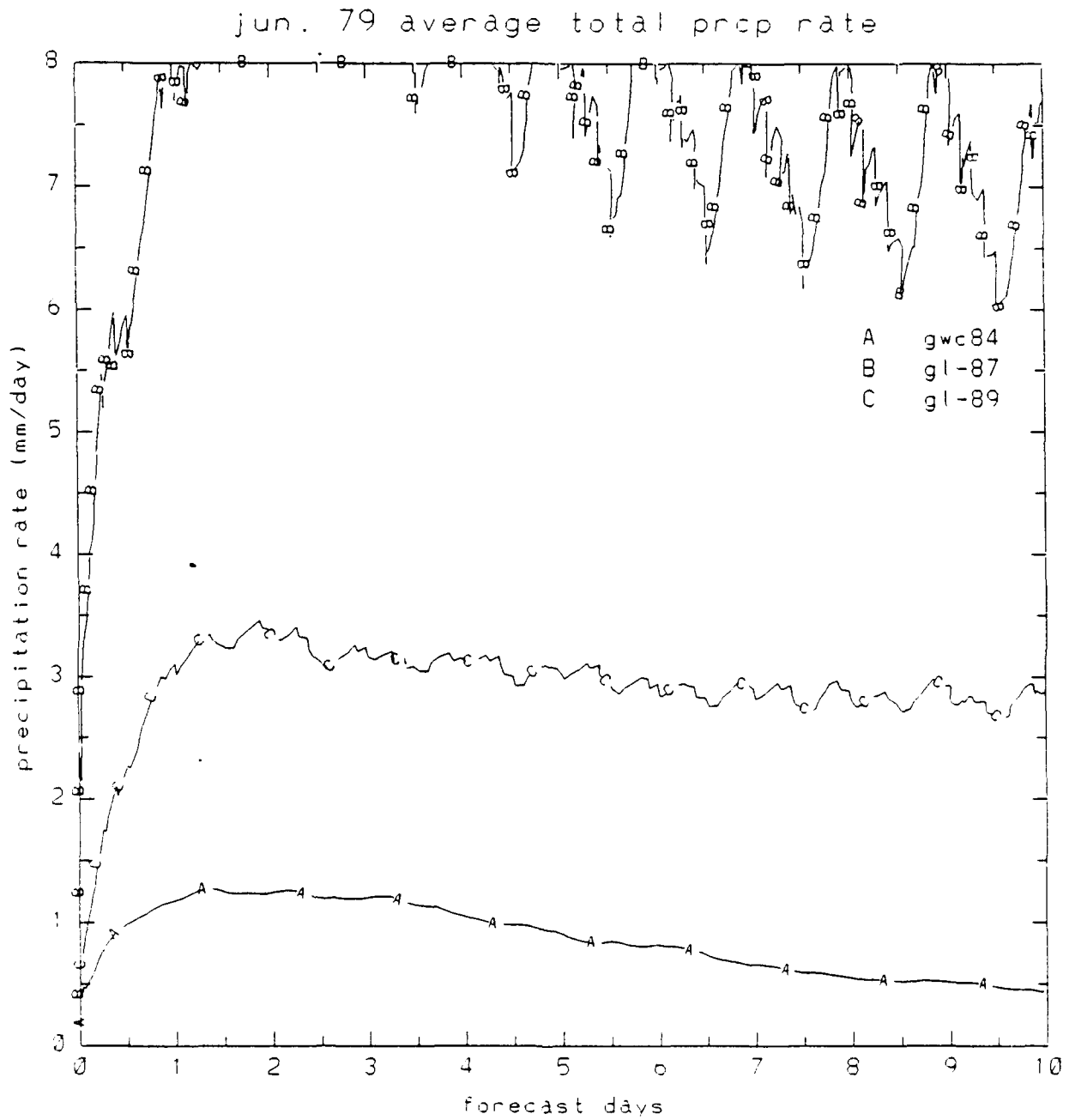


Figure 40. Globally-Averaged Total Precipitation Rates (mm day^{-1}) Averaged Over (a) January and (b) June Forecasts of GWC84, GL-87, and GL-89.

exp. 9 average total prcp rate

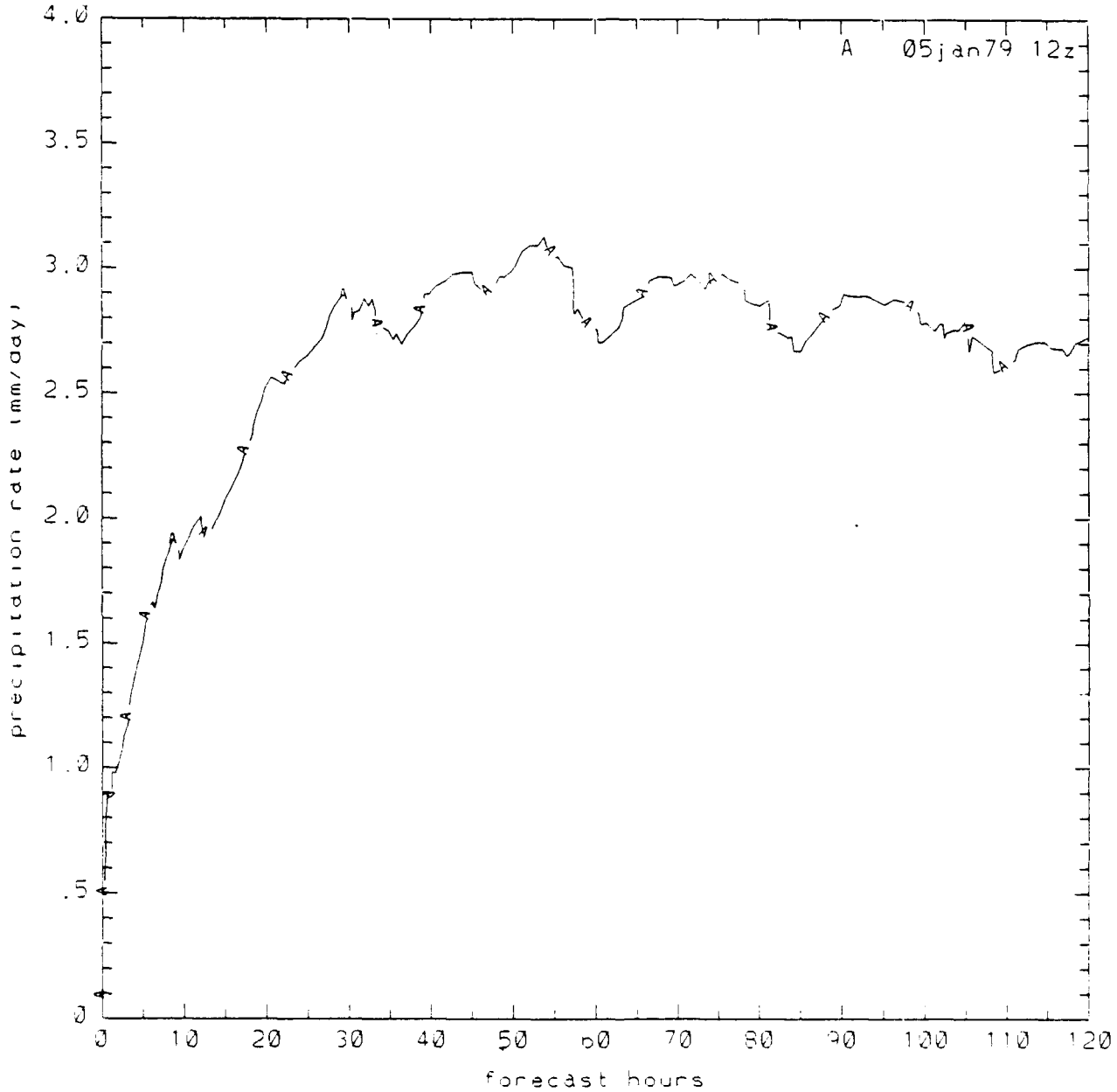


Figure 41. Total Precipitation Rates (mm day-1) (a) Globally-Averaged Total and (b) Latitude-Band (+15°) Averaged Convective for GL-89 Initialized 1200 UTC 05 January 1979.

precip rate (mm/day) exp 9 initialized 05jan7912 z

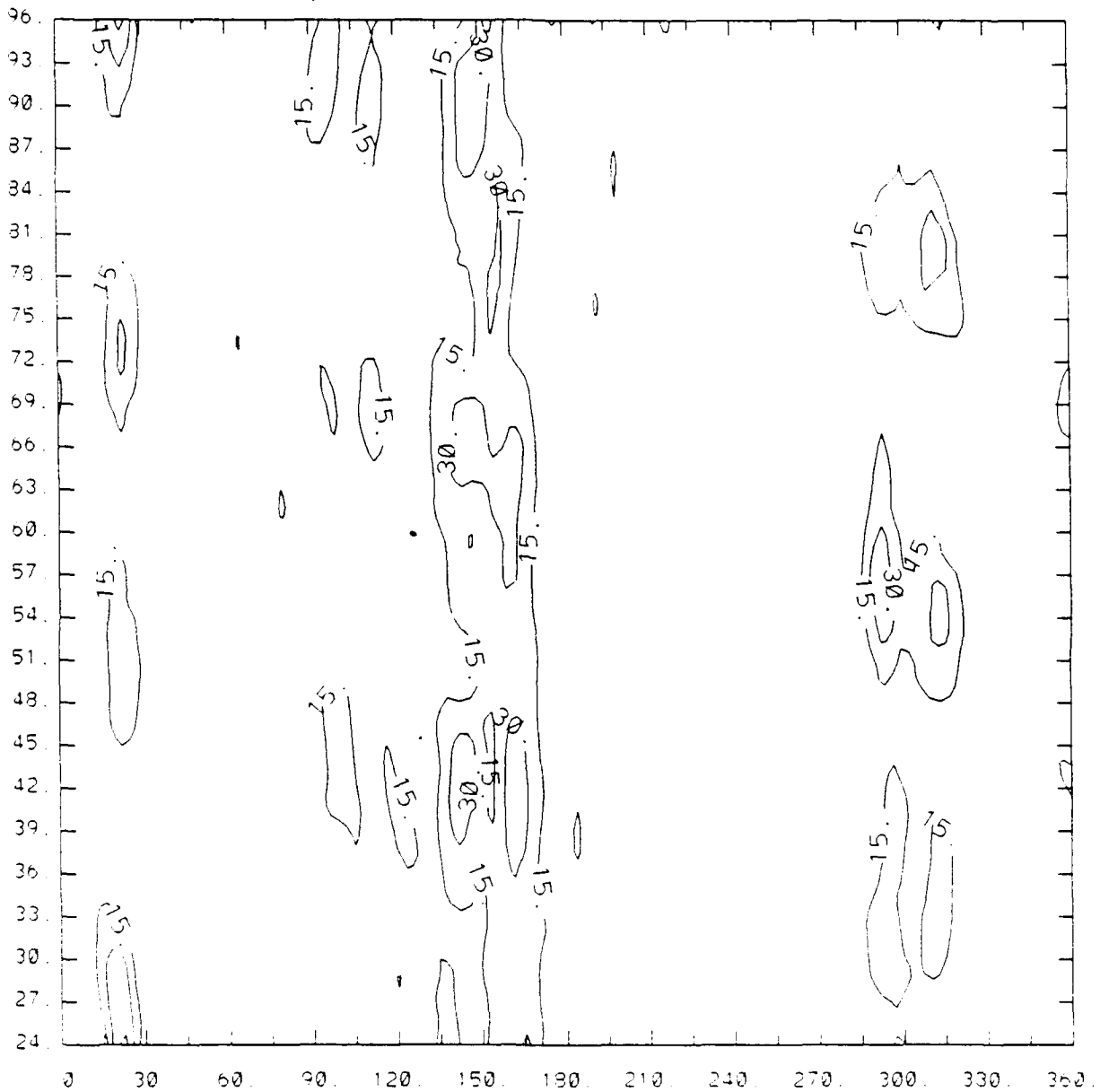


Figure 41. Total Precipitation Rates (mm day⁻¹) (a) Globally-Averaged Total and (b) Latitude-Band (+15°) Averaged Convective for GL-89 Initialized 1200 UTC 05 January 1979.

jan. 79 average conv. prop rate

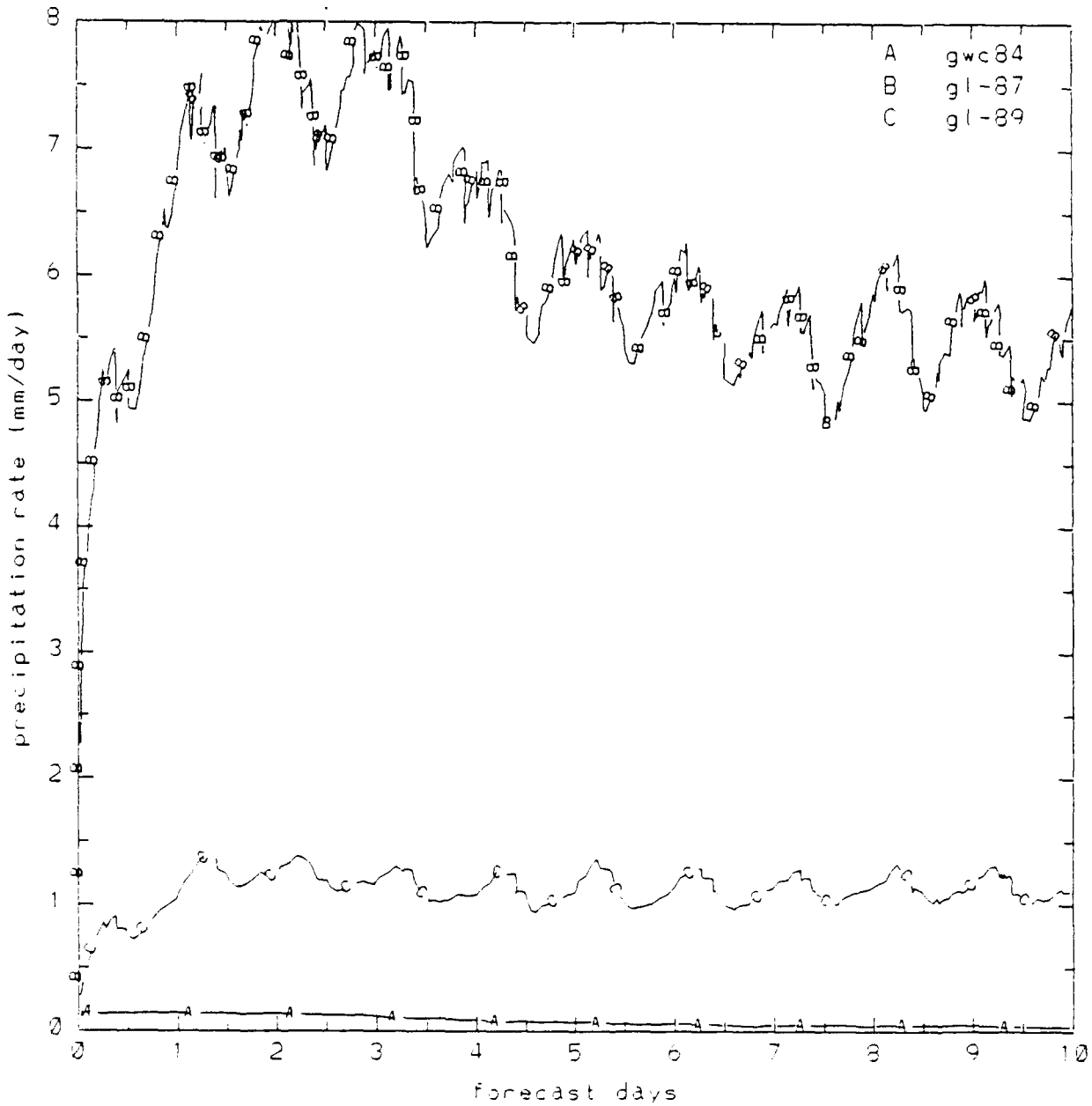


Figure 42. Globally-Averaged Convective Precipitation Rates (mm day⁻¹) Averaged Over (a) January and (b) June Forecasts of GWC84, GL-87, and GL-89.

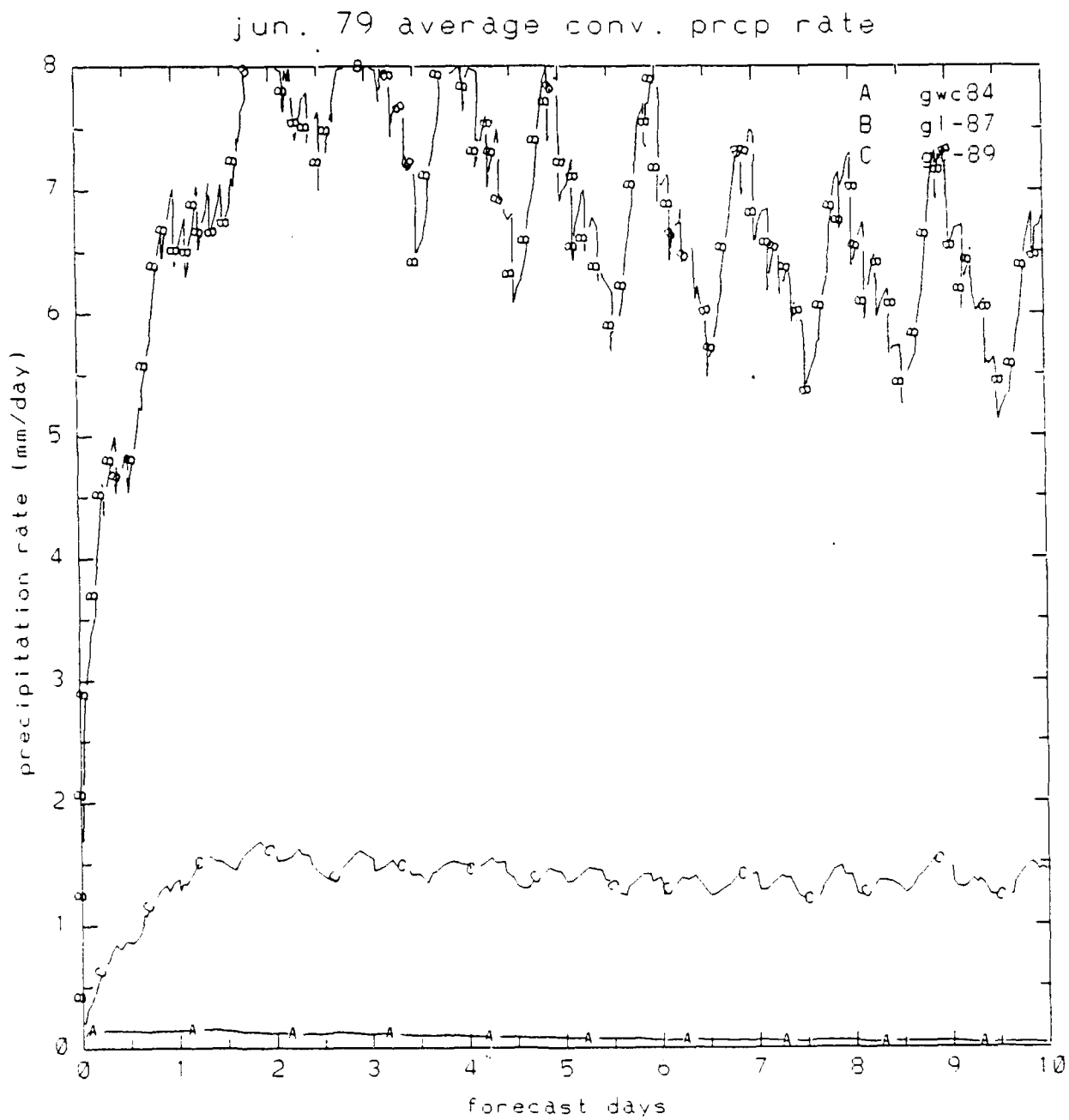


Figure 42. Globally-Averaged Convective Precipitation Rates (mm day^{-1}) Averaged Over (a) January and (b) June Forecasts of GWC84, GL-87, and GL-89.

jan. 79 average total evap rate

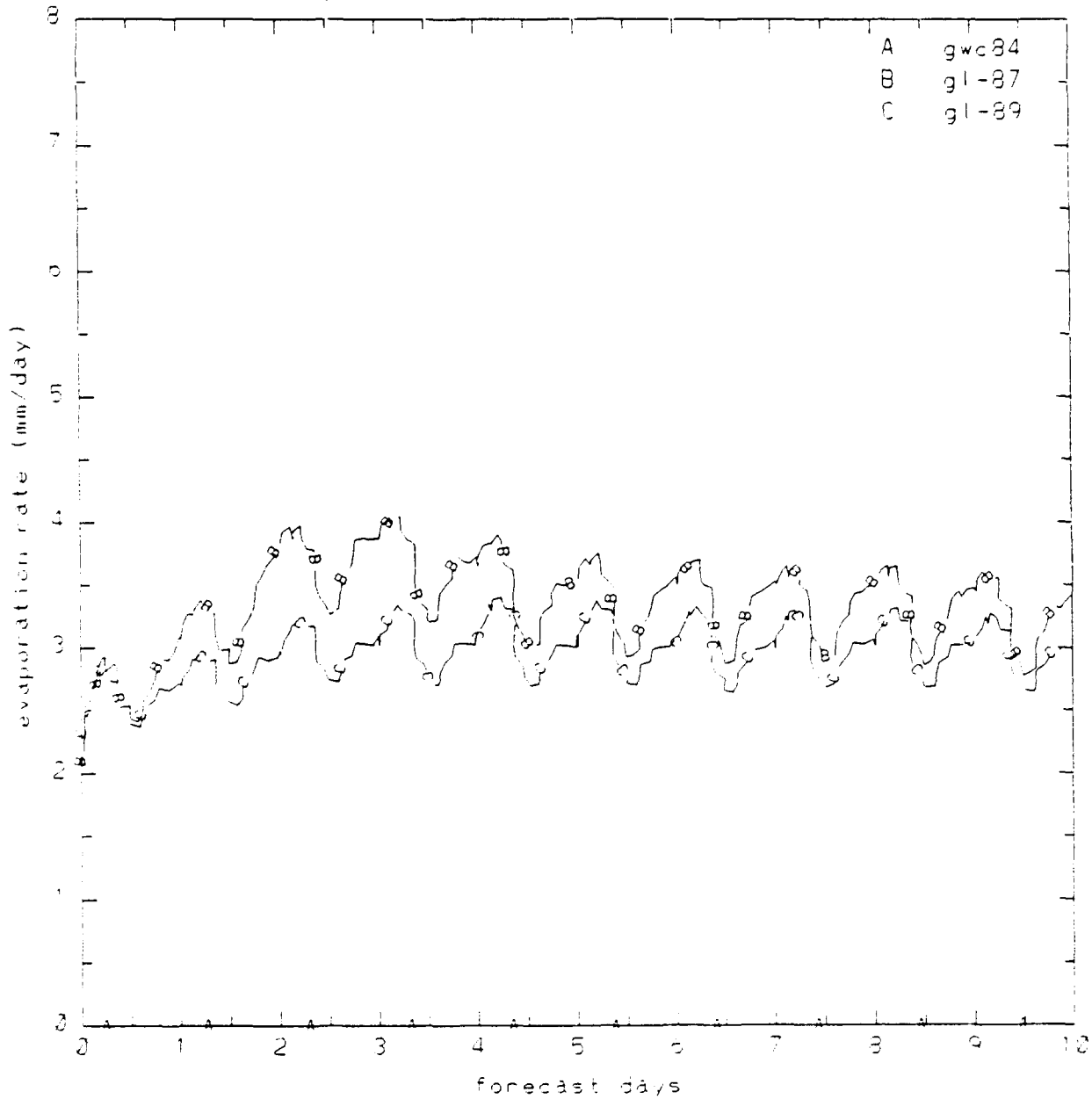


Figure 43. Globally-Averaged Surface Evaporation Rates (mm day^{-1}) Averaged Over (a) January and (b) June Forecasts of GWC84, GL-87, and GL-89.

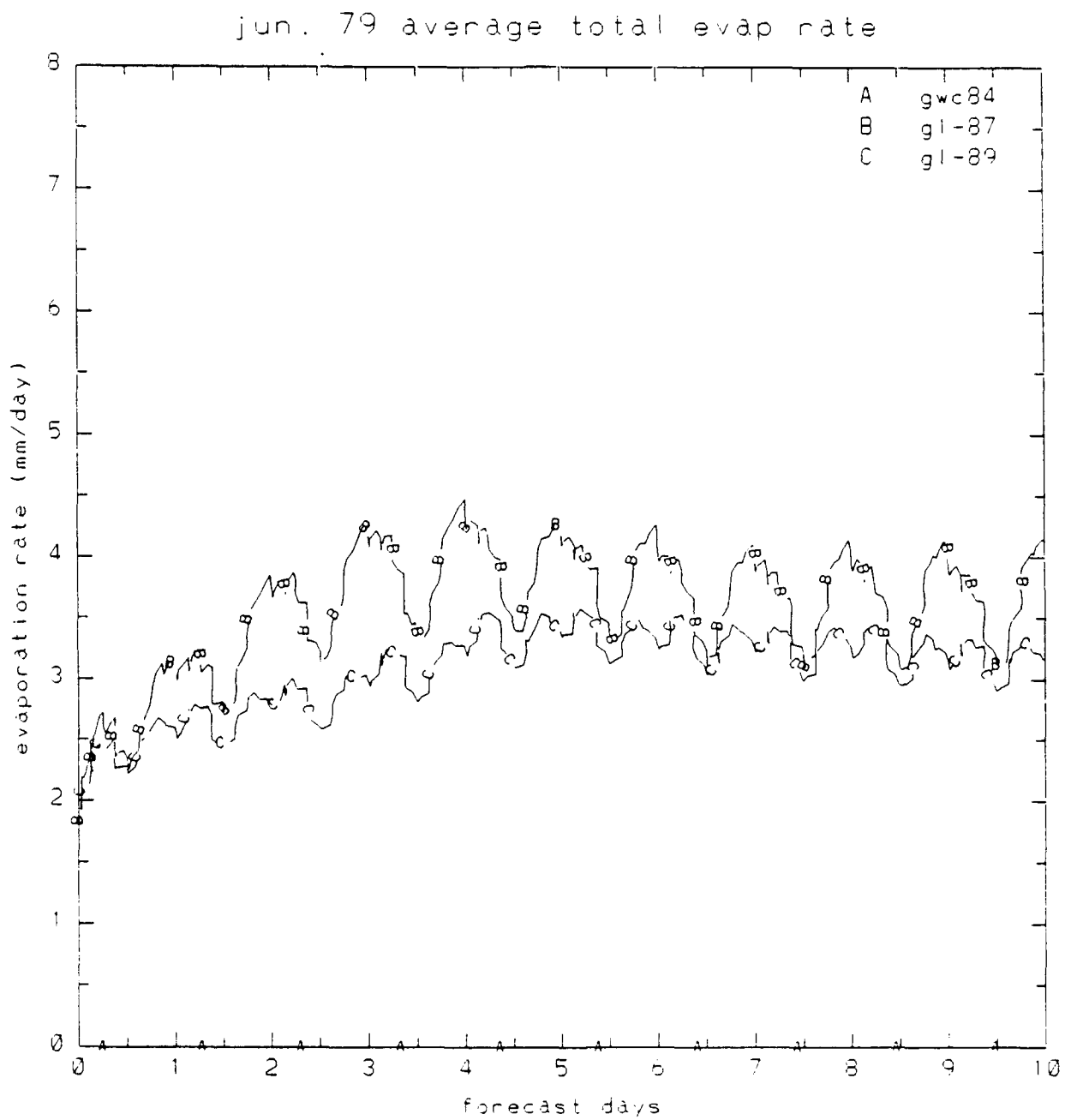


Figure 43. Globally-Averaged Surface Evaporation Rates (mm day^{-1}) Averaged Over (a) January and (b) June Forecasts of GWC84, GL-87, and GL-89.

higher than for January. Another similarity between the evaporation and precipitation curves is found in their diurnal variations, which are perfectly in phase. Also, the relative amplitudes between GL-87 and GL-89 in the two months agree with those seen in the precipitation curves. This is not surprising in light of the fact that surface evaporation is a major source of low-level moisture that supplies the convective processes.

GL-87 evaporation rates are greater than GL-89 rates as in the precipitation curves, but lie well below the GL-87 precipitation rates. By contrast, we see from Figures 40 and 43 that GL-89 evaporation exceeds precipitation rates in both months by as much as 0.5 mm/day, when both rates stabilize later in the forecast period. The relative magnitudes of precipitation and evaporation would suggest that the GL-87 atmosphere is losing water vapor, while the GL-89 atmosphere is gaining water vapor. However, the daily forecast values of vertically-integrated global RMS specific humidity plotted in Figure 44 reveal a decline in the global water vapor content of the atmosphere in both GL-87 and GL-89. Day 10 values in GL-89 are 93 percent of initial values for both January and June. The day 10 values for GL-87 are 86 and 87 percent of initial values respectively for January and June. The rate of decrease is greater for both models in the first 5 days of the forecast, then tends to level off beyond that point for GL-89 and drops more slowly beyond 5 days for GL-87.

From this point forward in the presentation of experimental results, we will use forecast accumulation of precipitation over 30 days for each month to facilitate comparisons with monthly climatology data. This accumulation was computed by adding together the accumulation from days 2-6 of each of the six forecasts for each month. Using days 2-6 avoids the spin-up in the first day and the likely degraded forecast quality in the last 4 days. By adding together six contiguous 5-day periods of accumulation, we can approximate each model's monthly total precipitation for January and June.

Figure 45 depicts the zonally-averaged accumulated total precipitation for the two months. All three model results are shown along with the Jaeger²⁰ climatology. GWC84 precipitation is less and GL-87 precipitation is greater than climatology at

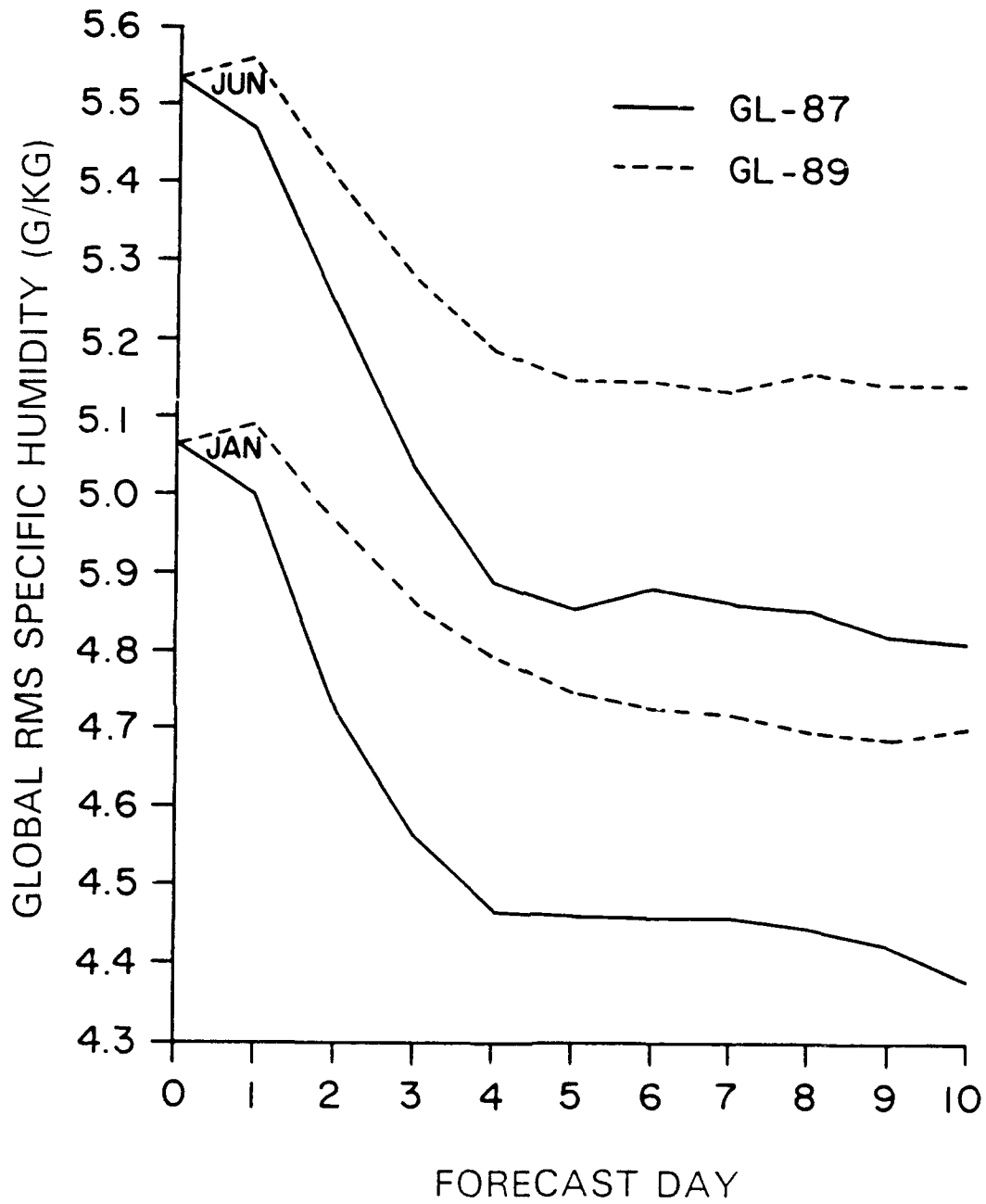


Figure 44. Vertically-Integrated Global Root-Mean-Square Specific Humidity (g kg^{-1}) for the 17 January 1979 and 15 June 1979 GL-87 and GL 89 Forecasts.

jan. 79 zonal ave accumulated total prop

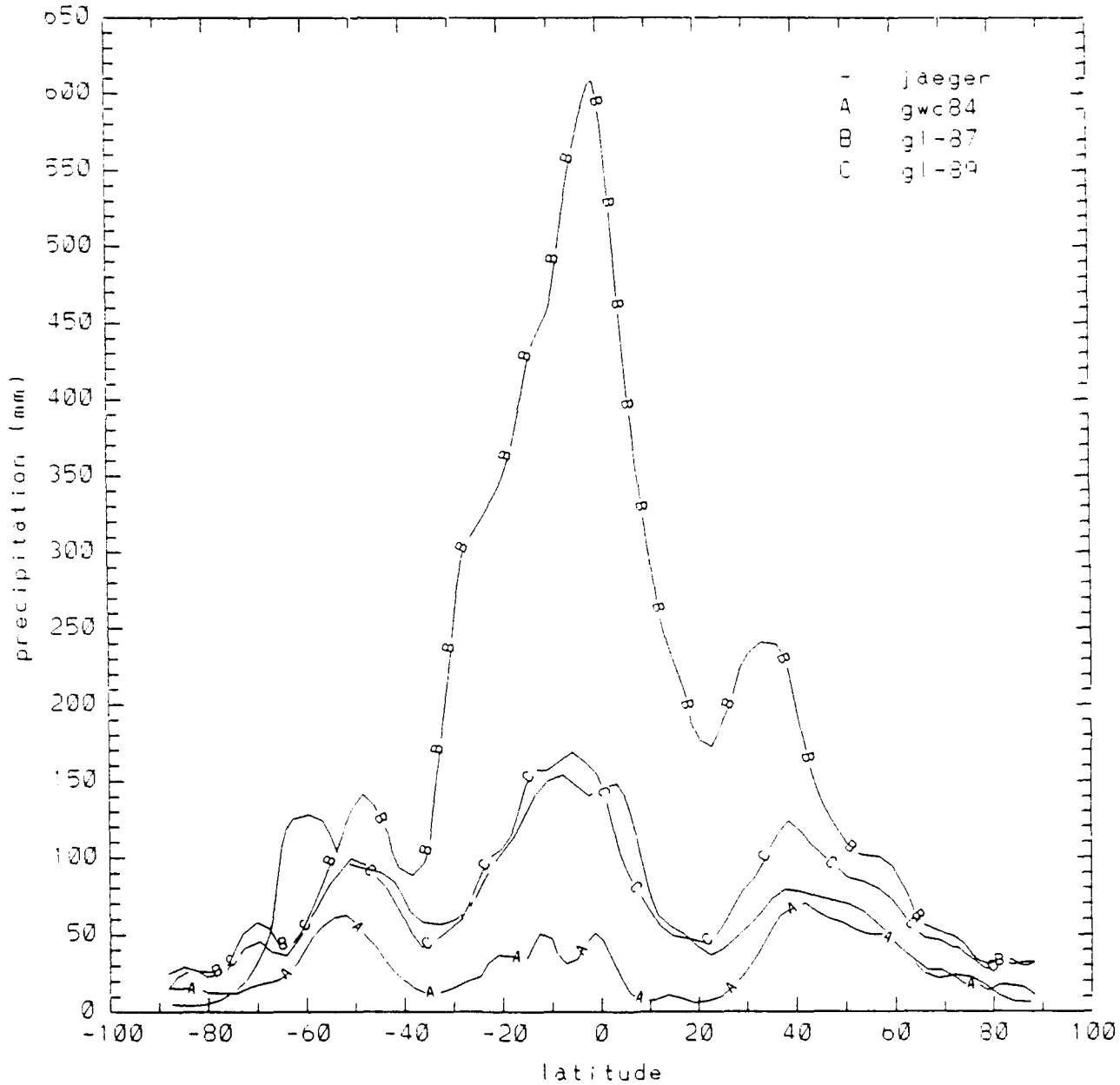


Figure 45. Zonally-Averaged Accumulated Convective and Large-Scale Precipitation (mm) Summed Over Days 2-6 of All (a) January and (b) June Forecasts of GL-89.

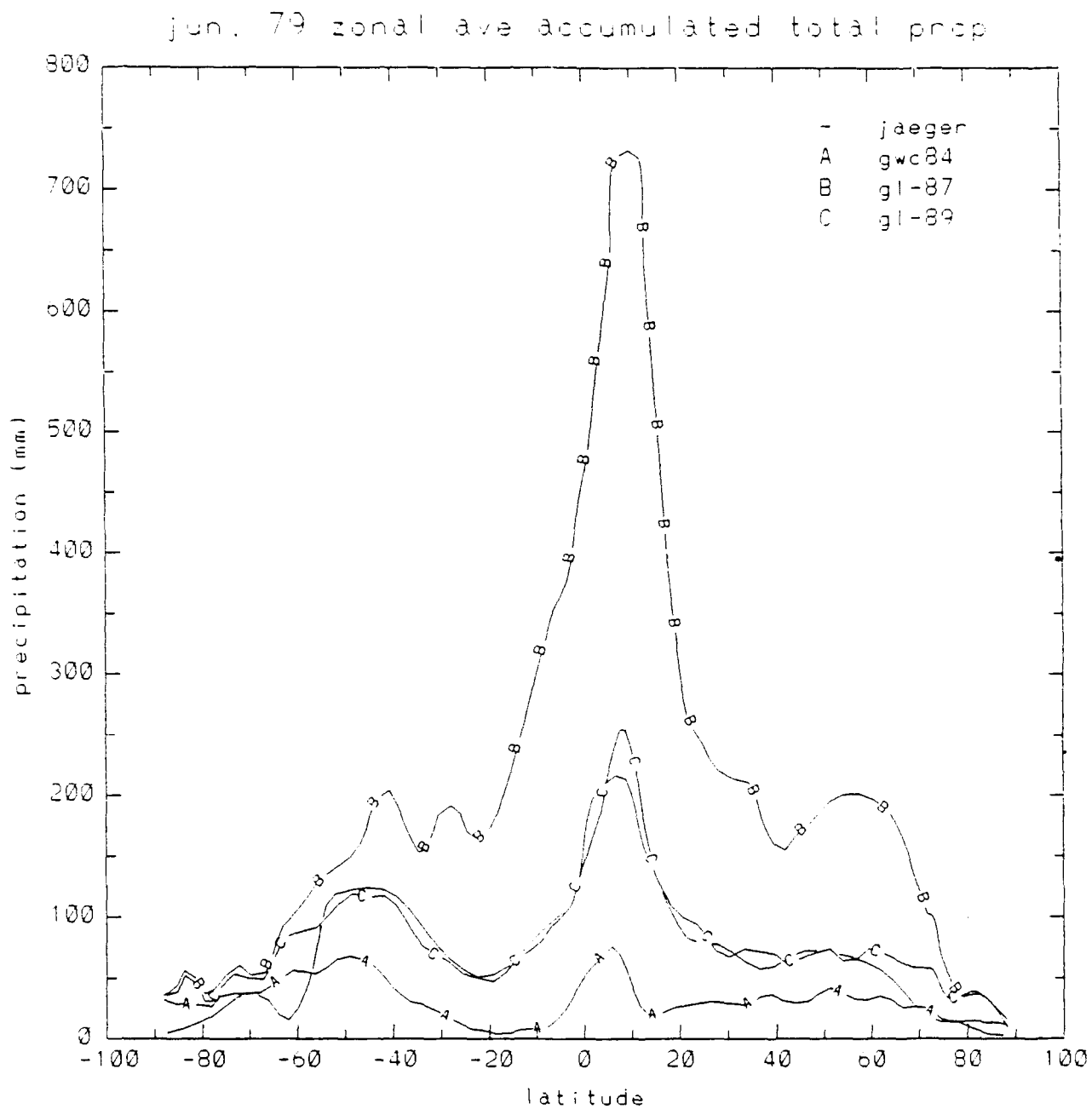


Figure 45. Zonally-Averaged Accumulated Convective and Large-Scale Precipitation (mm) Summed Over Days 2-6 of All (a) January and (b) June Forecasts of GL-89.

nearly all latitudes. GL-89 precipitation distribution agrees fairly well with climatology equatorward of 60° , where climatological values can be considered most valid.

The climatological distribution of precipitation is generally trimodal, with the largest peak shifted toward the summer hemisphere by just slightly less than 10° of latitude. The two lesser peaks lie in the mid-latitudes of both hemispheres. In both months, the Southern Hemisphere maximum is greater than that of the Northern Hemisphere. In the Southern Hemisphere, the winter mid-latitude (30° - 60°) precipitation is greater than the summer values. In the Northern Hemisphere mid-latitudes, the summer and winter precipitation amounts are about the same.

GL-89 zonally-averaged mid-latitude precipitation amounts in the Southern Hemisphere also indicate larger wintertime values. However, unlike climatology, the wintertime GL-89 mid-latitude precipitation in the Northern Hemisphere exceeds the summertime amounts. To better understand this characteristic of GL-89, we show the breakdown of the total precipitation into convective and large-scale (stratiform) components in Figure 46. Stratiform processes produce the dominant precipitation amounts in the Northern Hemisphere winter mid-latitudes, with a minor maximum of about 30 mm contributed by convective processes. When combined, these processes produce as much winter mid-latitude precipitation in the Northern Hemisphere as in the Southern Hemisphere. Even in the summertime, large-scale precipitation dominates convective rainfall in the middle latitudes of both hemispheres. Convective precipitation is dominant only in the tropics.

Having established the fact that GL-89 is the only model that resembles climatology in the magnitude of precipitation rate and in the latitudinal distribution of monthly precipitation, we will consider only GL-89 in further discussion of model results. We present maps of GL-89 30-day accumulated convective precipitation for January and June in Figure 47. To verify the positions of the convective maxima on the two maps, we present depictions of observed outgoing longwave radiation (OLR)

jan. 79 zonal ave accumulated gl-89 prec

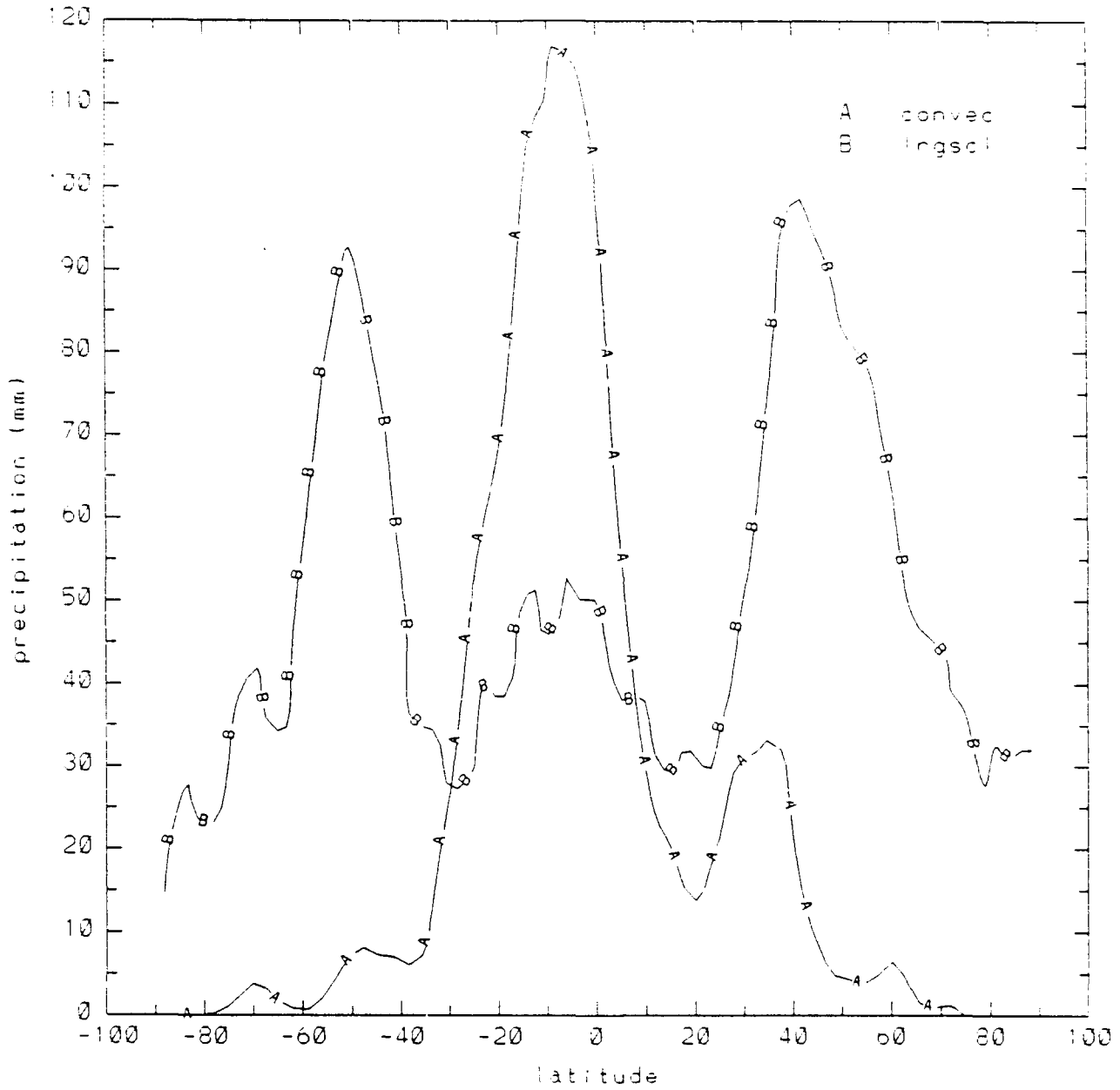


Figure 46. Zonally-Averaged Accumulated Convective and Large-Scale Precipitation (mm) Summed Over Days 2-6 of All (a) January and (b) June Forecasts of GL-89.

jun. 79 zonal ave accumulated gl-89 prcp

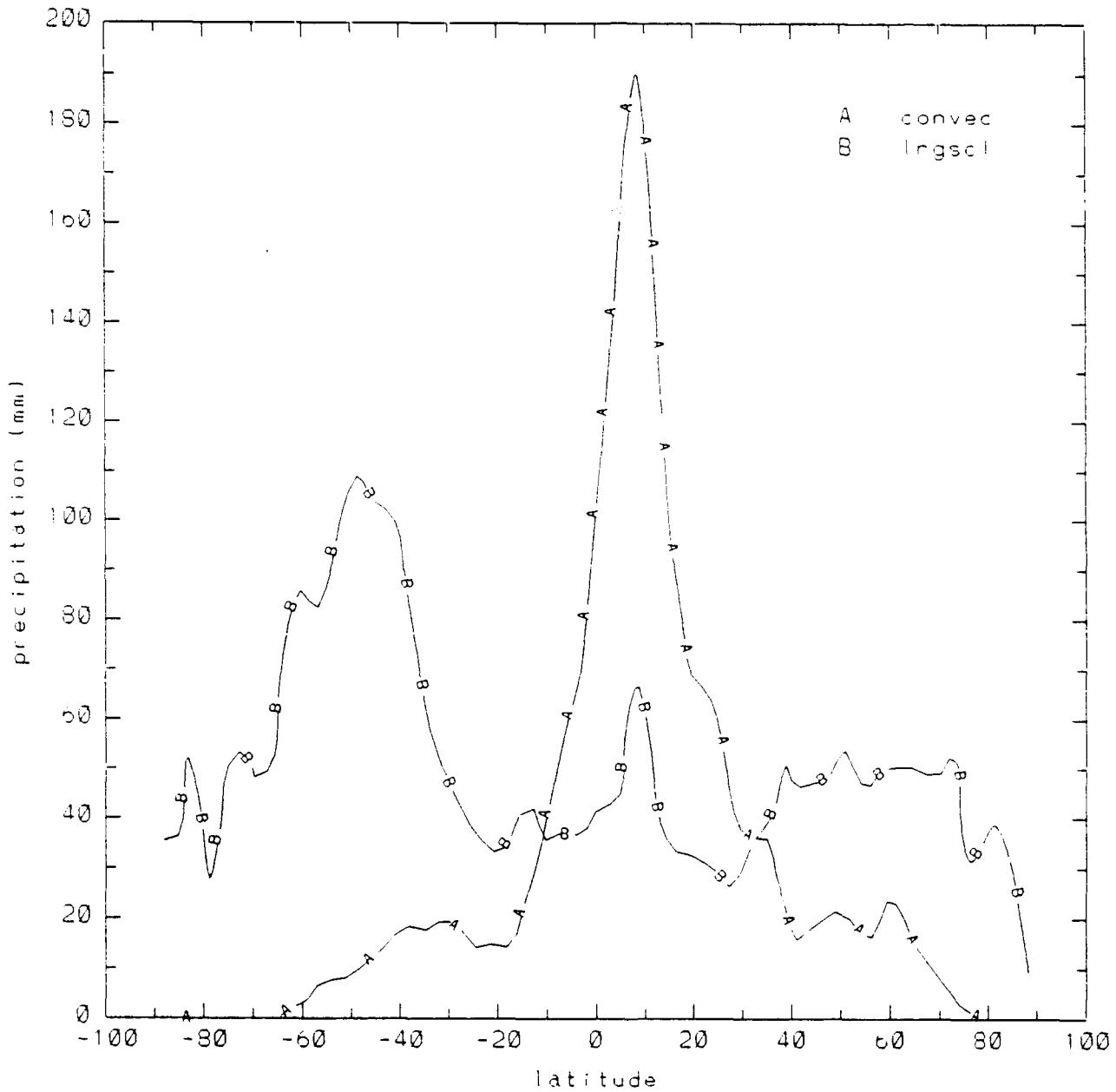
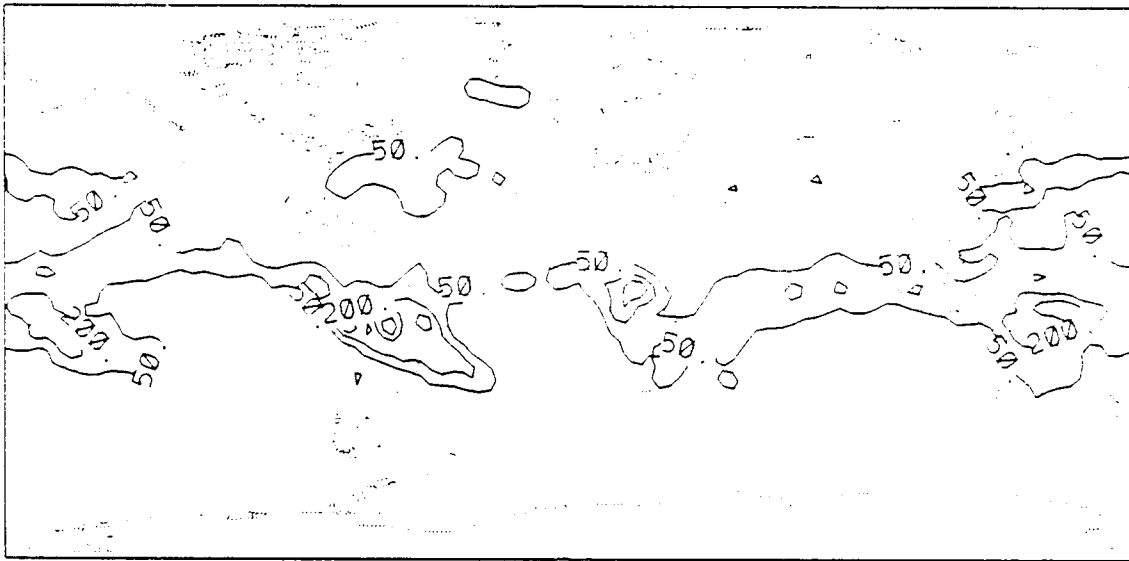


Figure 46. Zonally-Averaged Accumulated Convective and Large-Scale Precipitation (mm) Summed Over Days 2-6 of All (a) January and (b) June Forecasts of GL-89.

gl-89 prcp (mm) 30d conv. jan 79



gl-89 prcp (mm) 30d conv. jun 79



Figure 47. Maps of Accumulated Convective Precipitation (mm) Summed Over Days 2-6 of All (a) January and (b) June Forecasts of GL-89 (Contour Interval is 150 mm).

from Bess and Smith²⁷ for the same months in Figure 48. The areas of minimum OLR in the tropics represent areas of high clouds that are emitting at much colder temperatures than the surrounding clear areas. Thus, these areas most likely represent regions of stationary deep convection for the given month. Note the movement of these convectively active regions from south of the equator in January to north of the equator in June. We can qualitatively assess of the model simulation by comparing the positions of the model-produced convective maxima (Figure 47) with the positions of the OLR minima (Figure 48).

Figure 49 shows maps of the total accumulated precipitation generated by GL-89. In the tropics, we see that the maxima coincide with the maxima of convective precipitation in Figure 47. The maxima in the total precipitation maps have been enhanced by stratiform precipitation. In addition, regions of total precipitation minima (less than 50 mm) are evident to the west (downstream in the trade winds) in both months, but especially in January. To demonstrate the realism of this pattern of maxima and minima in the tropics, we reproduce a January climatological precipitation map by Jaeger²⁰ as Figure 50. This map shows regions of 50 mm or less that roughly coincide with the dry regions of the GL-89 January map west of South America, west of Africa, and northwest of Australia. Even the maximum regions enclosed by the 200 mm contour over South America, central Africa, and New Guinea are in reasonably good agreement between the two maps.

We now return to the issue of the enhancement of precipitation in areas of maximum tropical convection by stratiform precipitation. This pattern is clearly evident in Figure 51, which depicts the longitudinal distribution of convective and stratiform precipitation from GL-89 in the tropical convection zone. In January over Africa (20°-30° longitude) and South America (280°-320° longitude), stratiform precipitation maxima directly coincide intense convective precipitation. This is also

²⁷Bess, T.D., and Smith, G.L. (1987) *Atlas of Wide-Field-of-View Outgoing Longwave Radiation Derived From Nimbus 7 Earth Radiation Budget Data Set - November 1978 to October 1985*, NASA Reference Publication 1186, NASA Langley Research Center, Hampton, Virginia, pp. 11, 21.

January 1979

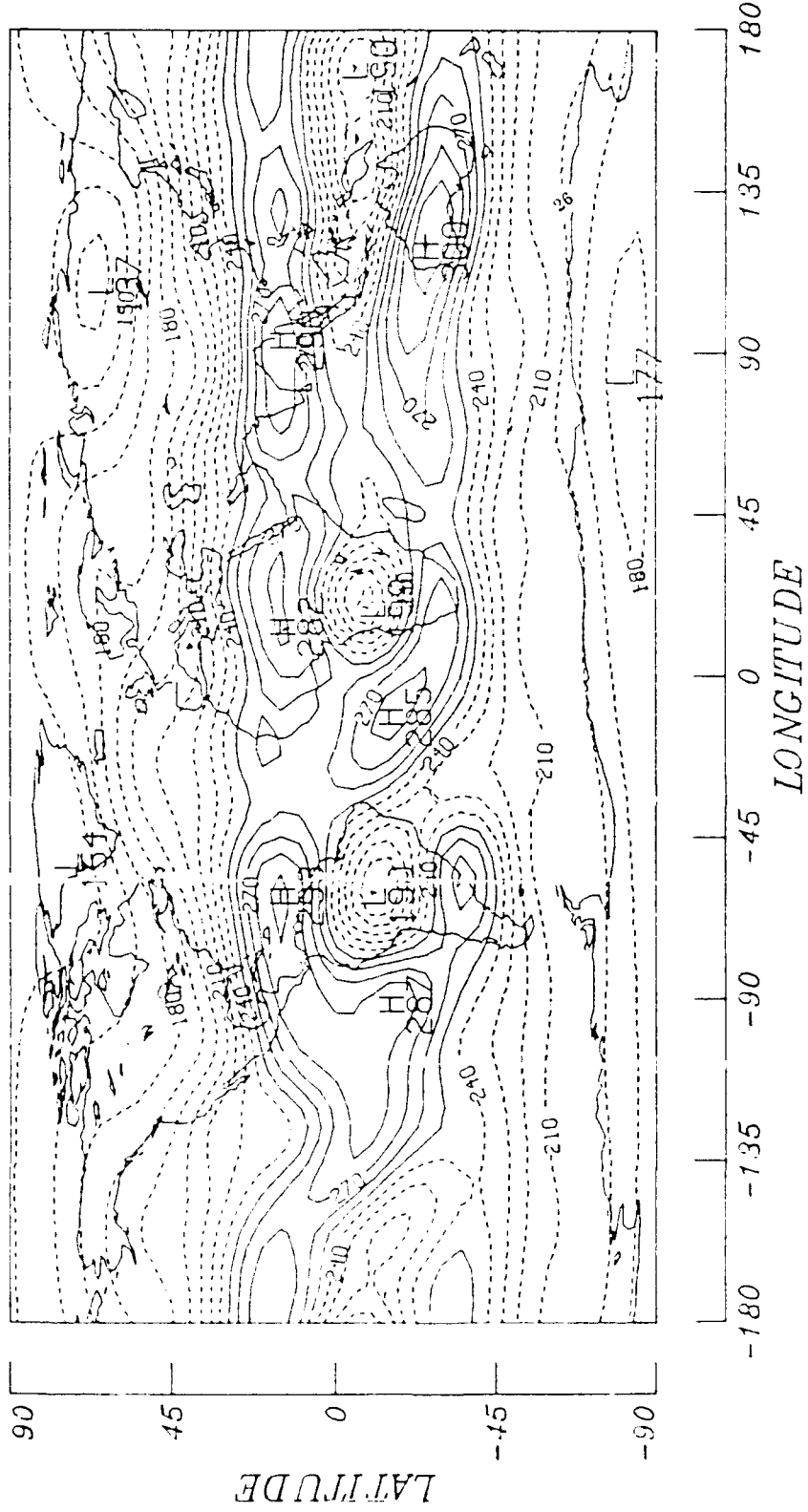


Figure 48. Maps of Outgoing Longwave Radiation ($W m^{-2}$) At the Top of the Atmosphere for (a) January and (b) June of 1979 Taken from Bess and Smith²⁷.

June 1979

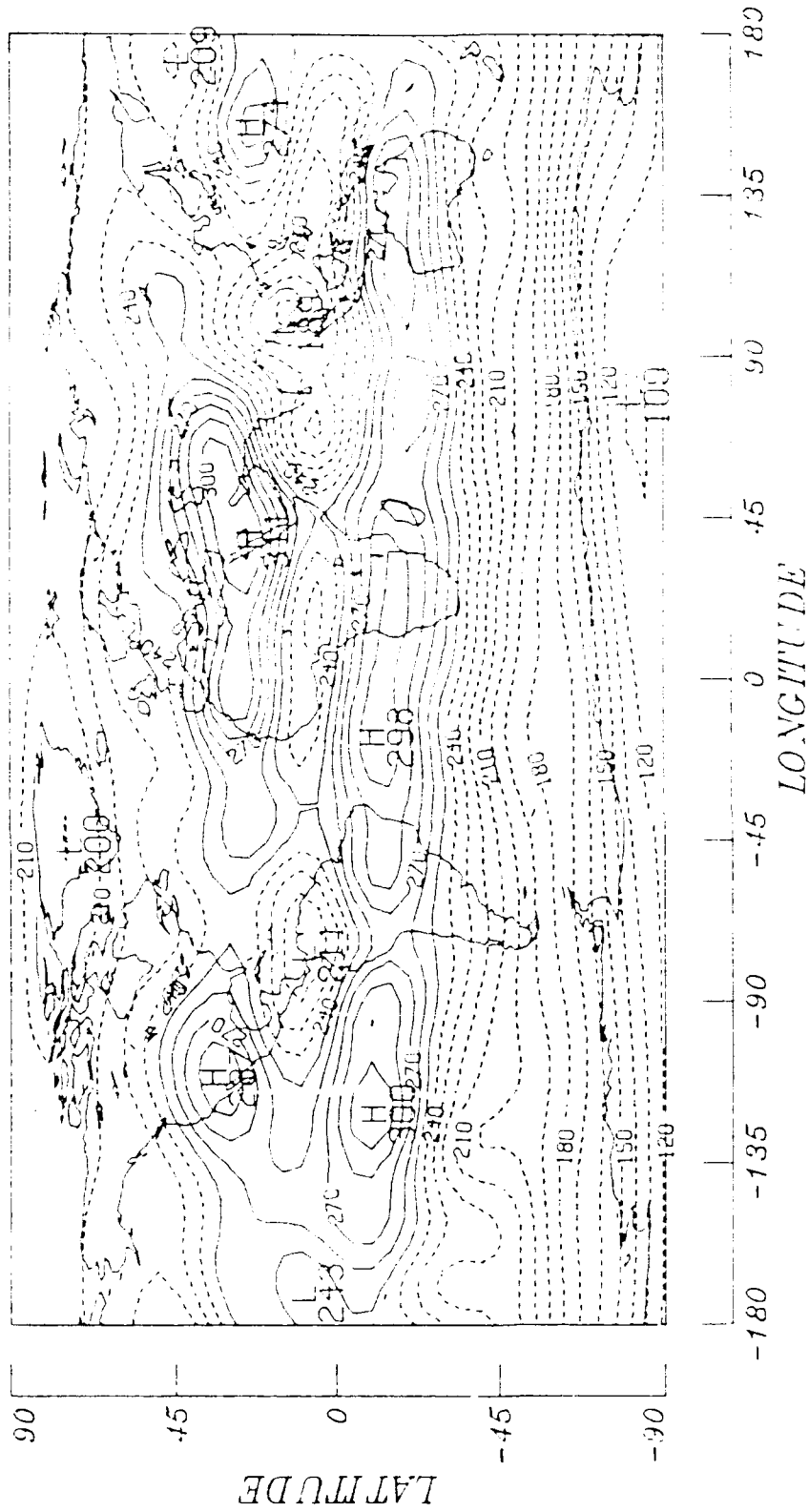
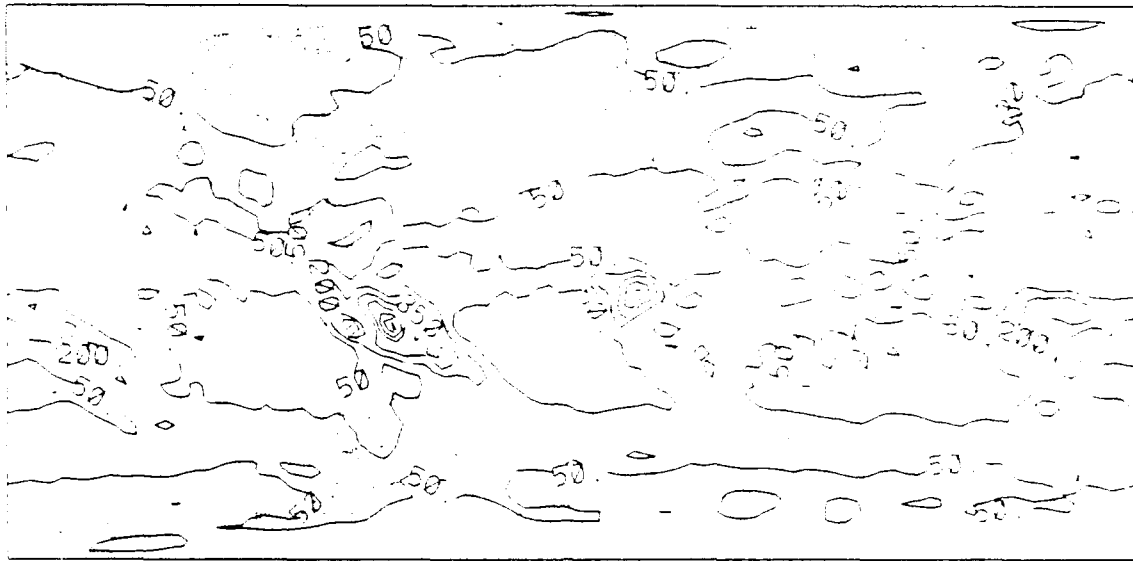


Figure 48. Maps of Outgoing Longwave Radiation ($W m^{-2}$) At the Top of the Atmosphere for (a) January and (b) June of 1979 Taken from Bess and Smith'7.

gl-89 prop (mm) 30d total jan 79



gl-89 prop (mm) 30d total jun 79



Figure 49. Maps of Accumulated Total Precipitation (mm) Summed Over Days 2-6 of All (a) January and (b) June Forecasts of GL-89 (Contour Interval is 150 mm).

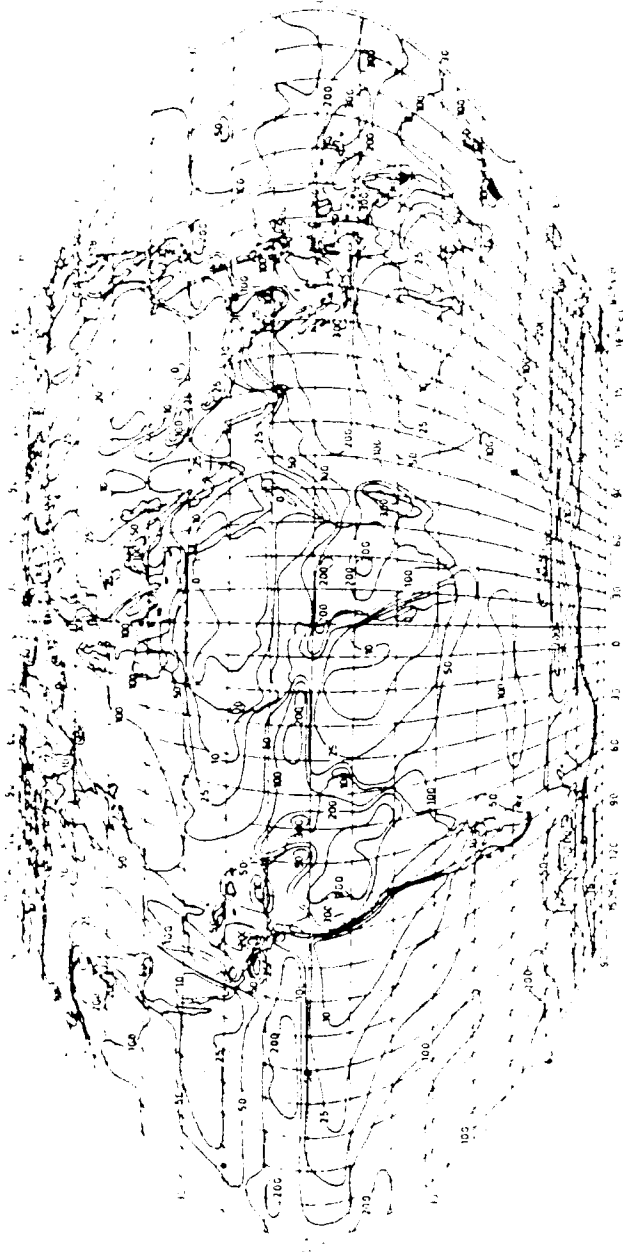


Figure 50. Map of Climatological Precipitation (mm) for January Taken from Jaeger²⁰.

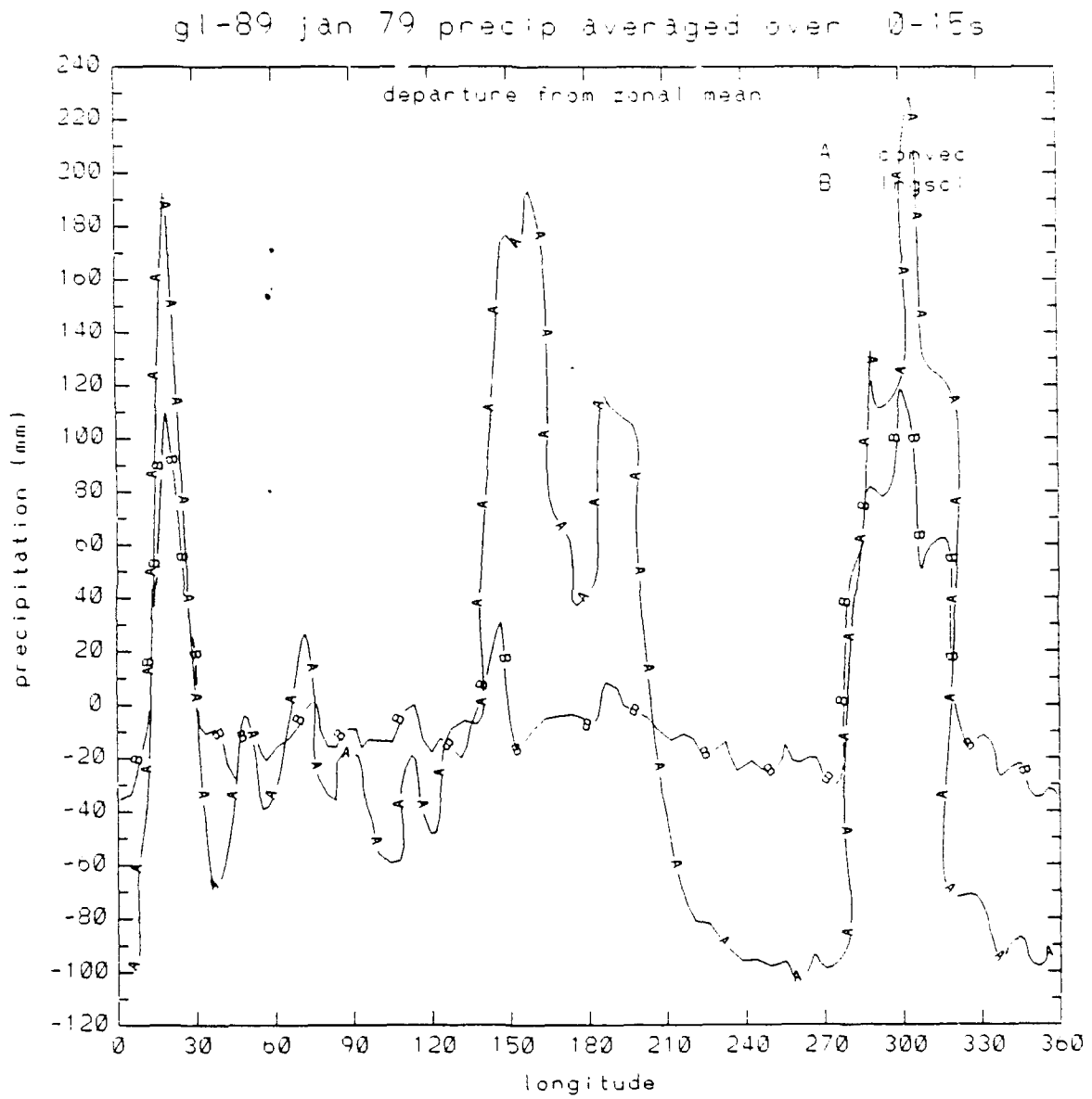


Figure 51. Latitude-Band Average Accumulated Convective and Large-Scale Precipitation (mm) Summed Over Days 2-6 of All (a) January (0°-15°S) and (b) June (0°-15°N) Forecasts of GL-89 in Their Departure from the Zonal Mean.

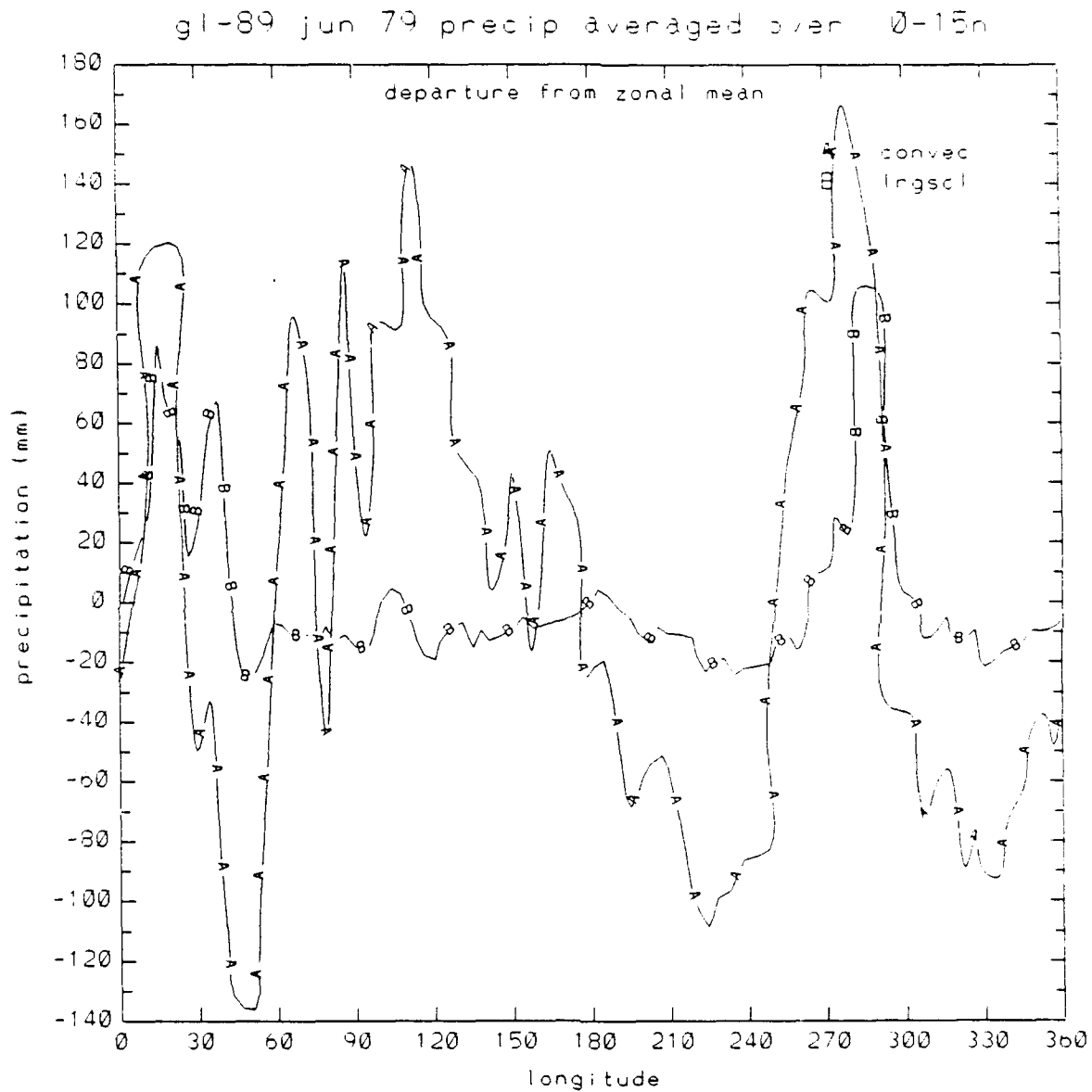


Figure 51. Latitude-Band Average Accumulated Convective and Large-Scale Precipitation (mm) Summed Over Days 2-6 of All (a) January (0°-15°S) and (b) June (0°-15°N) Forecasts of GL-89 in Their Departure from the Zonal Mean.

true for June over Africa and South America (especially at 290° longitude). There are convective maxima over water bodies; in the western Pacific (150°-210°) for January and in the Arabian Sea (70°), Bay of Bengal (90°), and South China Sea (100°-120° longitude) in June. None of them display coincident stratiform precipitation maxima.

We will now look at quantitative comparisons of model-produced precipitation and observed precipitation over two of these regions. The observed precipitation distribution was obtained by accumulating daily observed amounts averaged over all station observations during the month in the grid box and multiplying by 30. They and the GL-89 total precipitation model grid values for the tropical ocean region are shown in Figure 52. The model produces large amounts of precipitation (primarily convective) through much of the region, especially immediately north and south of the equator. The general trend in this region is to decrease in magnitude with increasing distance from the equator. Unfortunately, in all of this region except for Java to the south and the Philippines in the north, there is too little observational data to substantiate the observation-based estimates. Over these two areas, however, we can be confident of a valid comparison of observed and modeled precipitation. We do not see a discernible decreasing trend in the observed precipitation over the Philippines from south to north as is seen in the model precipitation.

Over the tropical land area in central Africa, we have depicted observed and model-produced total precipitation in Figure 53. In this case, we have also included the distribution of model-produced convective precipitation. We have done this because the model produced a substantial amount (>50 mm) of large-scale (stratiform) precipitation over much of the region. Considering that thunderstorms have been observed on more than half the days of a typical June in the western and central part of this region (see Figure 57), we expect that convection should dominate the total precipitation sources. Yet fully 30 percent of the total model-produced precipitation in this region is contributed by large-scale processes. This combination yields enormous amounts of precipitation. Both model convective and total precipitation amounts are greatest in the central part of the region, with lesser amounts (although still very large) to the east and west. The observed distribution, on the other hand,

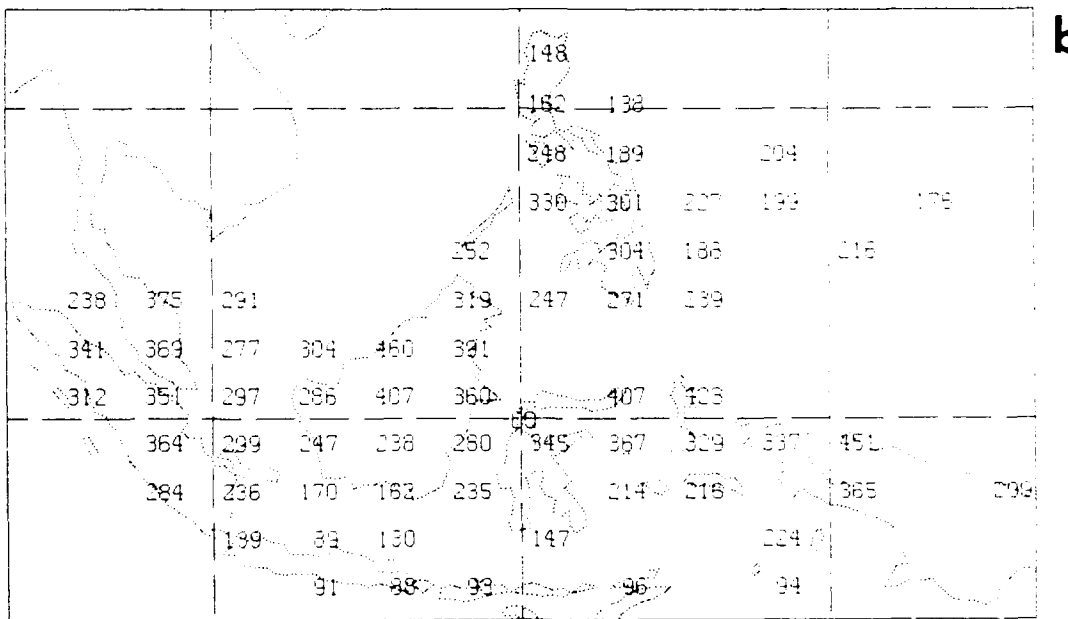
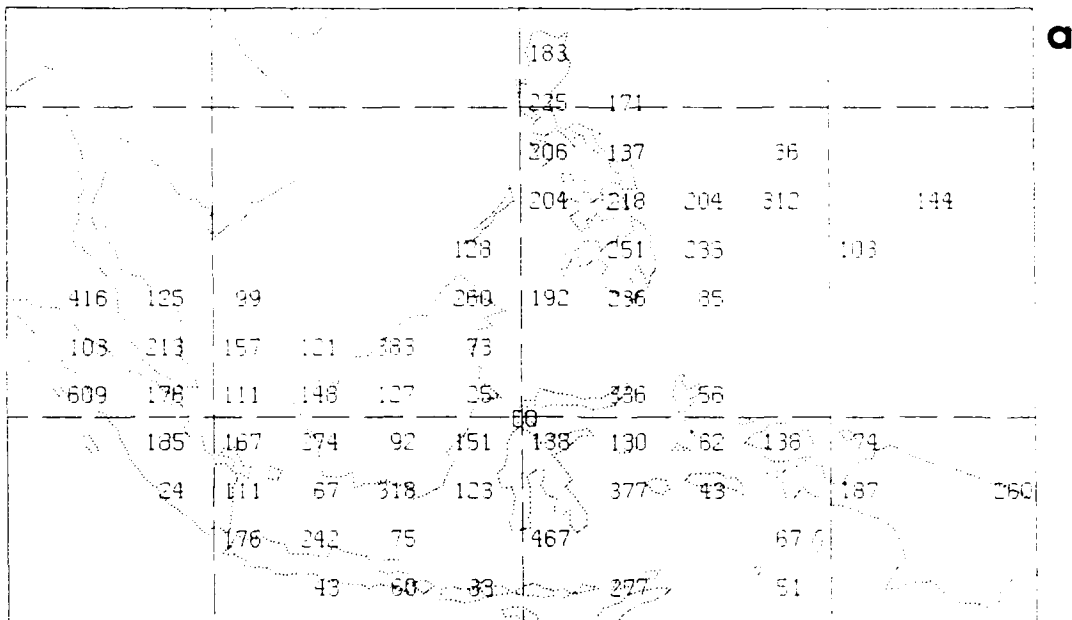


Figure 52. GSM Grid Box Accumulated Precipitation (mm) for June 1979 over the Tropical Ocean Area: (a) Observed, (b) GL-89.

a

	3	5		1										164	192	213
	3	6		3	0		1	0						110	207	200
	11	2	2	31	1	8		1						207	221	262
	35	211	213	249	111	53	35	77						191	193	334
	65	58	64	83	162	149	140	79	1	29	318	200	166	16		
	77	63	136	130	137	123	73	54	37	10	377	174	137	206		
		163	178	247	155	187	97	63	152	40	20	12	114			249
			402				472	72	95	70				0	118	231
							114	9	28	32					170	154
							71	34	45	7	0			40	51	68
								32	12	71				61	50	78
								6	27	0				23	65	35

b

	1	1		0										6	1	1
	1	2		3	2		5	3						12	5	3
	10	2	3	6	10	27		24						117	13	25
	22	31	69	64	106	176	203	148						221	180	228
	117	206	273	270	317	360	435	457	523	491	337	468	596	392		
	309	437	380	328	332	422	446	603	763	491	356	322	487	427		
		249	214	168	194	249	267	409	666	590	294	168	111	127	222	
			65				107	218	420	363			96	41	61	
							68	148	220	130				14	13	
							69	123	126	41	19			8	17	29
								28	22	10				5	14	73
								3	7	2				1	13	68

Figure 53. GSM Grid Box Accumulated Precipitation (mm) for June 1979 over the Tropical Land Area: (a) Observed, (b) GL-89 total, (c) GL-89 Convective.

	0	0		0							4	0	0		
	0	0		1		2	1				10	2	0		
	0	0	1	2	3	18	13			106	15	17	4		
	11	21	59	72	94	140	150	110		158	128	157	72		
	76	139	204	202	233	270	301	319	339	358	234	294	368	194	
	204	304	272	214	232	238	297	424	512	359	228	194	226	159	
		205	150	123	146	183	202	316	443	380	212	96	35	13	38
			51				79	166	289	230			6	3	13
							44	97	109	76		4		1	6
							23	77	51	19	12		1	2	8
								14	8	2			1	2	12
								2	1	0			0	1	7

Figure 53. GSM Grid Box Accumulated Precipitation (mm) for June 1979 over the Tropical Land Area: (a) Observed, (b) GL-89 total, (c) GL-89 Convective.

has the greatest amounts in the east, somewhat lesser amounts in the west, with the lightest amounts in the central section.

The discussion of our experimental results has concentrated on the behavior of model convection in the tropics. We now turn our attention to convection outside the tropics. Because of the greater land-ocean contrasts and abundance of observational data in the Northern Hemisphere, we will limit our discussion to the Northern Hemisphere extratropics. We will consider separately wintertime and summertime convection in the model.

Looking again at Figure 45a, the zonal-average of accumulated precipitation for January, we see a peak of 80 mm of precipitation in the climatological distribution at 40°N. This roughly coincides with a peak of model-produced precipitation of 125 mm. Actually, model precipitation exceeds climatological precipitation from 25°N to 90°N, but convection is not a significant factor northward of 50°N as can be seen in Figure 46a. This figure also reveals that the surplus model precipitation in the 25°-50°N band is primarily due to large-scale precipitation processes. Clearly, the maximum difference between model and climatology at 40°N in Figure 45a is explained by the peak of stratiform precipitation at 40°N as shown in Figure 46a. However, it is of interest to also investigate the realism of the minor maximum of convective precipitation in Figure 46a centered on 35°N.

Looking again at Figure 47a, the map of GL-89's convective precipitation for January, we see significant mid-latitude convective precipitation (>50 mm) being produced over the western Atlantic and across the western and central Pacific. On the other hand, the January climatological map (Figure 50) indicates that the eastern Atlantic and eastern Pacific both receive more than 100 mm of precipitation in January. However, it is impossible to break this down between convective and stratiform processes. It is worth noting that both regions are characterized by relatively warm ocean bodies downstream of large continents over which cold, dry

westerly flow is typical in wintertime. Several studies (e.g., Bosart²⁸) document the role of convective activity in deepening of extratropical cyclones off the east coast of the United States at about these latitudes (25°-40°N). Petterssen²⁹ assigns a relatively high frequency of occurrence of cyclogenesis for the region east of Cape Hatteras (about 35°N) and the region just south of the southern tip of Japan (28°-30°N). This suggests that convective processes could also be playing an active role in the development of cyclones off the east coast of China at these latitudes. We are not aware of any studies that describe cyclogenesis or sustained convective activity over the central Pacific in the 25°-40°N latitude band in January. The longitudinal distribution of convective and stratiform precipitation for this latitude band is presented in Figure 54. The west-central Pacific convective maximum is spread over some 90° of longitude with moderate magnitudes, while the western Atlantic maximum is larger and is confined to about 40° of longitude (285°-325°).

There appears to be quite good agreement between model and climatological zonally-averaged precipitation in the Northern Hemisphere summertime midlatitudes according to Figure 45b. Figure 46b indicates that north of about 30°N, the dominant contributor to the total zonally-averaged precipitation is from stable processes. The map of convective precipitation accumulation for June (Figure 47b) indicates that the model produced significant mid-latitude amounts over just two areas: central and eastern North America and extreme eastern Asia. These regions correspond to the maxima in the longitudinal distribution over the 35°-50°N band (Figure 55) at 120°-140° longitude (eastern Asia) and 250°-290° longitude (central and eastern North America).

To assess the realism of model-produced summertime precipitation in mid-latitudes more quantitatively, we compared GL-89 and observed accumulations for June over North America. Figure 56, which shows both fields in a region centered over the

²⁸Bosart, L.F. (1981) The President's Day snowstorm of 18-19 February 1970. A subsynoptic scale event, *Mon. Wea. Rev.*, **109**:1542-1566.

²⁹Petterssen, S. (1956) *Weather Analysis and Forecasting*, McGraw and Hill, New York, p. 267.

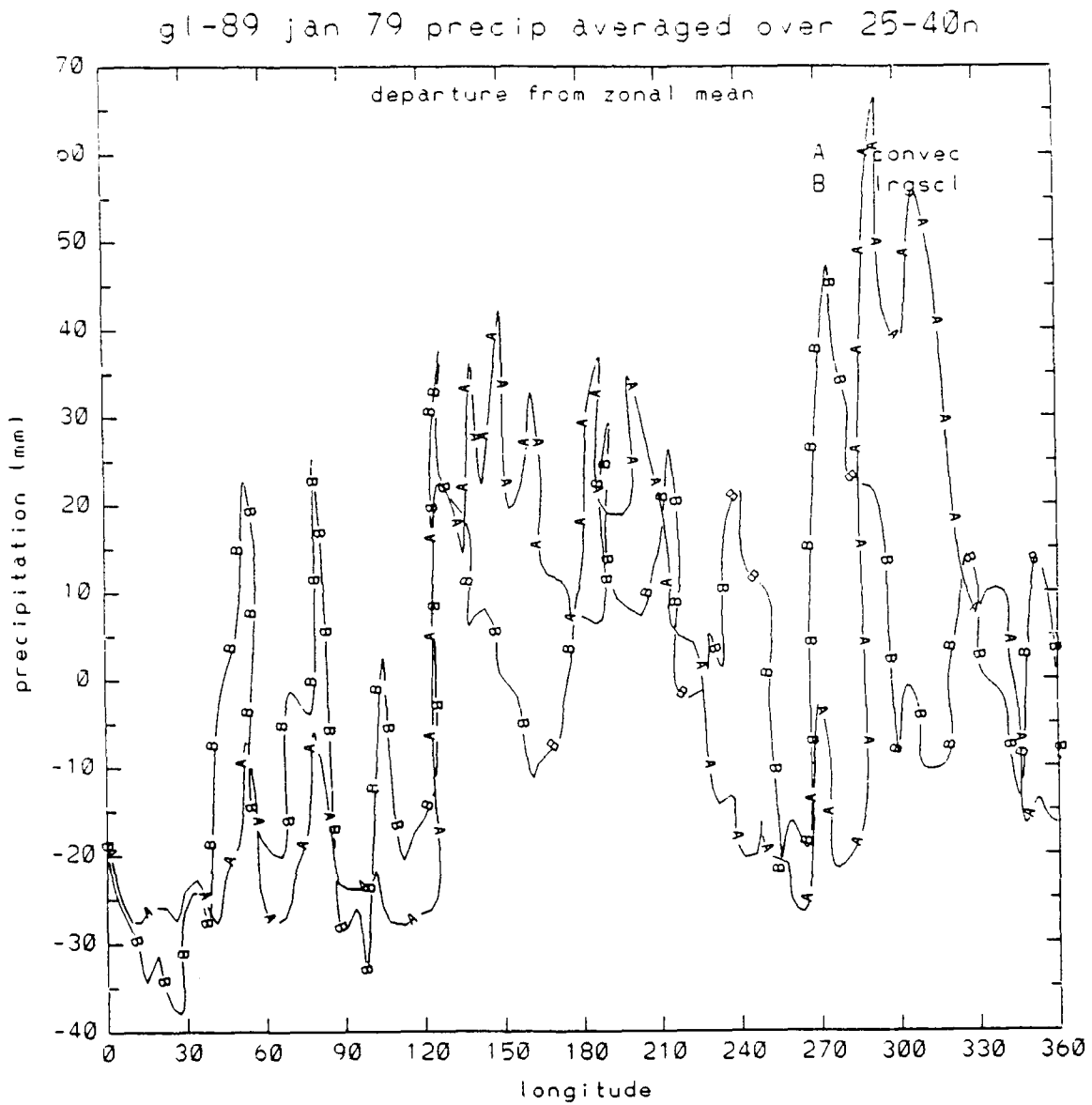


Figure 54. Latitude-Band (25° - 40°N) Average Accumulated Convective and Large-Scale Precipitation (mm) for January Forecasts of GL-89 in Their Departure from the Zonal Mean.

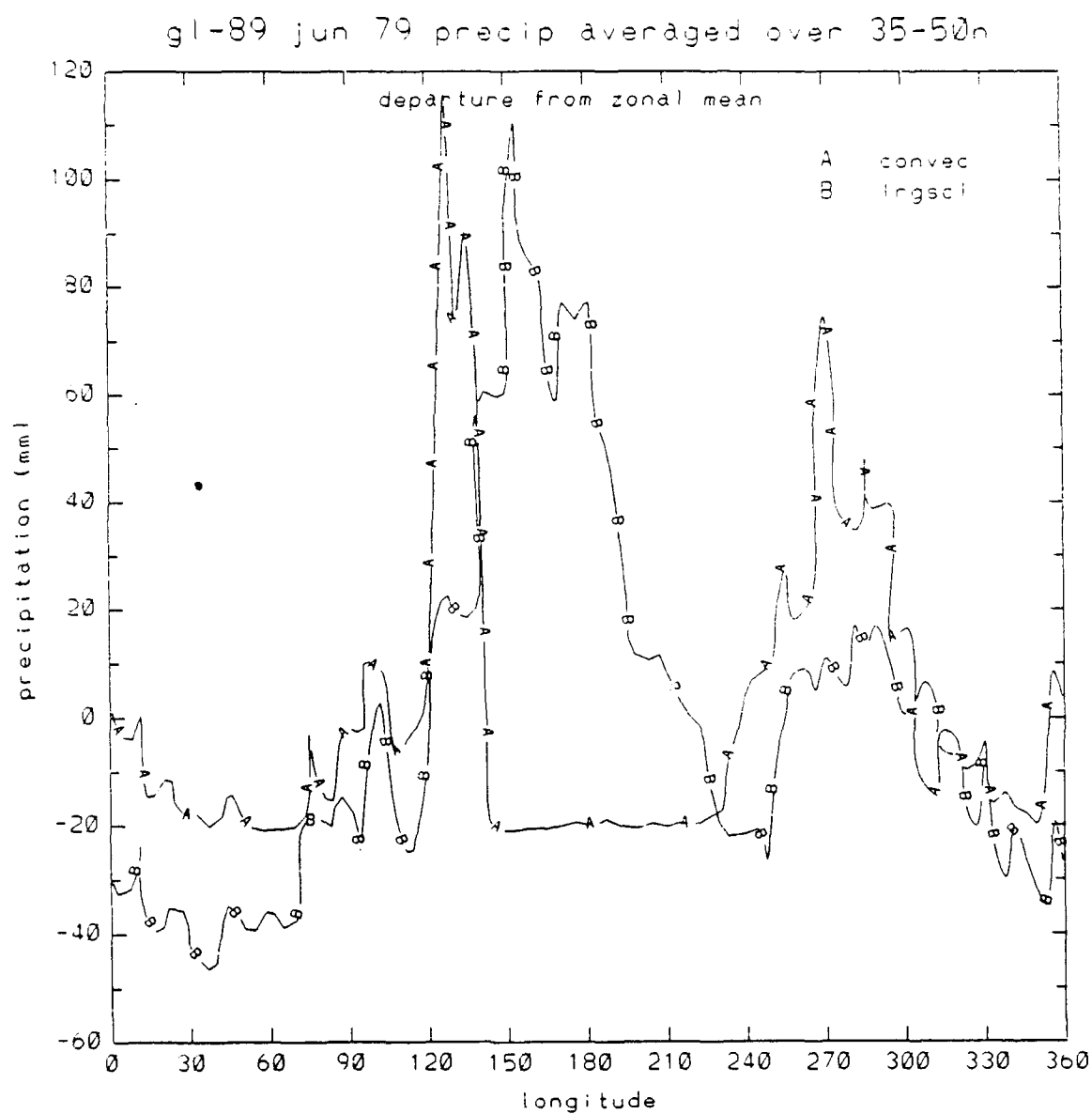


Figure 55. Latitude-Band (35° - 50°N) Average Accumulated Convective and Large-Scale Precipitation (mm) for June Forecasts of GL-89 in their Departure from the Zonal Mean.

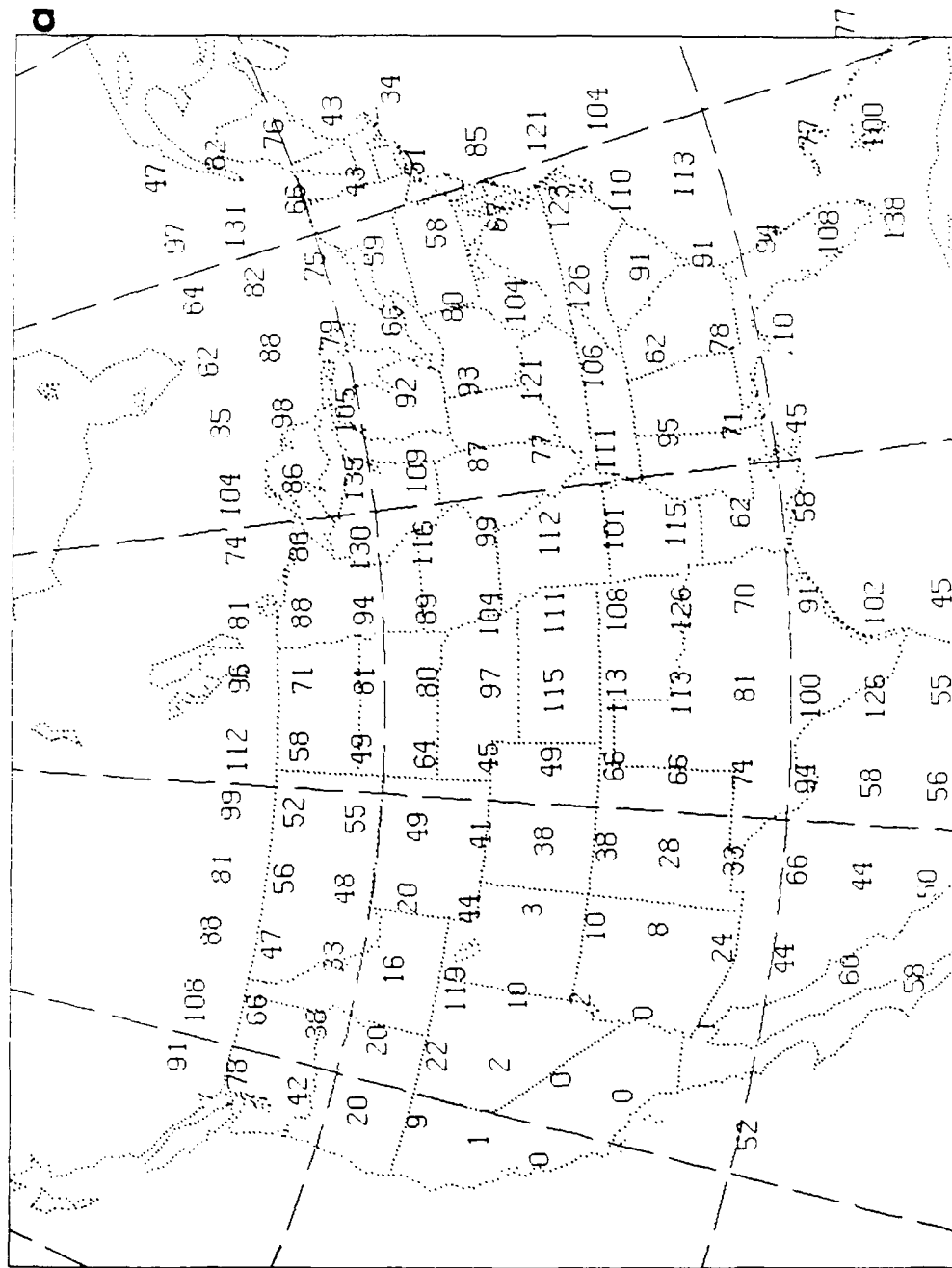


Figure 56. GSM Grid Box Accumulated Precipitation (mm) for June 1979 over the U.S.: (a) Observed, (b) GL-89.

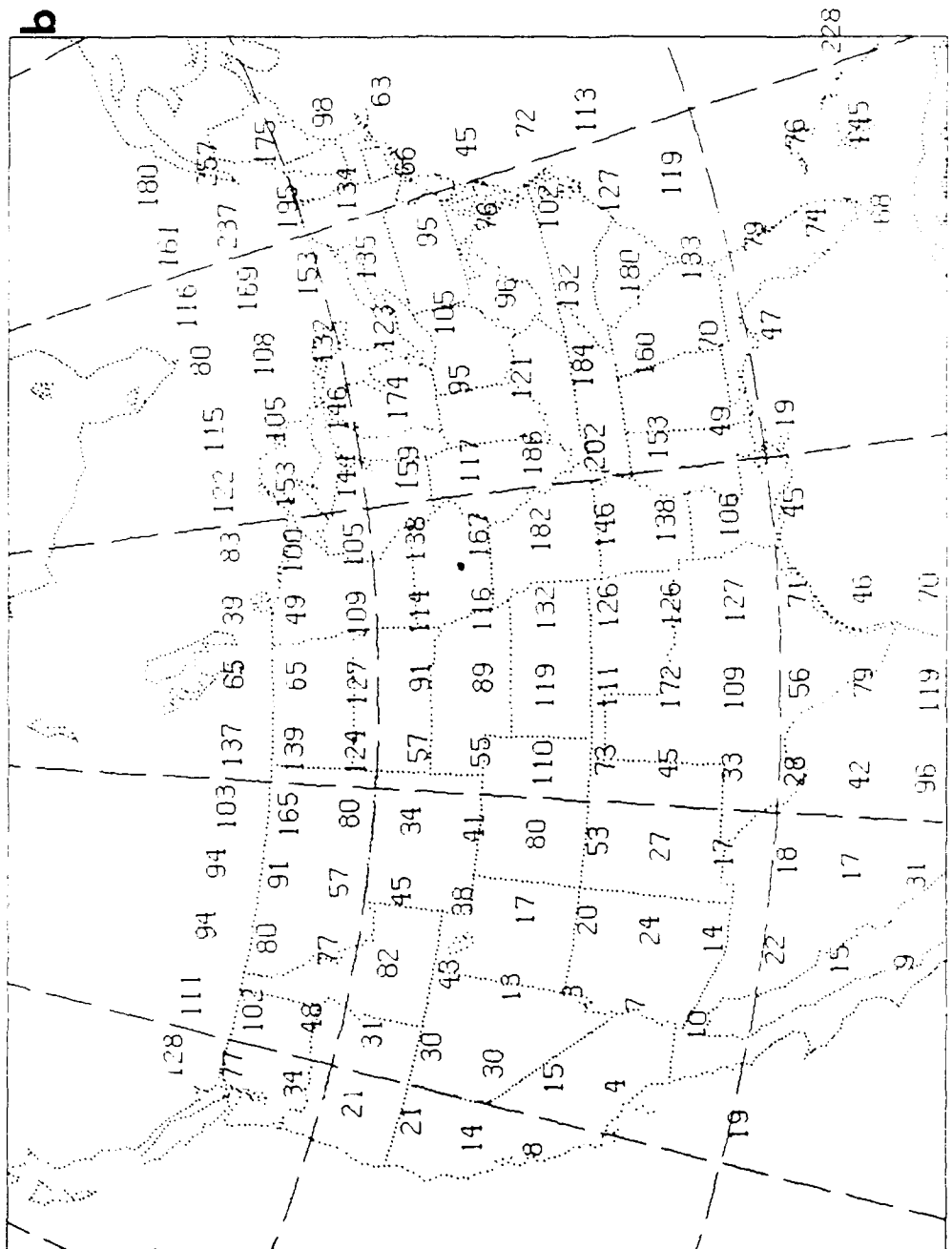


Figure 56. GSM Grid Box Accumulated Precipitation (mm) for June 1979 over the U.S.: (a) Observed, (b) GL-89.

United States, reflects lower precipitation amounts in the west and southwest. We recall from Figure 47b that model-produced convective precipitation exceeded 50 mm just over the central and eastern U.S. Since the total precipitation from GL-89 exceeds 50 mm over all but the southwestern U.S., this indicates that stable precipitation is generated in areas common to the generation of convective precipitation. This fact makes it difficult to separate out and assess the realism of just the convective portion of the model precipitation processes.

Figure 57 is a global map of the average number of thunderstorm days in June (from Guttman³⁰) prepared from tables of the average number of days with thunderstorms occurring in a given month compiled in World Meteorological Organization Publication No. 21.³¹ While data from any of the less populated regions of the world may be less reliable, the data within the U.S. should represent a good estimate of actual thunderstorm occurrence distribution domestically. Note there is reasonably good agreement between the region of the U.S. with five or more thunderstorm days in Figure 57 and the region of 50 mm or more convective precipitation in Figure 47b. An exception to this is the Gulf Coast states and Gulf of Mexico being omitted from >50 mm domain in Figure 47b. Also, the 50 mm contour lies too far east in the central U.S. Areas with 10 or more thunderstorm days (for June) shown in Figure 57 include the Central Plains (South Dakota, Nebraska, Kansas, Oklahoma, and eastern Wyoming and Colorado) and the Southeastern United States, including the Gulf of Mexico.

Figure 58 shows the difference between accumulated GL-89 total precipitation and observations. Over the area as a whole, GL-89 produced more accumulated precipitation than was observed. In the figure, we have identified regions of the U.S. and Canada that characterize different regimes of performance by the convective and

³⁰Guttman, N.B. (1971) *Study of Worldwide Occurrence of Fog, Thunderstorms, Supercooled Low Clouds and Freezing Temperatures*. U.S. Naval Weather Service Command, NAVAIR 50-1C-60, p. 42.

³¹World Meteorological Organization (1956) *World Distribution of Thunderstorm Days*, WMO Publication No. 21, Secretariat of the World Meteorological Organization, Geneva, Switzerland.

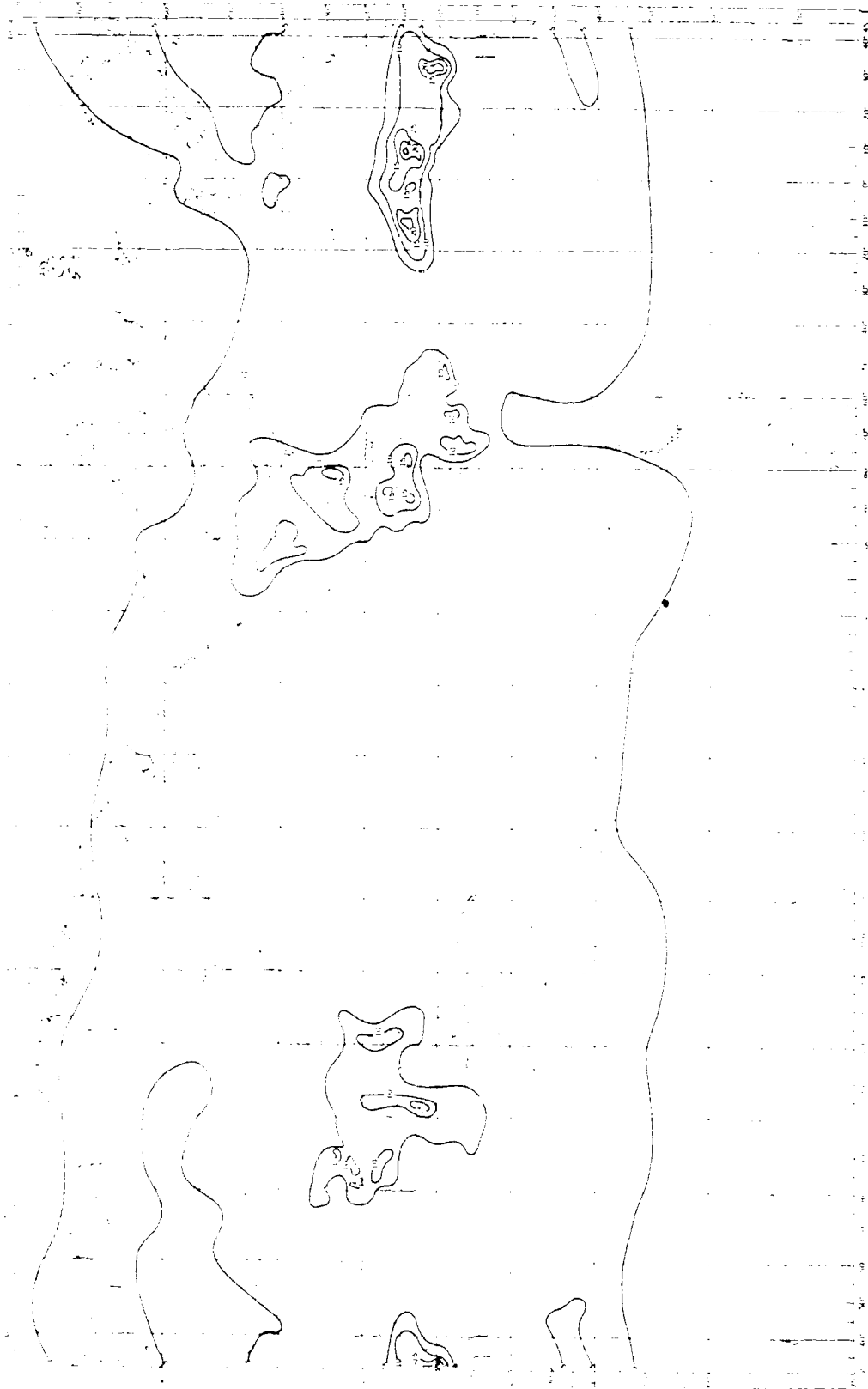


Figure 57. Map of Average Number of Thunderstorm Days for June Taken from Guttman.³⁰

large-scale precipitation algorithms of GL-89. Table 1 gives the statistics for each region that are relevant to the following discussion.

According to Figure 57, the Central Plains, Southeast, and Gulf Coast regions are areas where convective processes probably play a dominant role in the accumulation of total precipitation over the month. Convective precipitation should contribute significantly to the total also over much of the Northeast region. From Table 1 we see that in the Central Plains, GL-89 convective precipitation contributed less than half of the total rainfall.

Table 1. GL-89 and Observed Accumulated June 1979 Precipitation

Region	No. Grid Pts	Ave Conv	Ave Tot	Conv/Tot	Ave Obs	Tot/Obs
Central Plains	15	43 mm	102 mm	0.42	90 mm	1.14
Southeast	12	109	157	0.69	102	1.54
Northeast	20	69	138	0.50	75	1.84
Gulf Coast	13	52	76	0.69	81	0.93
Northwest	20	44	78	0.56	55	1.42

In the Southeast and Gulf Coast, GL-89 convective rainfall accounted for almost 70 percent of the total. In the Southeast, more convective precipitation was generated than the total amount observed, while in the Gulf Coast, only 64 percent of the total observed was contributed by GL-89 convective processes. Climatologically, we would expect that nearly all of the rainfall in the Gulf Coast should be contributed by convection due to the warm, moist, tropical nature of this area in the summertime. In the Northeast, nearly enough convective precipitation was generated by the model to account for the total observed precipitation. Yet we know that stratiform precipitation plays a significant role in the summertime precipitation here. Finally, it is apparent that convective rainfall from GL-89 accounts for over half the

model-produced precipitation in the Northwest. In an area where convection probably plays a less important role than does stratiform precipitation, the model convective precipitation is about 80 percent that of the observed accumulated precipitation.

5.2 Conclusions

The average January and June forecasts were based on six 10-day forecasts in each month. The temporal distribution of the globally-averaged precipitation rate revealed total precipitation that was 2-3 times the climatological value in GL-87. Some 80 per cent of the total precipitation in GL-87 was contributed by convective processes. GWC84 produced about one fifth as much precipitation as is commonly observed, of which scarcely 10 percent is convective. GL-89 globally-averaged total precipitation rates were in excellent agreement with climatological rates. About half of the total was convectively generated. Thus, we see a strong relationship between percentage of total rainfall contributed by convection and agreement with climatology.

We found that the diurnal signal in the globally-averaged precipitation rates was caused primarily by a diurnal pattern of intense convection over a single longitude sector. Two other longitude sectors produced diurnal convection of somewhat lesser intensity, and their presence spread out and slightly obscured the diurnal signal caused by the region of greatest intensity. Yet the clarity of the diurnal signal in the global-average rates is symptomatic of the spuriously high convective activity produced by the model in these confirmed areas of heavy convection.

GL-87 globally-averaged surface evaporation rates were found to be substantially less than total precipitation rates through the 10-day period. The evaporation rates in GL-89 slightly exceeded (by about 0.5 mm/day) precipitation rates. Yet in both cases, global specific humidity (atmospheric water vapor content) was reduced somewhat from initial levels. The rate of decrease in the first 5 days was greatest (somewhat greater for GL-87), and remained relatively stable beyond 5 days, continuing to decrease slowly in GL-87. Clearly, the gross imbalance between precipitation and evaporation is causing the decline in GL-87. Even though the

imbalance continues during the entire 10-day forecast period, the rate of decrease of the global specific humidity lessens in the last half of the period. It is not clear why greater evaporation than precipitation would lead to a decrease in global specific humidity in the first 5 forecast days in GL-89. Perhaps the model is generating its own water vapor climatology that is lower globally than the FGGE III-B initial conditions. This model climatology remains relatively stable during the last 5 days of the forecast, probably as a result of the near balance between evaporation and precipitation. It is not known how much of a role dew evaporation (included in the global evaporation averages) and dew deposition (not included in the global precipitation averages) would play in the hydrological balance of the model. We suspect that it would not fully account for the 0.5 mm/day imbalance in GL-89. These uncertainties suggest the need for a global water budget study to ascertain the magnitudes of the various source and sink terms and account for the apparent loss of global moisture during the first 5 days.

GL-89 zonally-averaged total precipitation for the months of January and June agreed quite well with climatological values between 60°S and 60°N latitudes where climatology is considered most reliable. Both distributions exhibited trimodal distributions with largest values in the tropics and lesser peaks in the mid-latitudes. The climatological Southern Hemisphere mid-latitude precipitation is greater than that of the Northern Hemisphere in both months. GL-89 reproduced this trend with the exception of the Northern Hemisphere winter mid-latitudes, which exhibited precipitation amounts as large as those in the Southern Hemisphere in both seasons. The major portion of this overabundant GL-89 Northern Hemisphere mid-latitude winter precipitation was generated by stable processes. In fact, convective processes were dominant only in the tropics, where zonal averages of total precipitation were in generally good agreement with climatology.

Maps of monthly-averaged outgoing long-wave radiation (OLR), where minima indicate regions of persistent deep convection, were used to verify the longitudinal positions of the convective precipitation maxima as generated by GL-89. The three convective maxima in each month were positioned longitudinally in essentially the

same places as the OLR minima. In the tropics, the model seems to be producing the right amount of zonally-averaged total precipitation, and the maxima are in the correct longitudinal positions. We compared the January GL-89 total precipitation map with a climatological precipitation map for the same month. Both showed regions of tropical minimum precipitation (50 mm or less) lying just west (downwind) of each of the maxima (200 mm or more) in the tropics. We conclude from this that the model is doing well in reproducing the longitudinal positioning of maxima and minima of convective precipitation in the tropics.

The model was found to have a tendency to produce copious amounts of stratiform precipitation in areas of tropical maximum convective precipitation where these maxima occur over land masses. No evidence of this phenomenon was present over ocean bodies where convective maxima occur. We speculate that the spurious stratiform precipitation results from lower model layers left saturated over land areas due to enhanced surface evaporation, which in turn is triggered by the heavy convective precipitation. More study of model results, including the longitudinal distribution of surface evaporation, will have to be performed to confirm this hypothesis.

GL-89 produces too much total precipitation over areas of confirmed tropical convective maxima. Quantitative assessment of precipitation over both a land area (Africa) and an ocean-island area (Indonesia and Philippines) in June convinces us that the maxima, while positioned correctly, are excessive. This is particularly true over the land areas, where heavy convective activity seems to trigger heavy stratiform precipitation. In such a case in tropical Africa, 2-3 times too much precipitation was produced by the model. In addition, the positions of the relative maxima within each region were not correctly placed in latitude (Asian region) or longitude (African region).

Because of the lack of observations, it is difficult to verify the quantitative values of the regions of tropical minimum convective activity lying west of the maxima. However, because the maxima were overforecasted and the zonal average was in good agreement with climatology we conclude that the minima were underforecasted in

precipitation amounts. The tendency of the Kuo-type convective schemes to dump precipitation in preferred regions to the exclusion of others has been noted by many authors [e.g., Emmanuel³²]. It has been attributed to the build-up of convective instability (CAPE) at the grid point until moisture convergence was of sufficient magnitude to switch on the moist convection algorithm. Then, this energy is allowed to be released suddenly, resulting in "grid point storms." However, in diagnosing the behavior of the scheme at individual tropical grid points, we have noticed that a positive feedback mechanism leads to the build-up of heavy convective activity. We saw in Section 5 that over a convectively-active tropical region, convective precipitation rates were growing in the face of decreasing CAPE but increasing moisture convergence in the region. At least in our version of the Kuo scheme, it is the positive feedback between moisture convergence (moisture advection and surface evaporation) and the release of latent heat that is the primary factor in overactive cumulus convection. We have not diagnosed the relative contributions of moisture convergence due to large-scale flow convergence and that due to surface evaporation. We have seen that the evaporation is in phase with convection in the global average rates. In any case, an increase of moisture convergence triggered the increase of the cumulus heating, and a decrease of moisture convergence stopped the convective activity. Emmanuel^{32,33} has suggested that this dependence of latent heat release on moisture convergence is not realistic. If this is true, then the scheme might not be able to simulate the diurnal activity of cumulus over purely ocean areas where no differential heating or pronounced diurnal evaporation pattern exists to set up areas of localized moisture convergence. We intend to investigate the diurnal nature of the convective scheme in a future study.

We investigated the relative contributions of GL-89 convective and stratiform precipitation in the winter Northern Hemisphere mid-latitudes. We found that the

³²Emmanuel, K.A., (1988) Reply, *J. Atmos. Sci.*, **45**:528-3530.

³³Emmanuel, K.A. (1987) Large-scale and mesoscale circulations in convectively adjusted atmospheres, *Proceedings of a Workshop on Diabatic Forcing*, 30 Nov. - 2 Dec. 1987, ECMWF, Shinfield Park, Reading RG2 9AX, United Kingdom, p. 323-348.

excessive model precipitation was primarily due to stable processes. However, the model did produce a minor maximum of convective precipitation centered on 35°N. This convective precipitation was located in the western Atlantic and western and central Pacific oceans. We suggest that in the case of the western Atlantic and western Pacific, cold, dry offshore flow off continents and over the warmer oceans downstream may be resulting in instabilities that could be inducing moderate wintertime convection. Other studies have concluded that these areas are significant areas of wintertime cyclogenesis in which moist convection plays an important role. Thus, these model-produced regions of wintertime convection east of North America and Asia appear to be realistic in their location. It is difficult to discern the realism of their magnitude.

GL-89 simulated the zonally-averaged total precipitation in the Northern Hemisphere summer at middle latitudes quite well. We found that this total was dominated by stable precipitation. The model produced significant convective precipitation over only central and eastern North America and eastern Asia. We attempted to assess the realism of the model-produced convective precipitation (and thus the mid-latitude summer convective activity) by comparing simulated and observed precipitation over the U.S. in June.

We found that the model did not produce enough convective precipitation over the Central Plains and Gulf Coast. On the other hand, in the Southeast most of the rainfall was convective, and this portion alone was slightly more than the total observed June rainfall. In these three areas where convection is the dominant contributor to total precipitation, we do not understand why the model produced sufficient convective precipitation only over the Southeast. Grell and others³⁴ suggest that the dependence of the Kuo scheme on cloud-environment temperature and moisture differences may limit the scheme's effectiveness in the mid-latitudes where these profiles depend heavily on synoptic conditions. However, we must

³⁴Grell, G., Kuo, Y.-H., and Pasch, R. (1988) Semi-prognostic tests of three cumulus parameterization schemes for mid-latitude convective systems, *Preprints, Eighth Conf. on Numerical Weather Prediction*, 22-26 Feb. 1988, Baltimore, American Meteorological Society.

continue to investigate the behavior of the scheme on a case-by-case basis to ascertain the cause of the systematic underactivity of convection in the Central Plains and Gulf Coast. In the northeast, the convective precipitation alone was almost as large as the observed total rainfall. This suggests that too much of both convective and stratiform precipitation was produced by the model. In the Northwest, this same overprediction was observed. Convective precipitation was judged to be excessive in its proportion of the total predicted rainfall. In summary, the model was overactive in convective activity in the Northeast and Northwest, and underactive in the Central Plains and Gulf Coast. In the Southeast and Southwest, the convective scheme probably produced slightly too much convective precipitation but was in much better agreement with what would be observed if only convective precipitation were measured.

6. SUMMARY AND RECOMMENDATIONS

The improvements we have made in the University of Illinois MODKOU convective parameterization have yielded globally- and zonally-averaged precipitation consistent with climatological values. These improvements have included corrections (including removal of the ill-designed entrainment formulation), algorithmic upgrades, and inclusion of more physical realism in the scheme. However, we have not changed the basic Kuo¹³ parameterization or the Krishnamurti et al¹⁵ closure scheme.

The scheme (after our modifications) correctly positions the areas of tropical convective precipitation maxima and minima around the globe. It tends to make the maxima excessive and underpredict the minima. The scheme's activity level in the tropics is quite sensitive to moisture convergence and insensitive to conditional instability. Over land areas the maxima are further enhanced by excessive stratiform precipitation apparently triggered (in part) by the scheme. In mid-latitude summer time convection, the scheme overpredicts precipitation in areas where actual convection is light-to-moderate, and underpredicts in areas where convection is

observed to be a frequent process. Thus, the behavior of the parameterization is fundamentally different between the tropics and mid-latitudes.

We conclude that further work needs to be done on the parameterization package to reduce the escalation of the convective process that creates deluges in areas of heavy tropical precipitation. The appropriateness of its sensitivity to moisture convergence should be studied further. By doing this, we could expect to obtain a more realistic longitudinal distribution of the magnitude of convective heating. This includes an investigation of why heavy stratiform precipitation is set off over land areas by the convection scheme. The model should be investigated to see if a trend toward increase in precipitation with forecast time is typical over heavy convection areas. We also suggest that the scheme be investigated in case studies over mid-latitudes to determine why too much precipitation is produced in some areas, and not enough in others. As an example, would the scheme benefit from an entrainment formulation that is designed differently?

Another issue of major importance is the role of the moist convection scheme in the global water budget. In particular, the GSM should be examined to determine why its atmosphere dries out in the first 5 days of the forecast. We should determine why the use of the improved convective scheme in GL-89 results in a tropical cold bias in the lower and middle troposphere, a negative RH bias in the lower troposphere, and a positive RH bias in the upper troposphere. More attempts should be made to verify the vertical structure of the model's convective heating and drying profiles. The realism of wintertime mid-latitude convection magnitudes should be determined. We have yet to attempt to verify the diurnal cycle of the simulated convection within the GL-89 GSM. This last issue will be taken up in a follow-on study and reported on later.

We chose to implement the modified Kuo parameterization in the GSM because of its computational efficiency. Its results were comparable with those of the Arakawa-Schubert parameterization over a limited area in a limited sample.¹⁰ However, when MODKuo was first implemented globally, it produced quite unreasonable precipitation rates in the global average. We recommend that if the

modified Arakawa-Schubert scheme is implemented in a GSM it be subjected to the same diagnosis described in this report. Such a study would provide insight on whether the additional computational expense is compensated by improved GSM performance.

References

1. Sela, J. (1980) Spectral Modeling at the National Meteorological Center, *Mon. Wea. Rev.*, **108**:1279-1292
2. Brenner, S., Yang, C.-H., and Yee, S.Y.K. (1982) *The AFGL Spectral Model of the Moist Global Atmosphere: Documentation of the Baseline Version*, AFGL-TR-82-0393, Air Force Geophysics Laboratory, Hanscom AFB, MA. [NTIS ADA 129283]
3. Brenner, S., Yang, C.-H., and Mitchell, K. (1984) *The AFGL Global Spectral Model: Expanded Resolution Baseline Version*, AFGL-TR-84-0308, Air Force Geophysics Laboratory, Hanscom AFB, MA. [NTIS ADA 160370]
4. Ballish, B.A. (1980) *Initialization Theory and Application to the NMC Spectral Model*, Ph.D. Thesis, Dept. of Meteorology, Univ. of Maryland.
5. Mahrt, L., Pan, H.-L., Paumier, J., and Troen, I. (1984) *A Boundary Layer Parameterization for a General Circulation Model*, AFGL-TR-84-0063, Air Force Geophysics Laboratory, Hanscom AFB, MA. [NTIS ADA 144224]
6. Mahrt, L., Pan, H.-L., Ruscher, P., and Chu, C.-T. (1987) *Boundary Layer Parameterization for a Global Spectral Model*, AFGL-TR-87-0246, Air Force Geophysics Laboratory, Hanscom AFB, MA. [NTIS ADA 199440]
7. Liou, K.-N., Ou, S.-C., Kinne, S., and Koenig, G. (1984) *Radiation Parameterization Programs for Use in General Circulation Models*, AFGL-TR-84-0217, Air Force Geophysics Laboratory, Hanscom AFB, MA. [NTIS ADA 148015]
8. Ou, S.-C., and Liou, K.-N. (1988) *Development of Radiation and Cloud Parameterization Programs for AFGL Global Models*, AFGL-TR-88-0018, Air Force Geophysics Laboratory, Hanscom AFB, MA [NTIS ADA 202020]

9. Soong, S.-T., Ogura, Y., and Kau, W.-S. (1985) *A Study of Cumulus Parameterization in a Global Circulation Model*, AFGL-TR-85-0160, Air Force Geophysics Laboratory, Hanscom AFB, MA [NTIS ADA 170137]
10. Kao, C.-Y.J., and Ogura, Y. (1985) *A Cumulus Parameterization Study with Special Attention to the Arakawa-Schubert Scheme*, AFGL-TR-85-0159, Air Force Geophysics Laboratory, Hanscom AFB, MA. [NTIS ADA 166801]
11. Arakawa, A. and Schubert, W.H. (1974) Interaction of a Cumulus Cloud Ensemble with the Large-Scale Environment, Part 1, *J. Atmos. Sci.*, **31**:674-701.
12. Kuo, H.-L. (1965) On formation and Intensification of Tropical Cyclones Through Latent Heat Release by Cumulus Convection, *J. Atmos. Sci.*, **22**:40-63.
13. Kuo, H.-L. (1974) Further Studies of Parameterization of the Influence of Cumulus Convection on Large-Scale Flow, *J. Atmos. Sci.*, **31**:1232-1240.
14. Yang, C.-H., Mitchell, K., Norquist, D., and Yee, S.Y.K. (1989) *Diagnostics for and Evaluation of New Physical Parameterization Schemes for Global NWP Models*, GL-TR-89-0158, Geophysics Laboratory (AFSC), Hanscom AFB, MA. ADA228033
15. Krishnamurti, T.N., Kanamitsu, M., Godbole, R., Chang C.-B., Carr F., and Chow, J.H. (1976) Study of a Monsoon Depression (II), Dynamical Structure, *J. Meteor. Sci. Japan*, **54**:208-225.
16. Yang, C.-H., and Norquist, D. (1990) An Assessment of a Moist Convection Parameterization Through a Comparison of Scheme-Generated Clouds with Observational Statistics, submitted to *Weather and Forecasting*.
17. Slingo, J.M., Mohanty, U.C., Tiedtke, M., and Pearce, R.P. (1988) Prediction of the 1979 Summer Monsoon Onset with Modified Parameterization Schemes, *Mon. Wea. Rev.*, **116**:328-346.
18. *Research Manual 3, ECMWF Forecast Model, Physical Parameterization (1984)* ECMWF Research Department, Ref: M1.6/2.
19. Sundquist, H., 1988: Personal Communication.
20. Jaeger, L. (1983) Monthly and areal patterns of mean global precipitation, in *Variations in the Global Water Budget*, A. Street-Perrott, M. Beran, R. Ratcliffe, Eds., D. Reidel, Dordrecht.
21. Molteni, F., and Tibaldi, S. (1985) *Climatology and Systematic Error of Rainfall Forecasts at ECMWF*, Tech. Rep. No. 51, European Centre for Medium Range Weather Forecasts, Shinfield Park, Reading, Berkshire RG2 9AX, England.
22. Reed, R.J., and Recker, E.E. (1971) Structure and Properties of Synoptic-Scale Wave Disturbances in the Equatorial Western Pacific, *J. Atmos. Sci.*, **28**:1117-1133.
23. Miller, B.L., and Vincent, D.G. (1987) Convective Heating and Precipitation Estimates for the Tropical South Pacific During FGGE, 10-18 January 1979, *Q.J.R. Meteorol. Soc.*, **113**:189-212.
24. Moncrieff, M.W., and Miller, M.J. (1976) The Dynamics and Simulation of Tropical Cumulonimbus and Squall Lines, *Q.J.R. Meteorol. Soc.*, **102**:373-394.

25. Betts, A.K. (1982) Saturation Point Analysis of Moist Convective Overturning, *J. Atmos. Sci.*, **39**:1484-1505.
26. Albright, M.D., Recker, E.E., Reed, R.J., and Dang, R. (1985) The Diurnal Variation of Deep Convection and Inferred Precipitation in the Central Tropical Pacific During January-February 1979, *Mon. Wea. Rev.*, **113**:1663-1680.
27. Bess, T.D., and Smith, G.L. (1987) *Atlas of Wide-Field-of-View Outgoing Longwave Radiation Derived From Nimbus 7 Earth Radiation Budget Data Set - November 1978 to October 1985*, NASA Reference Publication 1186, NASA Langley Research Center, Hampton, Virginia, pp. 11, 21.
28. Bosart, L.F. (1981) The President's Day Snowstorm of 18-19 February 1979: A Subsynoptic-Scale Event, *Mon. Wea. Rev.*, **109**:1542-1566.
29. Petterssen, S. (1956) *Weather Analysis and Forecasting*, McGraw-Hill Book Company, Inc., New York, p. 267.
30. Guttman, N.B. (1971) *Study of Worldwide Occurrence of Fog, Thunderstorms, Supercooled Low Clouds and Freezing Temperatures*, U.S. Naval Weather Service Command, NAVAIR 50-1C-60, p. 42.
31. World Meteorological Organization (1956) *World Distribution of Thunderstorm Days*, WMO Publication No. 21, Secretariat of the World Meteorological Organization, Geneva, Switzerland.
32. Emmanuel, K.A., (1988) Reply, *J. Atmos. Sci.*, **45**:3528-3530.
33. Emmanuel, K.A. (1987) Large-Scale and Mesoscale Circulations in Convectively Adjusted Atmospheres, *Proceedings of a Workshop on Diabatic Forcing*, 30 Nov. - 2 Dec. 1987, ECMWF, Shinfield Park, Reading RG2 9AX, United Kingdom, p. 323-348.
34. Grell, G., Kuo, Y.-H., and Pasch, R. (1988) Semi-Prognostic Tests of Three Cumulus Parameterization Schemes for Mid-Latitude Convective Systems, *Preprints, Eighth Conf. on Numerical Weather Prediction*, 22-26 Feb. 1988, Baltimore, American Meteorological Society.